



저작자표시-비영리-변경금지 2.0 대한민국

이용자는 아래의 조건을 따르는 경우에 한하여 자유롭게

- 이 저작물을 복제, 배포, 전송, 전시, 공연 및 방송할 수 있습니다.

다음과 같은 조건을 따라야 합니다:



저작자표시. 귀하는 원저작자를 표시하여야 합니다.



비영리. 귀하는 이 저작물을 영리 목적으로 이용할 수 없습니다.



변경금지. 귀하는 이 저작물을 개작, 변형 또는 가공할 수 없습니다.

- 귀하는, 이 저작물의 재이용이나 배포의 경우, 이 저작물에 적용된 이용허락조건을 명확하게 나타내어야 합니다.
- 저작권자로부터 별도의 허가를 받으면 이러한 조건들은 적용되지 않습니다.

저작권법에 따른 이용자의 권리는 위의 내용에 의하여 영향을 받지 않습니다.

이것은 [이용허락규약\(Legal Code\)](#)을 이해하기 쉽게 요약한 것입니다.

[Disclaimer](#)

공학박사 학위논문

고분자 전해질막 연료전지에서 막을 투과하는  
기체 크로스오버 현상에 관한 연구

A study on the gas crossover through the membrane  
in polymer electrolyte membrane fuel cells

2013년 2월

서울대학교 대학원

기계항공공학부

백 경 돈

**고분자 전해질막 연료전지에서 막을 투과  
하는 기체 크로스오버 현상에 관한 연구**

**A study on the gas crossover through the membrane  
in polymer electrolyte membrane fuel cells**

**지도교수 김 민 수**

**이 논문을 공학박사 학위논문으로 제출함**

**2013년 2월**

**서울대학교 대학원  
기계항공공학부  
백 경 돈**

**백경돈의 공학박사 학위논문을 인준함  
2012년 12월**

**위 원 장 \_\_\_\_\_ (인)**

**부위원장 \_\_\_\_\_ (인)**

**위 원 \_\_\_\_\_ (인)**

**위 원 \_\_\_\_\_ (인)**

**위 원 \_\_\_\_\_ (인)**

**A study on the gas crossover through the  
membrane in polymer electrolyte membrane  
fuel cells**

A DISSERTATION SUBMITTED TO THE SCHOOL OF  
MECHANICAL AND AEROSPACE ENGINEERING OF  
SEOUL NATIONAL UNIVERSITY IN PARTIAL  
FULFILLMENT OF THE REQUIREMENTS FOR THE  
DEGREE OF DOCTOR OF PHILOSOPHY

By

Kyung Don Baik

February 2013

## **Abstract**

# **A study on the gas crossover through the membrane in polymer electrolyte membrane fuel cells**

Kyung Don Baik

School of Mechanical and Aerospace Engineering

The Graduate School

Seoul National University

Membranes are usually used as an electrolyte in polymer electrolyte membrane fuel cells (PEMFCs). The main functions of membranes are to transfer protons from the anode to the cathode in PEMFCs and form a barrier between the anode and cathode reactants. However, gases inevitably permeate through the membrane barrier, which is referred to as the ‘gas crossover’ phenomenon. In this study, the experimental measurements of gas crossover (hydrogen, oxygen and nitrogen) were conducted using a mass spectrometer.

Firstly, the effect of operating parameters such as temperature, RH, hydrogen pressure, and membrane thickness on hydrogen crossover rate in

PEMFCs was investigated. The results show that the hydrogen crossover rate increases proportional to the increase in both temperature and relative humidity (RH). The hydrogen crossover rate also increases as hydrogen pressure increases due to the increased hydrogen partial pressure at anode side. Furthermore, the results were analyzed using a multiple linear regression analysis, indicating that the hydrogen crossover rate increases with the increase in the following variables; inverse of logarithmic membrane thickness > hydrogen pressure > RH > and temperature.

Local measurements of the hydrogen crossover rate were also conducted using a single fuel cell with the specially-designed cathode bipolar plate. The local distribution of the hydrogen crossover rate from the gas inlet to the outlet of cathode was examined. The hydrogen crossover rate near the inlet was large because the hydrogen gas pressure near the inlet was higher than that near the outlet. Thus, it was believed that the partial pressure gradient of hydrogen was one of the reasons for the local variation of hydrogen crossover in the fuel cell.

The quantitative measurements of oxygen crossover that reacts with hydrogen have been conducted. The effective oxygen permeability could explain the exact amount of oxygen crossover that affect the membrane degradation and/or water generation under the fuel cell operating conditions.

Thus, the effective oxygen permeability should be considered as an index of the membrane degradation and/or water generation due to oxygen crossover. The ratio between the normal and effective oxygen permeability is in a range between 0.927 ~ 0.933 under the fuel cell temperature conditions.

Nitrogen crossover was measured under various operating conditions and under open circuit voltage (OCV) and power generation conditions in PEMFCs. Under OCV conditions, nitrogen crossover increased with increasing cell temperature under all RH conditions. Nitrogen permeability coefficient (NPC) was calculated based on the obtained nitrogen concentration data and the NPC results fitted the form of Arrhenius expression. Under power generation conditions, nitrogen crossover increased with increasing current density. Moreover, when current density increased, the increases in the nitrogen crossover rates were found to be related to elevated membrane temperature and high water content.

Lastly, the effect of gas diffusion layer (GDL) structure on the membrane puncturing, the cell performance, hydrogen crossover and OCV of fuel cells were measured under various clamping torque conditions. The performances of fuel cells with GDL-1 (a carbon fiber felt substrate with micro-porous layer having rough surface) and GDL-3 (a carbon fiber paper substrate with micro-porous layer having smooth surface) are higher than that with GDL-2 (a

carbon fiber felt substrate with micro-porous layer having smooth surface). Hydrogen crossover of cells for all GDL samples increases with the increase of clamping torque, especially the degree of increase of GDL-1 is much greater than that of the other two GDL samples, implying that the penetration of carbon fibers of GDL-1 into membrane should be higher than that of the other two GDL samples. On the other hand, the cell with the GDL-3 is expected to have better durability than the other two GDLs, because the GDL-3 shows the minimum hydrogen crossover increase as clamping torque increases. The measurement of gas permeability could provide useful data and an insight into the selection of polymeric materials not only for membrane manufacturers, but also for fuel cell researchers understanding failure modes of membranes in operating fuel cells.

**Keywords: Polymer electrolyte membrane fuel cell, Gas crossover, Gas permeability coefficient, Local measurement, Gas diffusion layer penetration**

***Identification Number: 2007-20801***

# Contents

|  |              |
|--|--------------|
| <b>Abstract</b> .....  | <b>ii</b>    |
| <b>Contents</b> .....  | <b>vi</b>    |
| <b>List of Figures</b> .....                                       | <b>ix</b>    |
| <b>List of Tables</b> .....  | <b>xvii</b>  |
| <b>Nomenclature</b> .....  | <b>xviii</b> |
| <br>   |              |
| <b>Chapter 1. Introduction</b> .....                               | <b>17</b>    |
| 1.1 Background of the study .....                                  | <b>17</b>    |
| 1.2 Literature survey .....  | <b>20</b>    |
| 1.3 Objectives and scopes .....                                    | <b>25</b>    |
| <br>   |              |
| <b>Chapter 2. Experimental apparatus and method</b> .....          | <b>27</b>    |
| 2.1 Introduction .....   | <b>27</b>    |
| 2.2 Single fuel cell.....  | <b>27</b>    |
| 2.3 Experimental apparatus and test conditions .....               | <b>30</b>    |
| 2.4 Mass spectrometer.....   | <b>32</b>    |
| 2.5 Gas crossover theory.....                                      | <b>35</b>    |
| <br>   |              |
| <b>Chapter 3. Measurement of the hydrogen crossover rate</b> ..... | <b>38</b>    |
| 3.1 Introduction .....   | <b>38</b>    |

|  |  |           |
|--|--|-----------|
| 3.2  | Effect of operating conditions on hydrogen crossover ..... | 38        |
| 3.2.1  | Preparation of materials .....                             | 39        |
| 3.2.2  | Effect of the temperature .....                            | 41        |
| 3.2.3  | Effect of the relative humidity .....                      | 43        |
| 3.2.4  | Effect of the operating pressure .....                     | 45        |
| 3.2.5  | Effect of the membrane thickness .....                     | 47        |
| 3.2.6  | Multiple linear regression analysis .....                  | 50        |
| 3.2.7  | Numerical analysis of hydrogen crossover .....             | 56        |
| 3.3  | Local measurement of hydrogen crossover .....              | 63        |
| 3.3.1  | Preparation of new single fuel cell .....                  | 63        |
| 3.3.2  | Local hydrogen crossover distribution in a PEMFC.....      | 68        |
| 3.3.3  | Effects of operating conditions on hydrogen crossover..... | 74        |
| 3.4  | Summary .....  | 78        |
| <br><b>Chapter 4. Measurement of the oxygen crossover rate.....</b>    |  | <b>81</b> |
| 4.1  | Introduction .....   | 81        |
| 4.2  | New test procedure and method .....                        | 82        |
| 4.3  | Gas selectivity measurement .....                          | 86        |
| 4.4  | Quantitative measurements of oxygen crossover .....        | 89        |
| 4.5  | Measurement of effective oxygen permeability .....         | 93        |
| 4.6  | Summary .....  | 98        |
| <br><b>Chapter 5. Measurement of the nitrogen crossover rate .....</b> |  | <b>99</b> |

|  |            |
|--|------------|
| 5.1 Introduction .....   | 99         |
| 5.2 Characterization of nitrogen crossover under open circuit voltage conditions ..... | 99         |
| 5.2.1 Effect of operating condition on nitrogen crossover.....                         | 100        |
| 5.2.2 Nitrogen permeability coefficient.....   | 103        |
| 5.3 Characterization of nitrogen crossover under power generation conditions .....     | 109        |
| 5.3.1 Effect of current density on nitrogen crossover .....                            | 110        |
| 5.3.2 Effect of anode stoichiometric ratio on nitrogen crossover ....                  | 114        |
| 5.4 Summary .....  | 116        |
| <br>   |            |
| <b>Chapter 6. Gas crossover due to GDL penetration .....</b>                           | <b>118</b> |
| 6.1 Introduction .....   | 118        |
| 6.2 Materials and experimental setup.....  | 119        |
| 6.3 Electrochemical <i>I-V</i> performance of fuel cell .....                          | 127        |
| 6.4 Effect of hydrogen crossover on the OCV .....                                      | 134        |
| 6.5 Visual observation of the GDLs and MEA .....                                       | 141        |
| 6.6 Summary .....  | 143        |
| <br>   |            |
| <b>Chapter 7. Concluding remarks.....</b>  | <b>146</b> |
| <br>   |            |
| <b>References .....</b>  | <b>152</b> |
| <br>   |            |
| <b>Abstract (in Korean) .....</b>  | <b>163</b> |

## List of Figures

|            |  |    |
|------------|--|----|
| Figure 2.1 | Schematic diagram of the experimental setup used in this study<br>.....  | 28 |
| Figure 2.2 | Surface morphologies of the GDLs: (a) macro-porous substrate<br>and (b) micro-porous layer.....                    | 29 |
| Figure 2.3 | The schematic diagram of mass spectrometer used in this study<br>.....   | 33 |
| Figure 2.4 | The picture of the MS system used in this study.....   | 34 |
| Figure 3.1 | Hydrogen crossover rate as a function of cell temperature at 100%<br>RH and hydrogen pressure of 1.0 bar.....      | 42 |
| Figure 3.2 | Hydrogen crossover rate as a function of RH at 65°C and<br>hydrogen pressure of 1.0 bar.....                       | 44 |
| Figure 3.3 | Hydrogen crossover rate as a function of hydrogen pressure at<br>65°C and 100% RH.....                             | 46 |
| Figure 3.4 | Hydrogen crossover rates as a function of membrane thickness<br>under differing temperature and RH conditions..... | 48 |
| Figure 3.5 | Hydrogen crossover rates as a function of membrane thickness<br>under differing hydrogen pressure conditions.....  | 49 |
| Figure 3.6 | Relationship between inverse of logarithmic membrane<br>thickness and hydrogen crossover rate.....                 | 52 |
| Figure 3.7 | Comparison between measured and estimated values from MLR<br>model.....  | 53 |
| Figure 3.8 | Mesh configuration of single channel PEMFC geometry .....  | 58 |

|             |   |    |
|-------------|---|----|
| Figure 3.9  | The hydrogen mole fraction profiles in the whole area of fuel cell at the anode and cathode operating pressure of 1.0 and 1.0 bar, respectively .....   | 61 |
| Figure 3.10 | The hydrogen mole fraction profiles in the whole area of fuel cell at the anode and cathode operating pressure of 1.6 and 1.0 bar, respectively .....   | 62 |
| Figure 3.11 | Schematic representation of the single fuel cell used in this study: (a) an magnified view; (b) a photo of the fuel cell assembly for local measurement of hydrogen crossover .....                       | 65 |
| Figure 3.12 | Schematic diagram of the specially-designed bipolar plate for the cathode side.....   | 66 |
| Figure 3.13 | Local distribution of hydrogen crossover rate in fuel cell at a nitrogen flow rate of 0.5 LPM under a variety of temperature and RH conditions: cell temperatures of (a) 65°C, (b) 75°C and (c) 85°C..... | 71 |
| Figure 3.14 | Local distribution of hydrogen crossover rate in fuel cell under the various nitrogen flow rate conditions at 65°C and 100% RH .....  | 73 |
| Figure 3.15 | Total hydrogen crossover rates of the single fuel cell as a function of (a) cell temperature or (b) RH .....  | 76 |
| Figure 3.16 | Open circuit voltages of the single fuel cell as a function of (a) cell temperature or (b) RH .....   | 77 |
| Figure 4.1  | Schematic diagram of the oxygen crossover rate in a PEMFC.  | 83 |
| Figure 4.2  | Experimental raw data of oxygen crossover rates using   |    |

|            |  |     |
|------------|--|-----|
|            | hydrogen/ oxygen and helium/oxygen supplying gases.....  | 85  |
| Figure 4.3 | Oxygen concentration for different supplying gases under various temperature conditions .....  | 87  |
| Figure 4.4 | The oxygen concentration over a range of fuel cell temperatures at ambient pressure.....   | 90  |
| Figure 4.5 | Arrhenius plot of oxygen permeability as a function of temperature.....  | 91  |
| Figure 4.6 | Oxygen concentration in the anode exit stream using hydrogen and oxygen supplying gases.....   | 94  |
| Figure 4.7 | Arrhenius plots of normal and effective oxygen permeabilities  | 95  |
| Figure 4.8 | The effective oxygen crossover ratio under the various temperature conditions.....   | 96  |
| Figure 5.1 | Nitrogen concentration in the anode exit stream under various cell temperature at ambient pressure.....                                    | 101 |
| Figure 5.2 | Raw data of nitrogen concentration at anode exit stream under various relative humidity at ambient pressure .....                          | 102 |
| Figure 5.3 | Arrhenius plot of nitrogen permeability coefficient as a function of fuel cell temperature .....   | 105 |
| Figure 5.4 | Nitrogen permeability coefficient as a function of RH at ambient pressure .....  | 107 |
| Figure 5.5 | Comparison of nitrogen gas permeability coefficient with reported data.....  | 108 |
| Figure 5.6 | Nitrogen concentration in the anode exit stream under various current densities when hydrogen flow rate is 0.9 L min <sup>-1</sup> and air |     |

|            |   |     |
|------------|---|-----|
|            | flow rate is 2.0 L min <sup>-1</sup> .....  | 111 |
| Figure 5.7 | Calculated hydrogen consumption and the residual hydrogen flow rate at the exit under various current densities.....  | 112 |
| Figure 5.8 | Nitrogen crossover rate under various current densities when hydrogen flow rate is 0.9 L min <sup>-1</sup> and air flow rate is 2.0 L min <sup>-1</sup> .....   | 113 |
| Figure 5.9 | Nitrogen concentration in the anode exit stream under various anode stoichiometric ratios at ambient pressure with cathode stoichiometric ratio of 3.0 .....  | 115 |
| Figure 6.1 | Surface morphologies of macro-porous substrate and micro-porous layer observed by SEM with a 100× magnification: (a) macro-porous substrate and (b) micro-porous layer of GDL-1, (c) macro-porous substrate and (d) micro-porous layer of GDL-2, (e) macro-porous substrate and (f) micro-porous layer of GDL-3 | 125 |
| Figure 6.2 | The polarization curves under various clamping torque conditions for the GDL-1 sample: (a) RH is 100% and (b) 50% .....   | 128 |
| Figure 6.3 | The cell voltage variation at a current density of 1.6 A cm <sup>-2</sup> as a function of clamping torque .....  | 129 |
| Figure 6.4 | The polarization curves for all types of GDLs under a cell temperature of 65°C and fully humidified conditions: (a) clamping torque is 6.78 N m and (b) clamping torque is 15.8 N m .....   | 133 |
| Figure 6.5 | (a) Hydrogen concentration and (b) crossover rate at cathode exit   |     |

stream as a function of clamping torque. Anode H<sub>2</sub> flow and cathode N<sub>2</sub> flow rates are 0.9 and 0.5 L min<sup>-1</sup>, respectively.... 136

Figure 6.6 A proposed process of GDL substrate penetration into the MEA as clamping torque increases..... 137

Figure 6.7 OCV as a function of clamping torque when RH is 100% and cell temperature is 65°C at ambient gas pressure ..... 140

Figure 6.8 Cross-sectional SEM images of GDL-1 (a) before and (b) after the cell compression tests and in-plane surface SEM images of anode catalyst layer in MEA (c) before and (d) after the cell compression tests ..... 142

## List of Tables

|           |  |     |
|-----------|--|-----|
| Table 3.1 | Characteristics of the membranes used in this study.....   | 40  |
| Table 3.2 | Regression coefficients of the MLR model .....   | 54  |
| Table 3.3 | PEMFC model: governing equations .....   | 57  |
| Table 3.4 | Operating conditions used in this study .....  | 59  |
| Table 3.5 | Design parameters of the bipolar plate for the cathode side .....  | 67  |
| Table 5.1 | Calculated maximum permeability coefficient and the activation energy from the Arrhenius plot as a function of RH..... | 106 |
| Table 6.1 | Characteristics of GDLs used in this study .....   | 121 |

## Nomenclature

|           |   |
|-----------|---|
| <i>a</i>  | partial regression coefficient  |
| <i>A</i>  | active area [ $\text{cm}^2$ ]   |
| <i>C</i>  | concentration [%]   |
| <i>D</i>  | diffusion coefficient [ $\text{m}^2 \text{s}^{-1}$ ]                          |
| <i>E</i>  | activation energy [ $\text{kJ mol}^{-1}$ ]                                    |
| <i>F</i>  | Faraday constant [ $\text{C mol}^{-1}$ ]                                      |
| <i>FL</i> | Flow rate [ $\text{L min}^{-1}$ ]   |
| <i>I</i>  | current [A]   |
| <i>J</i>  | gas permeation rate [ $\text{mol s}^{-1} \text{cm}^{-2}$ ]                    |
| <i>k</i>  | permeability coefficient [ $\text{mol m}^{-1} \text{s}^{-1} \text{Pa}^{-1}$ ] |
| <i>l</i>  | membrane thickness [ $\mu\text{m}$ ]  |
| <i>N</i>  | flow rate [ $\text{L min}^{-1}$ ]   |
| <i>m</i>  | molar flow rate [ $\text{mol s}^{-1} \text{cm}^{-2}$ ]                        |
| <i>M</i>  | Molar weight [ $\text{g mol}^{-1}$ ]  |
| <i>P</i>  | partial pressure [Pa]   |
| <i>R</i>  | gas constant [ $\text{J mol}^{-1} \text{K}^{-1}$ ]                            |
| <i>RH</i> | relative humidity [%]   |
| <i>s</i>  | standard deviation  |
| <i>S</i>  | solubility coefficient [ $\text{mol m}^{-3}$ ]                                |
| <i>T</i>  | temperature [ $^{\circ}\text{C}$ ]  |
| <i>t</i>  | membrane thickness [ $\mu\text{m}$ ]  |
| <i>x</i>  | independent variable  |
| <i>y</i>  | estimated hydrogen crossover rate [ $\text{mol cm}^{-2} \text{s}^{-1}$ ]      |

## **Greek symbols**

|          |                                  |
|----------|----------------------------------|
| $\alpha$ | Effective oxygen crossover ratio |
| $\beta$  | standardized coefficient         |
| $\rho$   | density [ $\text{kg m}^{-3}$ ]   |

## **Superscript**

|     |              |
|-----|--------------|
| $A$ | anode side   |
| $C$ | cathode side |

## **Subscript**

|       |                |
|-------|----------------|
| $A$   | anode side     |
| $C$   | cathode side   |
| $C.O$ | cathode outlet |
| $i$   | inlet          |
| $e$   | outlet         |
| $N_2$ | nitrogen gas   |

# **Chapter 1. Introduction**

## **1.1 Background of the study**

Growing concerns about environmental issues and the passage of CO<sub>2</sub> emission regulations have produced demands for cleaner emission and more efficient vehicles. The use of polymer electrolyte membrane fuel cells (PEMFC) has been suggested as a means to meet such demands and as a means to provide a clean power source for transportation application in the future. PEMFC-based systems are particularly well suited for vehicle applications, as they do not exhaust pollutants. They have several other advantages such as high power density, high efficiency, and low operating temperature for a quick startup. Cost analyses conducted by several study groups have shown the potential of low cost fuel cell systems for use in commercial application.

Membranes are usually used as an electrolyte in polymer electrolyte membrane fuel cells (PEMFCs). The main functions of membranes are to transfer protons from the anode to the cathode in PEMFCs and form a barrier between the anode and cathode reactants. However, gases inevitably permeate through the membrane barrier, which is referred to as the ‘gas crossover’

phenomenon. Gas crossover occurs due to concentration and pressure gradients between the anode and cathode sides. The hydrogen concentration in the anode side is usually higher than that in the cathode side; thus hydrogen is transported from the anode to the cathode side by diffusion [1]. Nitrogen and oxygen are also transported from the cathode to the anode side in the same manner. There are several theories to explain the mechanism of gas crossover through the membrane. Yeager et al. [2] suggested a three-region structure model for a Nafion<sup>®</sup> membrane consisting of the fluorocarbon phase region, interfacial zone and ionic clusters formation region. They reported that gases permeate through Nafion<sup>®</sup> membranes in the intermediate region. Sakai et al. [3-4] suggested another theory of gas crossover by using an ionic cluster-network model. They claimed that the gas permeates mainly through the water-containing ion cluster regions of the membrane. However, these two mechanisms are still controversial because of the complexity of the membrane structure, as Kocha et al. [5] mentioned. Thus further research of the gas crossover mechanism is needed.

In this study, the experimental measurements of gas crossover ( $H_2$ ,  $O_2$  and  $N_2$ ) were conducted using a mass spectrometer. Firstly, the effects of various operating parameters on gas crossover were investigated. Local measurements of gas crossover were also conducted to investigate where the

gas crossover occurred. Measurements of oxygen and nitrogen crossover were carried out under the various operating conditions. Lastly, the effects of gas diffusion layer structure on the gas crossover fuel cells were measured. These results may be useful for fuel cell researchers understanding failure modes of membranes in operating fuel cells. Nitrogen crossover data are also useful in the development of a nitrogen crossover model that can be used to facilitate establishment of an efficient method for hydrogen recirculation systems.

## 1.2 Literature survey

Gas crossover is an unavoidable phenomenon in PEMFCs, having attracted much interest and research in recent years. Hydrogen crossover in fuel cells not only results in inefficient fuel utilization, but also leads to membrane degradations and other fuel-cell specific operational problems. Many studies were conducted to measure the hydrogen crossover rate through the membrane. Cheng et al. [6] measured the hydrogen crossover rate in high-temperature PEMFCs under various operating conditions by using a steady-state electrochemical method. Vilekar et al. [7] theoretically analyzed the role of hydrogen crossover in PEMFCs. They mentioned that hydrogen crossover can explain the entire potential loss from the standard-state reversible voltage of 1.23 V under open-circuit conditions. Inaba et al. [8] reported that hydrogen crossover is the main cause of membrane degradation. They suggested the possible degradation mechanisms due to hydrogen crossover: thermal degradation caused by heat generation upon direct combustion of hydrogen and oxygen, and chemical degradation by hydrogen peroxide. Bessarabov et al. [9] reported that hydrogen crossover lowers fuel cell efficiency and generated the oxygen activation, which degrades the membrane on the cathode side of the fuel cell. Nam et al. [10] numerically investigated

the effects of hydrogen crossover through the membrane in PEMFCs. Yuan et al. [11] observed hydrogen crossover using a linear sweep voltammetry method using Nafion® membranes with different thicknesses, and Francia et al. [12] investigated the applicability of the semi-empirical approach to the phenomena of hydrogen crossover in PEMFCs and analyzed the effect of temperature and membrane thickness on the hydrogen crossover rate.

Oxygen crossover also causes several problems relating to limiting the durability of PEMFCs. Willsau et al. [13] reported that oxygen crossover influenced to the electrochemical carbon corrosion in cathode gas diffusion layer (GDL). It is well known that the air/fuel boundary is created at the anode side if oxygen gas transported from cathode to anode side. This increases the potential of cathode higher than the open circuit voltage and quickly corrodes the carbon layer [14-15]. Another problem caused by oxygen crossover is membrane degradation [16-18]. Oxygen crossover does provide a means for the formation of peroxide and hydro-peroxide radicals, which can slowly deteriorate the membrane. Broka et al. [19] also measured the oxygen permeability through Nafion® 117 membrane and recast Nafion® film by means of gas chromatography at different values of temperature and gas relative humidity. The electrochemical monitoring technique is also used to measure the solubility and the diffusion coefficient of oxygen in a PEMFC

[20]. Peron et al. [21] reported a range of properties obtained by ex-situ and in-situ characterization methods including oxygen permeability coefficients.

Nitrogen crossover accumulates in the fuel cell's hydrogen recirculation system (HRS) and an excessive buildup of nitrogen lowers the hydrogen concentration, affecting fuel cell performance. During PEMFC operation, it would be advantageous to recycle the exhausted residual hydrogen. However nitrogen as well as hydrogen present in the anode exit stream due to nitrogen crossover from the cathode to the anode through the fuel cell's membrane. Current HRSs recycle all residual gases in the anode exit stream to the anode inlet without eliminating the inert nitrogen. If a nitrogen-hydrogen mixture is continuously recycled, the concentration of the supplied hydrogen is gradually lowers, affecting PEMFC performance. Therefore, purging of a certain amount of the recycling nitrogen-hydrogen mixture to the ambient atmosphere is required to prevent PEMFC performance degradation. However, frequent purging can lead to a waste of the hydrogen fuel, so an appropriate method of control of the purging process is necessary for fuel economy. Ahluwalia et al. [22] conducted a comprehensive simulation study on the buildup of nitrogen in anode channels. They reported that the steady-state nitrogen concentration in anode channels can reach 50~70% under low purge conditions. Kocha et al. [5] presented a mathematical model to predict the extent of nitrogen

accumulation along the anode flow fields.

As gas crossover causes the degradation of membrane, several measurement techniques including the time-lag method [4, 23-24], volumetric method [3], electrochemical monitoring method [5, 20-21, 25-26], and direct gas detection method using gas chromatography (GC) [19, 27] or mass spectrometry (MS) [28-32] have been employed to measure the gas crossover rate. Both time-lag and volumetric methods applied higher pressure at one side of the membrane, then the gas molecules started sorbing into the high-pressure side of the membrane (upstream), and subsequently diffuse to the opposite low-pressure side of the membrane (downstream). The time-lag method involved monitoring the transient accumulation of species due to permeation on a fixed volume present in a downstream reservoir [24], but the volumetric method obtained the flow rate in the downstream [3]. These two methods offered a simple and effective technique for determining the gas permeation rates, but were not conducted under the fuel cell operating conditions (i.e., wide humidity and temperature ranges). Therefore, the results from these methods may be limited to use on both numerical and experimental researches of PEMFCs. For in-situ measurements of the gas crossover rate under the fuel cell operating conditions, electrochemical monitoring and direct gas detection methods are employed. The electrochemical monitoring

technique is used that one of its sides is exposed to an acid solution with a counter electrode, and current is generated due to gas crossover, while a reactive gas is supplied to the other side of the membrane and is measured over time to estimate the gas crossover rates in the membrane, but it is still limited in actual operating conditions of PEMFCs due to not using the hydrogen and oxygen gases for the reactant gases. Another class of measuring the gas crossover rate of PEMFCs is using direct gas detection method. Recently, the direct gas detection methods using gas chromatography (GC) or mass spectrometry (MS) were suggested to measure the gas crossover rate under the actual fuel cell operating conditions. As illustration in Ref. [28], the direct gas detection system is connected at the exit of the conventional fuel cell system, indicating that the gas crossover rate under the actual fuel cell conditions can be measured. The measuring of the gas crossover rates in conditions as close as possible to the real situation of PEMFCs appears important; therefore, the direct gas detection method methods using GC or MS is more suitable for gas crossover measurements.

### **1.3 Objectives and scopes**

There are a lot of experimental and analytical studies on the gas crossover of the fuel cell because it is directly related to the membrane degradation. However, most of the studies were not conducted under the fuel cell operating conditions (i.e., wide humidity and temperature ranges). Therefore, the results from these methods may be limited to use on both numerical and experimental researches of PEMFCs. The objective of present study is to measure the gas crossover rate (hydrogen, oxygen, and nitrogen) of fuel cell in conditions as close as possible to the real situation of PEMFCs. Furthermore, the permeability coefficients of each gas are also analyzed under the various operating conditions.

In chapter two, the experimental setup and test conditions are summarized. Preparation and assembly of single fuel cell, the test station, and auxiliary components such as fuel supplying system, humidifying system, devices for measurement, and gas crossover measurement system are shown. Especially, gas crossover measurement system using a mass spectrometer was introduced in this chapter.

In chapter three, the results of hydrogen crossover rates were shown and discussed. The effect of temperature, RH, hydrogen pressure, and membrane

thickness on hydrogen crossover rate in a PEMFC was investigated. Furthermore, local measurements of the hydrogen crossover rate were also conducted using a single fuel cell with the specially-designed cathode bipolar plate.

In chapter four, the results of oxygen crossover rates which conducted by new measurement method were analyzed. The amount of oxygen that react with the hydrogen is compared with the conventional oxygen crossover rate. These oxygen crossover measurements were used to determine how fast membrane degradation occurs.

In chapter five, the effects of fuel cell temperature and relative humidity on nitrogen crossover were investigated. Nitrogen permeability coefficient as a function of RH was also analyzed.

In chapter six, the effect of GDL structure on the membrane puncturing, the cell performance, hydrogen crossover and OCV of fuel cells were measured under various clamping torque conditions. The morphological images of the GDLs and the catalyst layer in MEA have been analyzed by scanning electron microscopy (SEM) in connection with hydrogen crossover to elucidate the membrane puncturing process.

Finally, the concluding remarks were given along with the brief summarization of results and discussions.

## **Chapter 2. Experimental apparatus and method**

### **2.1 Introduction**

In order to measure the gas crossover rate in a PEMFC, it is need to modify the conventional fuel cell system to measure the gas crossover rates. Fig. 2.1 shows a schematic diagram of the experimental setup used in this study. When the gas crossover rate was measured, a flushing sequence was necessary to measure a small amount of gas crossover rate; thus, a flush line was constructed and combined with the conventional fuel cell test system.

### **2.2 Single fuel cell**

In this study, a single fuel cell composed of the membrane electrode assembly (MEA), gas diffusion layers (GDLs), bipolar plates with a 5-serpentine channel for both anode and cathode flow fields, gaskets and end plates was used. A commercially-available perfluorinated sulfonic acid MEA with an active area of 25 cm<sup>2</sup> was used. Both the anode and cathode of an MEA were composed of typical Pt/C catalysts, and the Pt loadings of the anode and cathode were both 0.4 mg Pt cm<sup>-2</sup>. A GDL sample with thickness of 276 ± 6 μm, the average of 100 measurements using a Mitutoyo thickness

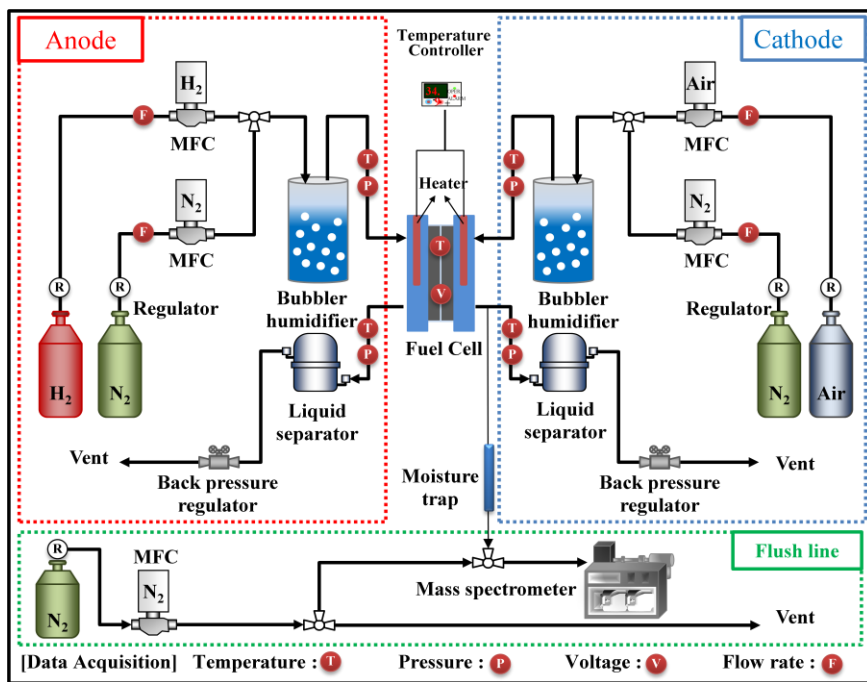
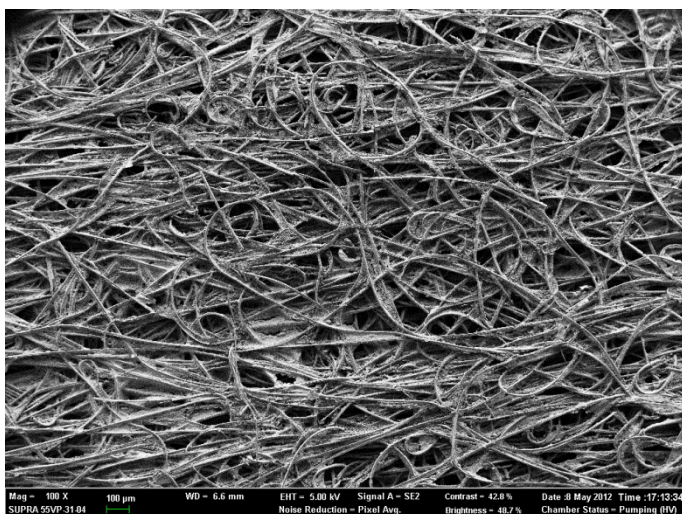
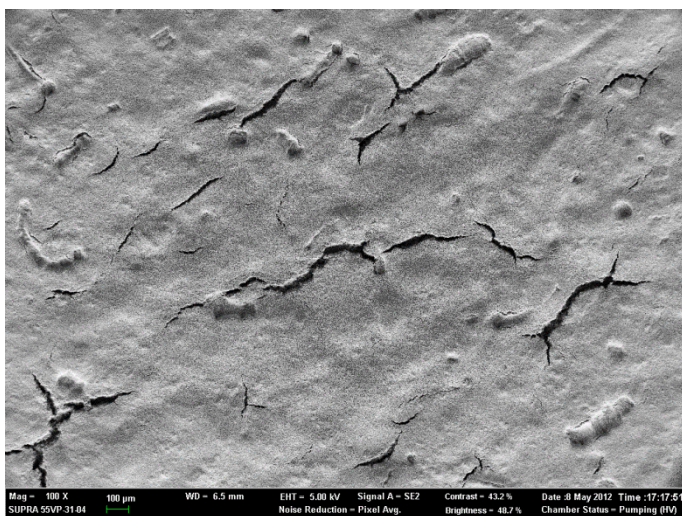


Fig. 2.1 Schematic diagram of the experimental setup used in this study



(a)



(b)

**Fig. 2.2** Surface morphologies of the GDLs: (a) macro-porous substrate and (b) micro-porous layer.

gauge (KWC 576 model, Mitutoyo Co., Japan), was obtained from a commercial manufacturer. The surface morphology of macro-porous substrate and MPL, which were both wet-proofed by hydrophobic treatment, of the pristine GDL sample was observed by SEM (SUPRA 55VP, Carl Zeiss, Weimar, Germany) with an accelerating voltage of 15 kV and a magnification of 100×. As shown in Fig. 2.2(a), the macro-porous substrate of the GDL sample exhibits a typical structure of carbon fiber felt. And as shown in Fig. 2.2(b), the MPL shows typical cracks on its surface, which is often observed in most commercial GDLs. Rubber type O-rings and Teflon<sup>®</sup> gaskets were used to prevent gas leakage. A torque wrench was used for fuel cell assembly. The torque wrench was set at 6.78 N m and the single cell assembly was compressed uniformly with the torque wrench. Before the tests were conducted, the compression pressure and uniformity of the fuel cell were checked using the pressure measurement film. A leak testing was performed after the fuel cell assembly process.

### **2.3 Experimental apparatus and test conditions**

The electrochemical performances of PEMFCs were measured by a commercial tester (1 kW test station, Chino Co., Korea). To measure an

operating temperature of the fuel cell, T-type thermocouples (TCs) with an uncertainty of  $\pm 0.5^{\circ}\text{C}$  were inserted into a long hole of 40 mm depth in both the anode and cathode bipolar plates, and the tube-shaped cartridge heaters were also inserted into both the anode and cathode end plates. The holes for the thermocouples were located 10 mm away from the center line of the MBP and 5 mm depth from the surface of MBP. Both TCs and heaters were connected to a temperature controller (UT 550, Yokogawa, Japan) to control the fuel cell temperature. Hydrogen and air were supplied to anode and cathode sides, respectively, to measure the fuel cell performance. All gas flow rates were controlled by mass flow controllers (Bronkhorst High-Tech, the Netherlands). The gas pressures of both the anode and cathode sides were monitored by pressure transducers. Uncertainties were estimated as  $\pm 0.15\%$  and  $\pm 0.1\%$  for gas pressure and mass flow measurements, respectively. Bubbler-type humidifiers were used for gas humidification. The inlet relative humidity (RH) values of 50%/50% (anode/cathode) and 100%/100% were used as partially and fully humidified operating conditions, respectively. An activation process was conducted first for 10 h to activate the fresh fuel cell under the following conditions: hydrogen (anode) and air (cathode) at ambient pressures with no back pressure; cell temperature of  $65^{\circ}\text{C}$ ; environment temperature of  $23^{\circ}\text{C}$ ; RH of 100%/100%; and stoichiometric ratios of anode

and cathode sides of 1.5 and 2.0, respectively. After the activation process, the fuel cell was characterized by measuring the current-voltage ( $I$ - $V$ ) polarization performance. An electric loader (PLZ 1004WA, Kikusui Electronics, Japan) was used to measure the  $I$ - $V$  curve of the single fuel cell. A differential pressure transducer (DPLH0100N, Sensys, Korea) was used to measure the pressure differences between the inlet and outlet.

## **2.4 Mass spectrometer**

The gas crossover rate through the PEMFC membrane was measured using an on-line HPR-20 QIC quadrupole mass spectrometer (Hiden Analytical, Warrington, UK). Fig. 2.3 shows the schematic diagram of the MS system used in this study and the picture of the MS system is shown in Fig. 2.4. As shown in Fig. 2.1, a flush line was added to fuel cell system to permit measurement of small amounts of gas crossover rates. Measuring such low levels of gas crossover rate is not easy due to the interference of the oxygen and nitrogen in the ambient air; thus, before gas crossover testing, a flushing sequence of at least three hours duration was used to eliminate the residual gas inside the mass spectrometer system [33]. After that flushing sequence, a residual gas sample containing a small amount of gas what we want to

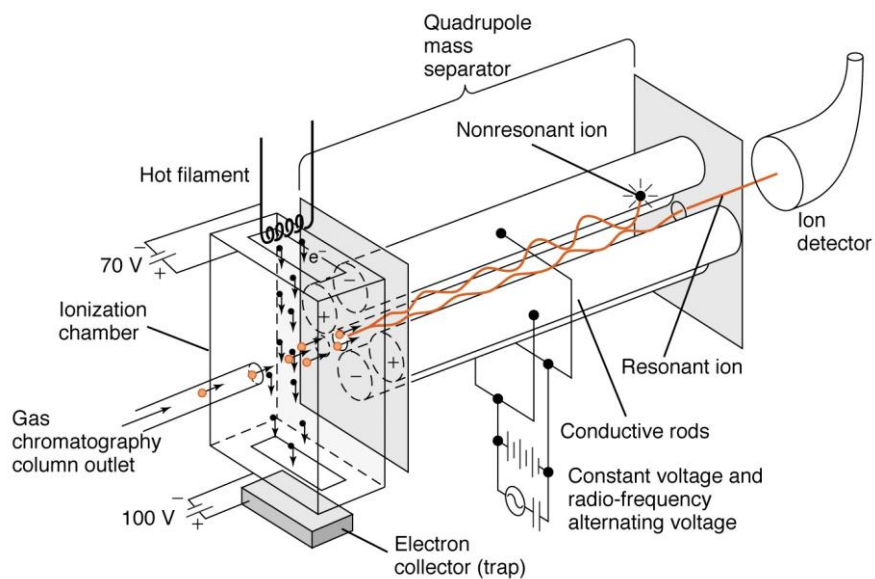


**Fig. 2.3** The schematic diagram of mass spectrometer used in this study.



**Fig. 2.4** The picture of the MS system used in this study.

measure was injected from the exit stream to the mass spectrometer via a 3-way valve (Fig. 1). For quantitative measurements with the mass spectrometer, the calibration process proposed by Bley et al. [34] was conducted.

## 2.5 Gas crossover theory

In a PEMFC, the concentration gradient across the membrane is the driving force for the gas to permeate from the one side to the other side, and under Fick's law, gas crossover across the membrane is considered as diffusion through a membrane. If we suppose a fuel cell system in a steady state, the concentration of gas remains constant at all surfaces of the membrane. Under that assumption, if we consider the hydrogen crossover, the one-dimensional diffusion equation from Fick's first law is expressed as below

$$J_{H_2} = D_{H_2} \cdot \frac{\partial C_{H_2}}{\partial x} = D_{H_2} \cdot \left( \frac{C_{H_2}^A - C_{H_2}^C}{l} \right) \quad (2.1)$$

where  $J_{H_2}$  is the hydrogen permeation rate,  $D_{H_2}$  is the hydrogen diffusion coefficient, and  $l$  is the membrane thickness.  $C_{H_2}^A$  and  $C_{H_2}^C$  are the surface hydrogen concentrations of the membrane at the anode and cathode, respectively. In a fuel cell system, the two surface hydrogen concentrations ( $C_{H_2}^A$  and  $C_{H_2}^C$ ) are not known, but the partial pressures of hydrogen on the

anode and cathode sides of the membrane,  $P_{H_2}^A$  and  $P_{H_2}^C$ , respectively, are known. Henry's law is used to quantify the solubility of a gas in a solvent with such solubility being directly proportional to the partial pressure of the gas above the solvent. That relationship is written as

$$C_{H_2} = S_{H_2} \cdot P_{H_2} \quad (2.2)$$

where  $C_{H_2}$  is the surface hydrogen concentration of the membrane in equilibrium with an external hydrogen partial pressure  $P_{H_2}$ , and in which  $S_{H_2}$  is the hydrogen solubility coefficient. Combining Eqs. (2.1) and (2.2), the permeation rate of hydrogen, when  $P_{H_2} = 0$ , is written as

$$J_{H_2}^{A \rightarrow C} = (D_{H_2} \cdot S_{H_2}) \cdot \left( \frac{P_{H_2}^A}{l} \right) = k_{H_2} \cdot \left( \frac{P_{H_2}^A}{l} \right) \quad (2.3)$$

$$k_{H_2} = D_{H_2} \cdot S_{H_2} = J_{H_2}^{A \rightarrow C} \cdot \left( \frac{l}{P_{H_2}^A} \right) \quad (2.4)$$

where  $k_{H_2}$  is the permeability coefficient of hydrogen. In Eq. (2.4), the hydrogen permeability coefficient is expressed as the product of the diffusion coefficient and the solubility coefficient [35]. It is calculated by measuring the permeation rate of hydrogen through the membrane for a given membrane thickness and a given partial pressure of hydrogen at the anode side. The output data of the mass spectrometer is the gas concentration in the residual outlet gas. It is assumed that there is no change in cathode flow rate between the inlet and outlet because the amount of gas that crosses over from the

cathode to anode during the measurements is expected to be too small to cause a significant drop in the outlet flow rate. The  $P_{H_2}^A$  is based on the anode inlet pressure, and hydrogen permeability coefficient can be calculated.

## **Chapter 3. Measurement of the hydrogen crossover rate**

### **3.1 Introduction**

Recently, thin membranes ranging from 18 to 50  $\mu\text{m}$  have been widely adopted in PEMFCs to improve efficiency and allow high current-density operations. However, the use of thin membranes facilitates gas crossover, and may reduce fuel cell durability. Hydrogen crossover is a direct loss of fuel cell efficiency, and is the main cause of membrane degradation: thermal degradation caused by heat generation upon direct combustion of hydrogen and oxygen, and chemical degradation by hydrogen peroxide. Furthermore, hydrogen crossover can explain the entire potential loss from the standard-state reversible voltage of 1.23 V under open-circuit conditions. Therefore, measurements of the hydrogen crossover rate need to be studied.

### **3.2 Effect of operating conditions on hydrogen crossover**

Firstly, the effect of operating conditions on hydrogen crossover was investigated. A number of factors are known to affect hydrogen crossover, such as operating temperature, relative humidity (RH), gas pressure, and

membrane thickness. As the permeability coefficient is usually expressed in terms of membrane thickness, the membrane thickness is also an important factor in the hydrogen crossover rate. However, the combined operational effects of temperature, RH, hydrogen pressure, and membrane thickness on hydrogen crossover rate have not been investigated. To the best of our knowledge, there are few comparative studies on the impact of various factors on the hydrogen crossover rate. The present study examined the effects of various operating parameters on hydrogen crossover rate, and compared the results via multiple linear regression (MLR) analysis. A parametric study of hydrogen crossover was also conducted by comparing the beta coefficients obtained from the MLR analysis.

### **3.2.1 Preparation of materials**

All Nafion<sup>®</sup> membranes used in the experiments were obtained from DuPont Co., and the thicknesses of all the membranes were measured at least 20 times per membrane sample, using a Mitutoyo thickness gauge (Mitutoyo Co., Japan). The average and standard deviation of the membrane thicknesses are summarized in Table 3.1.

A single fuel cell with an active area of 25 cm<sup>2</sup> was used in the

**Table 3.1** Characteristics of the membranes used in this study

| <b>Grade name</b> | <b>Sample code</b> | <b>Typical thickness (<math>\mu\text{m}</math>)</b> | <b>Measured thickness (<math>\mu\text{m}</math>)</b> |
|-------------------|--------------------|---|--|
| NRE211CS          | NRM-1              | 25.4  | $20.9 \pm 1.7$                                       |
| NR212             | NRM-2              | 50.8  | $63.4 \pm 1.4$                                       |
| N115              | NRM-3              | 127.0   | $134.8 \pm 5.9$                                      |
| N117              | NRM-4              | 183.0   | $179.8 \pm 6.9$                                      |
| N1110             | NRM-5              | 254.0   | $258.2 \pm 4.2$                                      |

measurements of hydrogen crossover rate. The single fuel cell consisted of a membrane, bipolar plates, gaskets, and end plates. Only the Nafion<sup>®</sup> membrane was sandwiched between the bipolar plates. The bipolar plates without flow fields were designed to eliminate the effect of compression pressure on hydrogen crossover rate. The depths of the anode and cathode sides were 0.6 and 0.9 mm, respectively. Rubber type O-rings and Teflon<sup>®</sup> gaskets were used to prevent gas leakage. A torque wrench was used during fuel cell assembly, and was set high enough to prevent gas leakage and to uniformly compress the fuel cell assembly.

### **3.2.2 Effect of the temperature**

Fig. 3.1 shows the hydrogen crossover rate in the cathode exit stream across all operating temperatures at 100% RH and hydrogen pressure of 1.0 bar. It is observed that the hydrogen crossover rate increases linearly with temperature for all membrane samples. This is because hydrogen permeability coefficient (expressed as the product of a diffusion coefficient and a solubility coefficient) increases as temperature increases. The diffusion coefficient increases with temperature as molecular movement of the gas becomes more active [28]. Thus, the increase in diffusion coefficient finally results in the

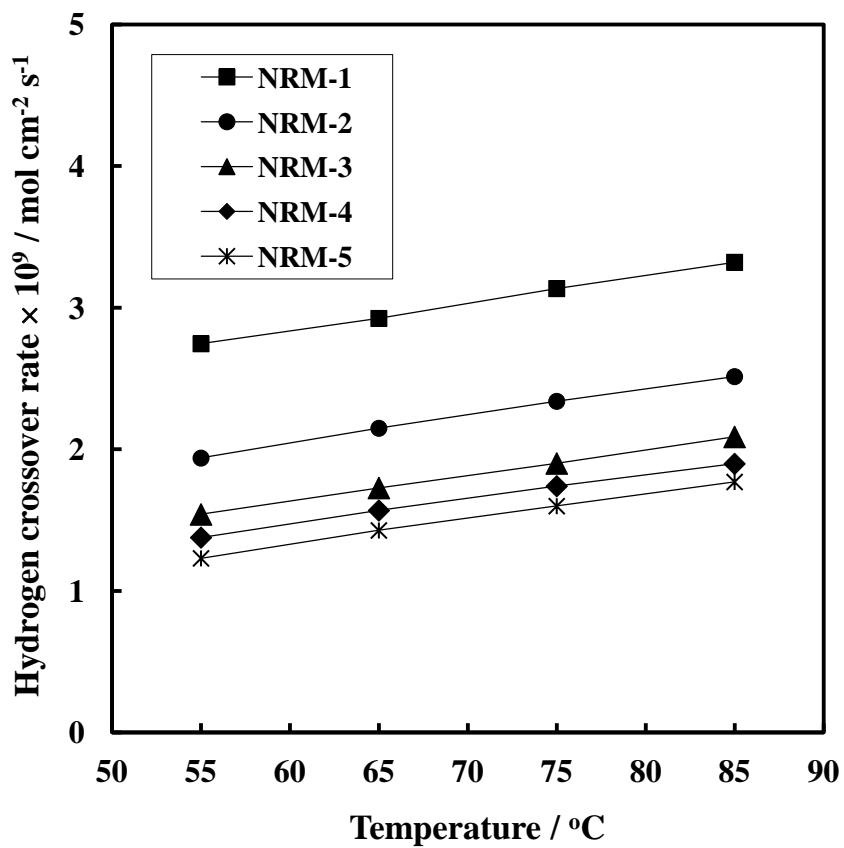


**Fig. 3.1** Hydrogen crossover rate as a function of cell temperature at 100% RH and hydrogen pressure of 1.0 bar

increase in hydrogen permeability coefficient, which affects the increase in hydrogen crossover rate. Cheng et al. [6] also reported the same trend as our results, i.e. hydrogen crossover rate increases with the increase in temperature. In Fig. 3.1, it is also seen that a greater increase in the rate of hydrogen crossover is observed for the thinnest NRM-1 membrane used in the study. Conversely, the hydrogen crossover rate for the NRM-5 sample (the thickest membrane) increases slowly as temperature increases. These results indicate that the amount of hydrogen crossover via the thickest membrane (NRM-5) may be less affected by temperature increase than that of the thinnest membrane (NRM-1).

### **3.2.3 Effect of the relative humidity**

Fig. 3.2 shows the hydrogen crossover rate as a function of RH at 65 °C and 1.0 bar for all membrane samples. Higher hydrogen crossover rates are observed at higher RH conditions for all membrane samples. Higher RH results in greater water content of the membrane, resulting in increased permeability coefficient of the membrane. Several studies investigated why gas crossover occurs largely at the hydrated membrane. Liu et al. [36] reported that when water is sorbed into the membranes, the intermolecular

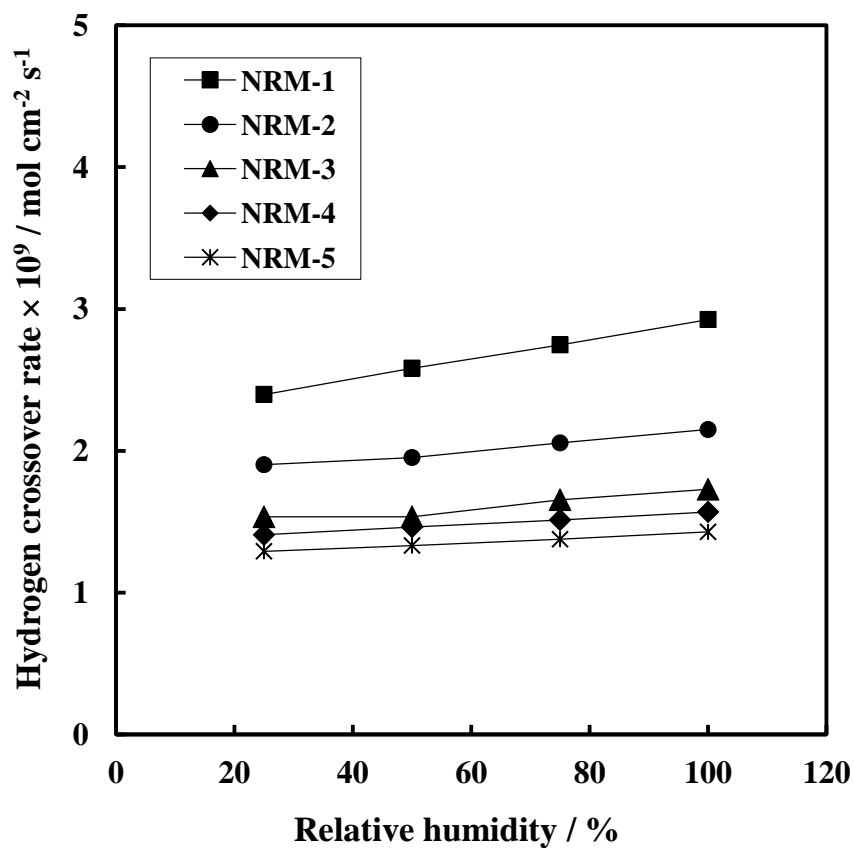


**Fig. 3.2** Hydrogen crossover rate as a function of RH at 65°C and hydrogen pressure of 1.0 bar

distance is increased between the polymer chains to enlarge the free volume, which offers additional pathways for hydrogen crossover. Sakai et al. [3] reported that the diffusion coefficient in hydrated Nafion<sup>®</sup> was 20 times greater than that in dry Nafion<sup>®</sup>. However, the solubility coefficient in hydrated Nafion<sup>®</sup> was half that for dry Nafion<sup>®</sup>. Thus, solubility decreases slightly and diffusivity increases remarkably, finally resulting in the increased permeability coefficient, when Nafion<sup>®</sup> is hydrated. Fig. 3.2 also shows that the hydrogen crossover rate of the thinnest membrane (NRM-1) may be more susceptible to the RH increase than that of the thickest membrane (NRM-5).

### **3.2.4 Effect of the operating pressure**

Fig. 3.3 shows hydrogen crossover rate as a function of hydrogen pressure at 65 °C and 100% RH. A proportional increase in the hydrogen crossover rate with increasing hydrogen pressure is observed for all membrane samples. Generally, the hydrogen partial pressure increases as hydrogen pressure increases. If the hydrogen partial pressure increases at the anode side of the fuel cell, the greater pressure differential between the anode and cathode sides leads to an increase in hydrogen crossover. Adachi et al. [37] examined the water permeability coefficient through Nafion<sup>®</sup> membranes

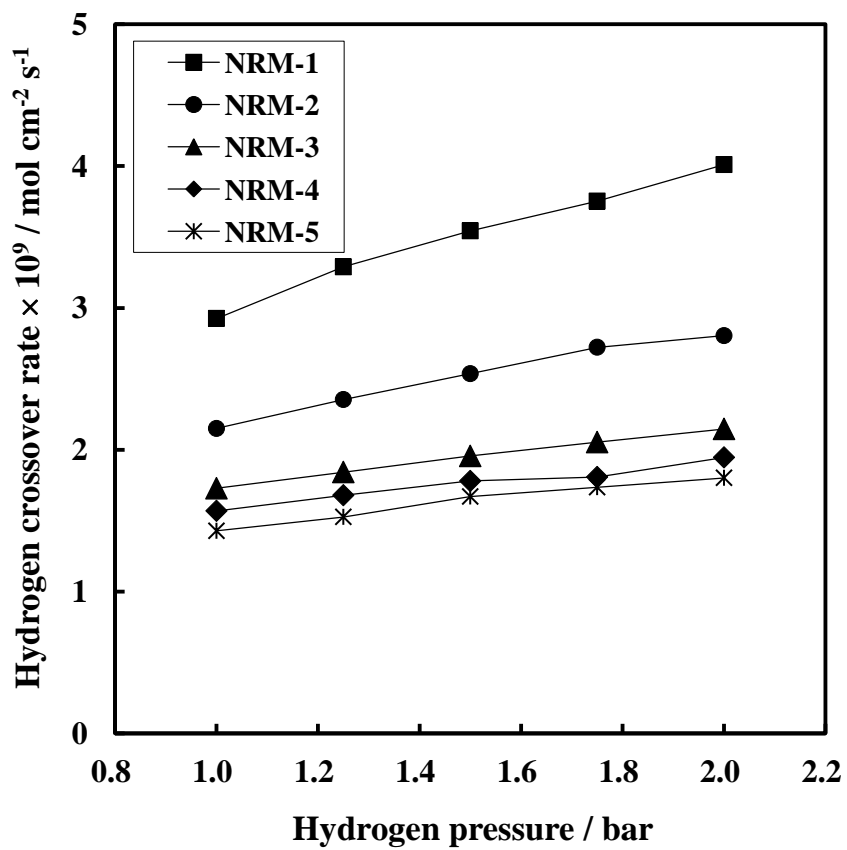


**Fig. 3.3** Hydrogen crossover rate as a function of hydrogen pressure at 65°C and 100% RH

ranging in thickness from 6 to 201  $\mu\text{m}$ . Similar to the trend of our results, greater hydrogen permeation was observed at higher hydrogen pressure conditions across all temperature conditions. Zhu et al. [38] conducted a similar hydrogen permeation test under different feed-gas partial pressures. They varied the hydrogen partial pressure by controlling the hydrogen and nitrogen contents of the feed gas. The trend reported for water flux through Nafion<sup>®</sup> membrane under differential pressure is also in good agreement with our results.

### **3.2.5 Effect of the membrane thickness**

In order to examine the effects of membrane thickness on hydrogen crossover rate, the hydrogen crossover rates are expressed as a function of membrane thickness. As shown in Figs. 3.4 and 3.5, higher hydrogen crossover rates are observed for the thinner membranes. In particular, the change in hydrogen crossover rate is significant for the thinner membranes (those ranging from 25 to 51  $\mu\text{m}$ ), whereas the hydrogen crossover rates are relatively unchanged for the thicker membranes (127 to 254  $\mu\text{m}$ ). The polymer membranes typically exhibit diffusion transport behavior; however, as the membranes become thinner, Knudsen transport behavior (the

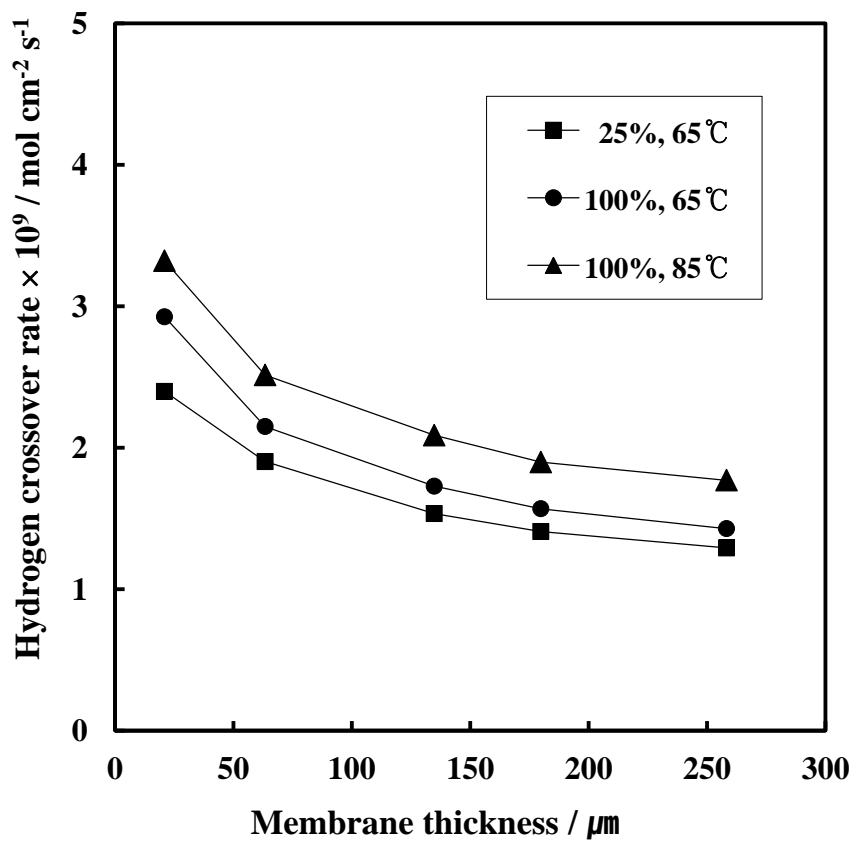


**Fig. 3.4** Hydrogen crossover rates as a function of membrane thickness under differing temperature and RH conditions

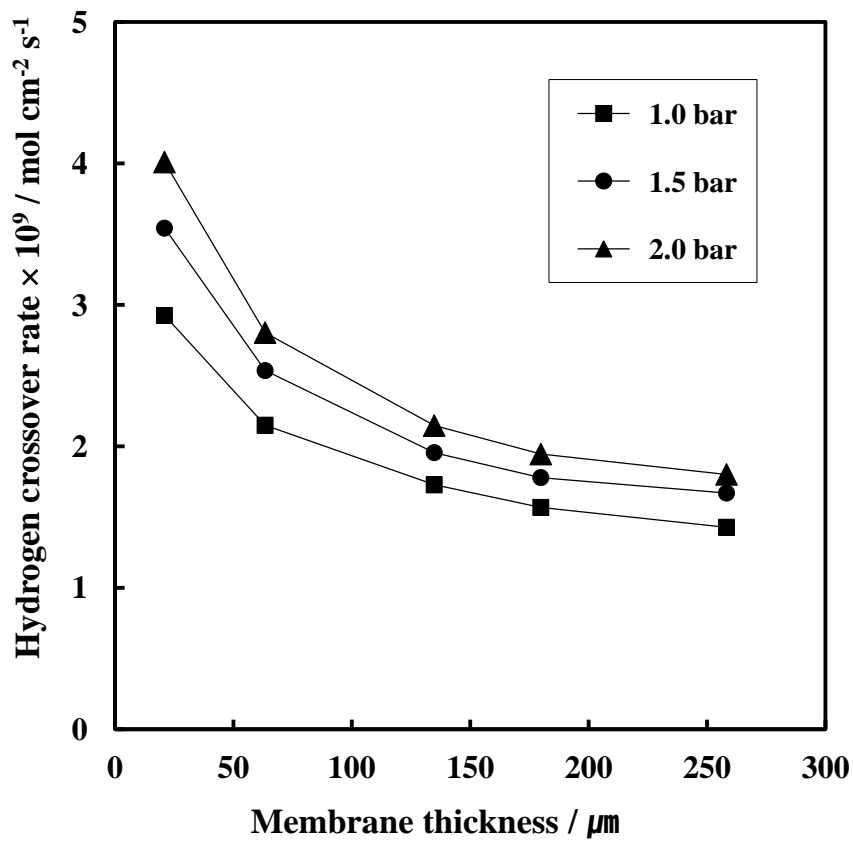


**Fig. 3.5** Hydrogen crossover rates as a function of membrane thickness under differing hydrogen pressure conditions

mechanism by which gases diffuse through porous materials) predominates [39]. Generally, transport through pores (*i.e.*, Knudsen transport behavior) is much faster than permeation through the membrane by the diffusion mechanism; this explains why the hydrogen crossover rate increases for the thinner membranes. However, Knudsen behavior is negligible in thicker membranes, resulting in relatively low hydrogen crossover rates. Yuan et al. [11] showed the effect of membrane thickness on hydrogen crossover rate before and after degradation tests. They reported no significant change in hydrogen crossover rate for the thicker membranes following degradation, whereas crossover rate increased greatly for the thinner membranes. Their results indicate that thinner membranes facilitate hydrogen permeation, which is in good agreement with our findings. Zhang et al. [40] also reported that hydrogen crossover rate through a thicker membrane (Nafion<sup>®</sup> 117) was less than that through a thinner membrane (Nafion<sup>®</sup> 112).

### **3.2.6 Multiple linear regression analysis**

Multiple linear regression (MLR) using SPSS statistical software (version 18.0) was performed to provide parametric analysis in this study. Regression analysis is widely used to understand the relationships of

independent variables to a dependent variable, as well as to predict the forms of empirical models [41-42]. The general form of MLR [43] is shown in Eq. (3.1)

$$y = a_0 + a_1 \cdot x_1 + a_2 \cdot x_2 + \dots + a_n \cdot x_n \quad (3.1)$$

where  $y$  is the estimated value,  $a_0$  is the regression constant,  $a_1 \sim a_n$  are the partial regression coefficients, and  $x_1 \sim x_n$  are the independent variables. In this study, we use four independent variables: temperature, RH, hydrogen pressure, and membrane thickness. Figs. 3.1 ~ 3.3 show a proportional relationship between hydrogen crossover rate and operating parameters (*i.e.*, temperature, RH, and hydrogen pressure). In Fig. 3.6, a linear relationship ( $R^2$  is about 0.99) is also observed, thus Eq. (3.1) becomes

$$y = a_0 + a_1 \times T + a_2 \times RH + a_3 \times P_{H_2} + a_4 \times (\ln t)^{-1} \quad (3.2)$$

where  $y$  is the estimated hydrogen crossover rate,  $a_0$  is the regression constant,  $a_1, a_2, a_3, a_4$  are the partial regression coefficients,  $T$  is temperature,  $RH$  is relative humidity,  $P_{H_2}$  is hydrogen pressure, and  $t$  is membrane thickness.

The comparison between measured and estimated values from the MLR model is shown in Fig. 3.7. The MLR model predicts the hydrogen crossover rate within 20% error. The  $R^2$  value for the final MLR model is 0.925, and the regression coefficients produced as an output of MLR analysis are listed in

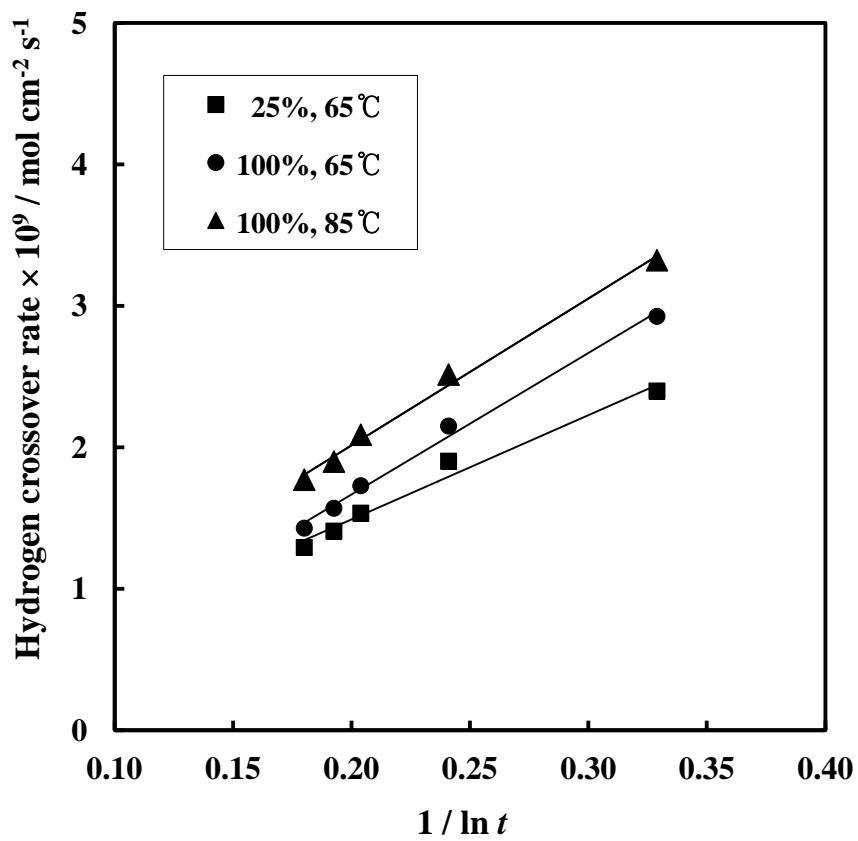


**Fig. 3.6** Relationship between inverse of logarithmic membrane thickness and hydrogen crossover rate

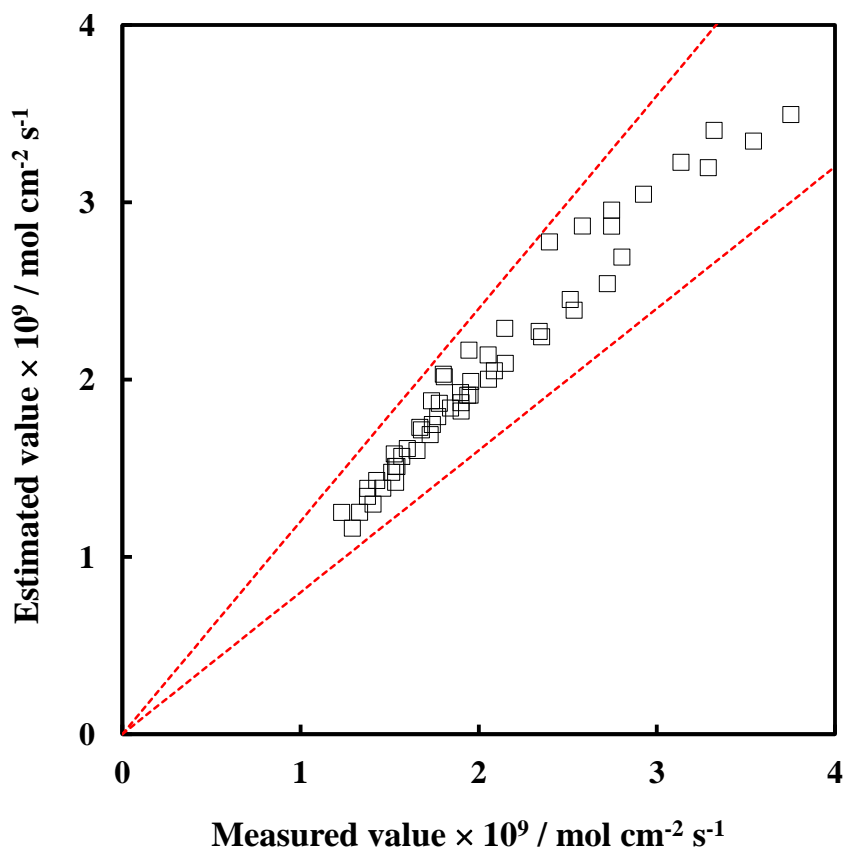


**Fig. 3.7** Comparison between measured and estimated values from MLR model

**Table 3.2** Regression coefficients of the MLR model

| No. |                | Unstandardized Coefficients |            | Standardized Coefficients |
|-----|----------------|-----------------------------|------------|---------------------------|
|     |                | $a_n$                       | Std. Error | $\beta$                   |
| 0   | (Constant)     | -2.6492                     | 0.2256     |                           |
| 1   | $T$            | 0.0180                      | 0.0028     | 0.078                     |
| 2   | $RH$           | 0.0036                      | 0.00085    | 0.138                     |
| 3   | $P_A$          | 0.5992                      | 0.0610     | 0.313                     |
| 4   | $(\ln t)^{-1}$ | 10.840                      | 0.3495     | 0.893                     |

Table 3.2. The first part of Table 3.2 estimates the unstandardized coefficient (*i.e.*, partial regression coefficient,  $a_n$ ), and indicates the individual contribution of each predictor to the model. These  $a_n$  values explain the relationship between hydrogen crossover rate and each variable. The standardized coefficients (beta coefficient) in the multiple regression analysis identify which independent variables have the greatest effect on the dependent variable, irrespective of differing units of measurement. The effect of the standardization is to remove the influence of units and place all parameters on an equal level [44]. The parameters are therefore directly comparable, and provide a better insight into the ‘importance or impact’ of a parameter in the model. The beta coefficients are calculated using Eq. (3.3)

$$\frac{\hat{y} - \bar{y}}{s} = \sum_k \left[ \frac{b_k s_k}{s} \right] \cdot \frac{Z_k - \bar{Z}_k}{s_k} \quad (3.3)$$

where each  $Z_k$  is a function of ( $X_1 \sim X_4$ ),  $s$  is the standard deviation of the output, and  $s_k$  is the standard deviation of the input [44]. A parametric study of hydrogen crossover using the parameters  $T$ ,  $RH$ ,  $P_{H_2}$ , and  $(\ln t)^{-1}$  was conducted in comparison with these beta coefficients. Of the parameters affecting hydrogen crossover, the highest beta coefficient ( $\beta_4 = 0.893$ ) was found for the inverse of the logarithmic membrane thickness, implying that the effect of membrane thickness on hydrogen crossover is dominant.

Similarly, the beta coefficients indicated that hydrogen pressure ( $\beta_3 = 0.313$ ) had a greater effect on hydrogen crossover than that of RH ( $\beta_2 = 0.138$ ) or temperature ( $\beta_1 = 0.078$ ). Lastly, RH has a higher beta coefficient than that of temperature. Consequently, increase in hydrogen crossover rate is predominantly determined by the inverse of the logarithmic membrane thickness, followed by hydrogen pressure, RH, and temperature, respectively.

### **3.2.7 Numerical analysis of hydrogen crossover**

The effect of operating conditions on hydrogen crossover was numerically investigated in this section. The governing equations of the PEMFC model, relevant source terms, and electrochemical properties at the anode and cathode CLs are summarized in Tables 3.3. The PEMFC model is numerically implemented in a commercial computational fluid dynamics (CFD) program, CCM+, basing on its user defined functions (UDF). Fig. 3.8 shows the mesh configuration of the simple single-straight channel geometry. The operating conditions are given in Table 3.4.

Fig. 3.9 shows the hydrogen mole fraction profiles in the whole area of fuel cell at the anode and cathode operating pressure of 1.0 and 1.0 bar, respectively. It is observed that hydrogen permeates from the anode to cathode

**Table 3.3** PEMFC model: governing equations

| <b>Governing equations</b> |   |
|----------------------------|---|
| Mass                       | $\frac{\partial(\rho u)}{\partial x} + \frac{\partial(\rho v)}{\partial y} + \frac{\partial(\rho w)}{\partial z} = S_m$ $u \frac{\partial(\rho u)}{\partial x} + v \frac{\partial(\rho u)}{\partial y} + w \frac{\partial(\rho u)}{\partial z} = -\frac{\partial P}{\partial x} + \frac{\partial}{\partial x} \left( \mu \frac{\partial u}{\partial x} \right) + \frac{\partial}{\partial x} \left( \mu \frac{\partial u}{\partial y} \right) + \frac{\partial}{\partial x} \left( \mu \frac{\partial u}{\partial z} \right) + S_{px}$  |
| Momentum                   | $u \frac{\partial(\rho v)}{\partial x} + v \frac{\partial(\rho v)}{\partial y} + w \frac{\partial(\rho v)}{\partial z} = -\frac{\partial P}{\partial x} + \frac{\partial}{\partial x} \left( \mu \frac{\partial v}{\partial x} \right) + \frac{\partial}{\partial x} \left( \mu \frac{\partial v}{\partial y} \right) + \frac{\partial}{\partial x} \left( \mu \frac{\partial v}{\partial z} \right) + S_{py}$ $u \frac{\partial(\rho w)}{\partial x} + v \frac{\partial(\rho w)}{\partial y} + w \frac{\partial(\rho w)}{\partial z} = -\frac{\partial P}{\partial x} + \frac{\partial}{\partial x} \left( \mu \frac{\partial w}{\partial x} \right) + \frac{\partial}{\partial x} \left( \mu \frac{\partial w}{\partial y} \right) + \frac{\partial}{\partial x} \left( \mu \frac{\partial w}{\partial z} \right) + S_{pz}$ |
| Energy                     | $\frac{\partial(\rho v)}{\partial t} + \frac{\partial(\rho u h)}{\partial x} + \frac{\partial(\rho v h)}{\partial y} + \frac{\partial(\rho w h)}{\partial z} = \frac{\partial}{\partial x} \left( k \frac{\partial T}{\partial x} \right) + \frac{\partial}{\partial y} \left( k \frac{\partial T}{\partial y} \right) + \frac{\partial}{\partial z} \left( k \frac{\partial T}{\partial z} \right) + S_{hp} + S_{he}$  |
| Gas crossover              | $J = -D \frac{dC}{dy} + v \frac{dP}{dy}$  |

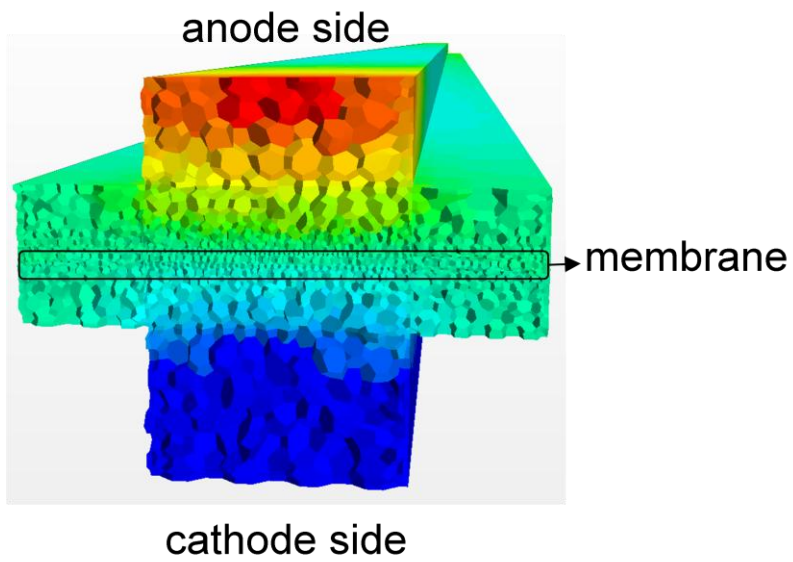


**Fig. 3.8** Mesh configuration of single channel PEMFC geometry.

**Table 3.4** Operating conditions used in this study.

| <b>Conditions</b>        | <b>Value</b>                   |                |
|--------------------------|--------------------------------|----------------|
|                          | <b>Anode</b>                   | <b>Cathode</b> |
| Relative humidity        | 100%                           | 100%           |
| Pressure                 | 1.0/1.6 bar                    | 1.0 bar        |
| Stoichiometric ratio     | 1.5                            | 2.0            |
| Channel (width × height) | 1.0 × 0.4 mm                   | 1.0 × 0.6 mm   |
| Temperature              | 65°C                           |                |
| Membrane                 | Nafion 211 (thickness : 25 μm) |                |
| Nafion dry density       | 1980 kg/m <sup>3</sup>         |                |
| Nafion equivalent weight | 1.1 kg/mol                     |                |
| GDL porosity             | 0.7                            |                |
| GDL thickness            | 278 μm                         |                |

sides by diffusive transport because the anode and cathode pressure is the same. As the hydrogen gas transported, the increased mole fraction of hydrogen is observed and accumulated in the cathode channel, finally resulting in a high mole fraction at the outlet regions. Fig. 3.10 shows the hydrogen mole fraction profiles in the whole area of fuel cell at the anode and cathode operating pressure of 1.6 and 1.0 bar, respectively. Because the pressure at the anode side is higher than that at the cathode side, hydrogen permeates to the cathode by diffusive and also by convective transport. It is shown that higher hydrogen mole fraction is observed in Fig. 3.10 due to the convective transport.

• Hydrogen crossover ( $P_A = 1.0$  bar,  $P_C = 1.0$  bar)

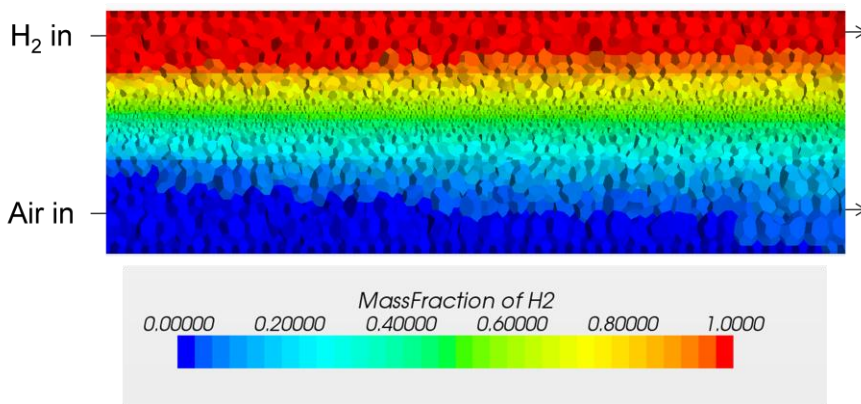


**Fig. 3.9** The hydrogen mole fraction profiles in the whole area of fuel cell at the anode and cathode operating pressure of 1.0 and 1.0 bar, respectively.

- Hydrogen crossover ( $P_A = 1.6$  bar,  $P_C = 1.0$  bar)

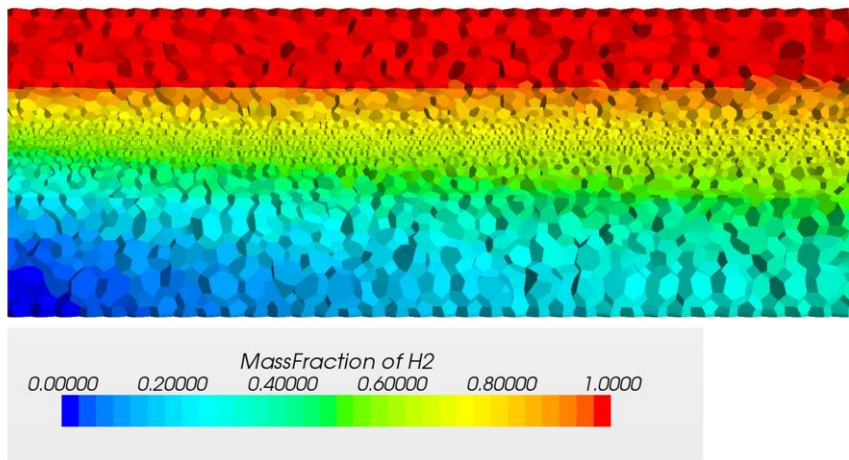


**Fig. 3.10** The hydrogen mole fraction profiles in the whole area of fuel cell at the anode and cathode operating pressure of 1.6 and 1.0 bar, respectively.

### **3.3 Local measurement of hydrogen crossover**

To design highly-durable stacks for fuel cell vehicle applications, the local distribution of the hydrogen crossover rate in fuel cells needs to be understood in depth, because hydrogen crossover can cause local degradations of the membrane. However, most of local measurement studies have been applied to measure the local current in the PEMFC rather than the local gas crossover rate [45-50]. Local measurements of the hydrogen crossover rate can elucidate where membrane degradations occur. Therefore, local measurements of the hydrogen crossover rate need to be studied. In this study, local measurements of the hydrogen crossover rate in PEMFCs have been conducted to analyze the distribution of the hydrogen crossover rate under various temperature and RH conditions. Furthermore, the effects of operating conditions on hydrogen crossover are investigated.

#### **3.3.1 Preparation of new single fuel cell**

A single PEMFC with an active area of 25 cm<sup>2</sup> was used for the local measurements of the hydrogen crossover rate in this study. The graphite bipolar plates with serpentine flow channels were used for both anode and cathode flow fields. As shown in Fig. 3.8(a), the single PEMFC consisted of

end plates, graphite bipolar plates, gas diffusion layers (GDLs), gaskets and a membrane electrode assembly (MEA). Bipolar plates and end plates were specially designed for local measurements of the hydrogen crossover rate. A GDL sample with a nominal thickness of 325  $\mu\text{m}$  was obtained from a commercial manufacturer, and consisted of both a micro-porous layer and a macro-porous substrate, which were both wet-proofed by hydrophobic treatment. The macro-porous substrate of the GDL sample was made from carbon fiber papers. Commercially-available perfluorinated sulfonic acid MEA was used in this study. Both the anode and cathode of the MEA were composed of typical Pt/C catalysts, and the Pt loadings of the anode and cathode were both 0.4 mg Pt  $\text{cm}^{-2}$ . Rubber type O-rings and Teflon<sup>®</sup> gaskets were also used to prevent gas leakage. A torque wrench, set at 6.78 N m, was used to uniformly compress the single cell assembly. A photo of the single fuel cell used in this study is shown in Fig. 3.8(b). For local measurements of the hydrogen crossover rate in the PEMFC, a bipolar plate was specially designed for the cathode side, as shown in Fig. 3.9. The anode bipolar plate was composed of conventional five-serpentine flow fields, while the cathode bipolar plate was modified to have parallel and five-serpentine flow fields with gas sampling ports. The cathode flow field had a channel width and depth of 1.0 and 0.9 mm, respectively, and the land width was 1.0 mm. The

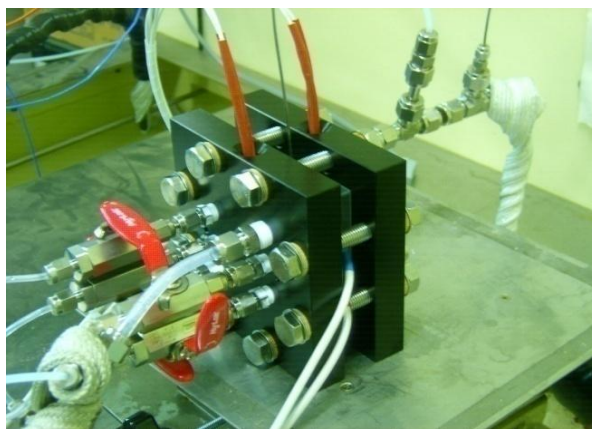
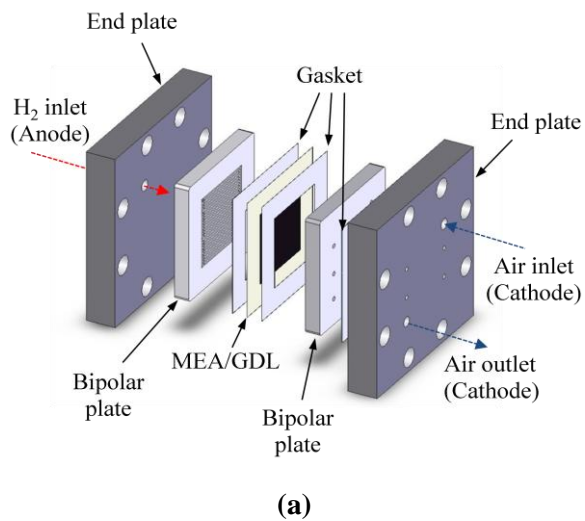


**Fig. 3.11** Schematic representation of the single fuel cell used in this study: (a) an magnified view; (b) a photo of the fuel cell assembly for local measurement of hydrogen crossover

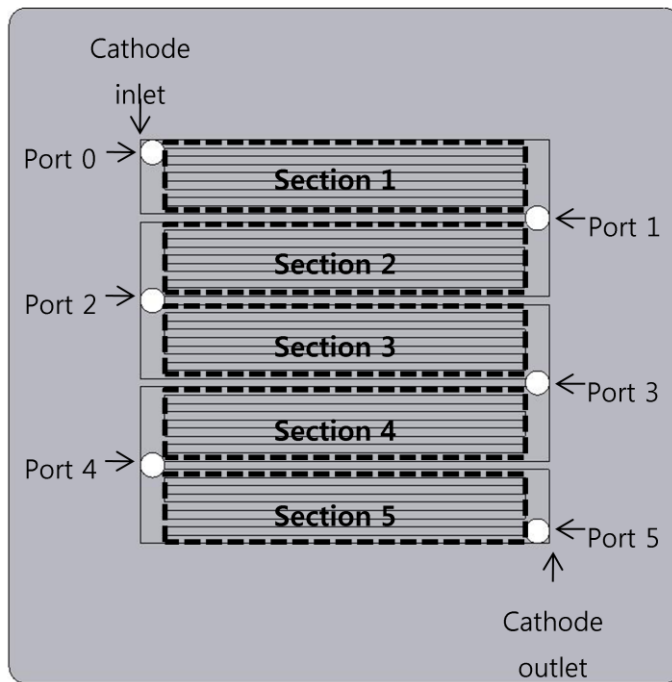


**Fig. 3.12** Schematic diagram of the specially-designed bipolar plate for the cathode side

**Table 3.5** Design parameters of the bipolar plate for the cathode side

| <b>Parameter</b> | <b>Value</b>       |
|------------------|--------------------|
| Active area      | 25 cm <sup>2</sup> |
| Channel width    | 1 mm               |
| Land width       | 1 mm               |
| Channel depth    | 0.9 mm             |
| Port diameter    | 3 mm               |

design parameters of the bipolar plate for the cathode side are detailed in Table 3.3. In addition to the conventional cathode inlet (port 0) and outlet (port 5), as shown in the Fig. 3.9, the cathode bipolar plate contains four more ports (1 ~ 4), which are used to sample the gas precisely. In the present study, the six ports (0 ~ 5) were used to sample the gas. The six sampling ports were located at regular intervals along the cathode flow field, and the local distribution of the hydrogen crossover rate in the fuel cell was analyzed by measurements of the hydrogen crossover rate at each gas sampling port.

As shown in Fig. 3.9, the flow field of the cathode side is divided by five sections along the flow field with an area of  $5 \text{ cm}^2$  per each section. The amount of hydrogen crossover in section 5 was obtained by subtracting the amount of hydrogen crossover detected at port 4 from that at port 5, and then converted into the hydrogen crossover rate by dividing the crossover amount by the sampling area. The hydrogen crossover rates of the other four sections were also measured similarly.

### **3.3.2 Local hydrogen crossover distribution in a PEMFC**

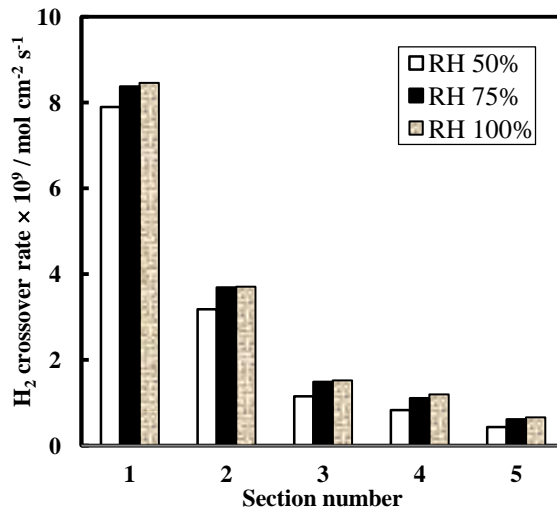
Fig. 3.10 represents the local distribution of the hydrogen crossover rate in the fuel cell under a variety of temperature and RH conditions. As shown in

Fig. 3.10, the hydrogen crossover rate decreases as the section number increases, that is, along the locations starting from the inlet towards the outlet regions. This result indicates that hydrogen crossover largely occurs near the inlet region, and reduced crossover amounts near the outlet region, presumably due to the partial pressure gradient of hydrogen. In this study, local measurements of the hydrogen crossover rate were conducted by supplying hydrogen and nitrogen for the anode and cathode sides, respectively. This means that the supply gases are not consumed electrochemically in the fuel cell because there is no electrochemical reaction. Furthermore, other operating parameters such as temperature and RH are also the same, whereas the gas pressure between the inlet and outlet of the flow field is different because of the pressure gradient between the inlet and outlet, which is needed to make the gas flow. Zhou et al. [51] reported that the gas pressure distribution along the channel varies almost linearly. Therefore, it is assumed that the hydrogen gas pressure distribution of the anode side is linear from the inlet to outlet of the flow field. Generally, the partial pressure of hydrogen on the anode side of the MEA increases as the hydrogen gas pressure increases. The increase in the partial pressure of hydrogen leads to the increase in the hydrogen permeation rate, as shown in Eq. (3.4). Hydrogen permeation rate is derived from Fick's law and is written as

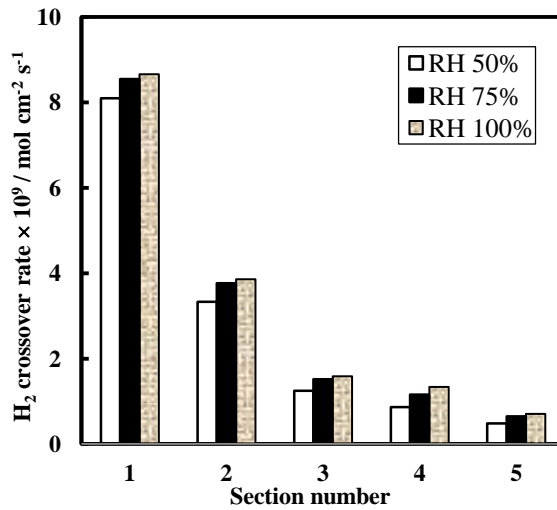
$$J_{H_2}^{A \rightarrow C} = k_{H_2} \cdot \left( \frac{P_{H_2}^A}{l} \right) \quad (3.4)$$

where  $J_{H_2}^{A \rightarrow C}$  is the permeation rate of hydrogen,  $k_{H_2}$  is the permeability coefficient of hydrogen,  $P_{H_2}^A$  is the partial pressure of hydrogen at the anode side and  $l$  is the membrane thickness. Accordingly, hydrogen crossover is more likely to occur near the inlet due to the high partial pressure of hydrogen. Therefore, the partial pressure gradient of hydrogen is considered one of reasons for the local variation of hydrogen crossover in the fuel cell. This means that other parameters, such as the permeability coefficient of hydrogen, do not affect the hydrogen crossover distribution because their values are the same over the whole area of the membrane. Hydrogen crossover is the main reason for membrane degradation. Matsuura et al. [52] measured the membrane thickness from the inlet to the outlet after an aging test of a fuel cell. They reported that the membrane near the inlet was clearly thinner than those at other locations. This result can support our experimental results that hydrogen crossover largely occurs near the inlet region rather than at the outlet region. Although the low RH near the inlet region may cause the membrane thinning, as suggested in the literature [52], the increase in hydrogen crossover near the inlet region can accelerate membrane thinning, as it did in this study.

In order to clarify the dependency of local hydrogen crossover behavior

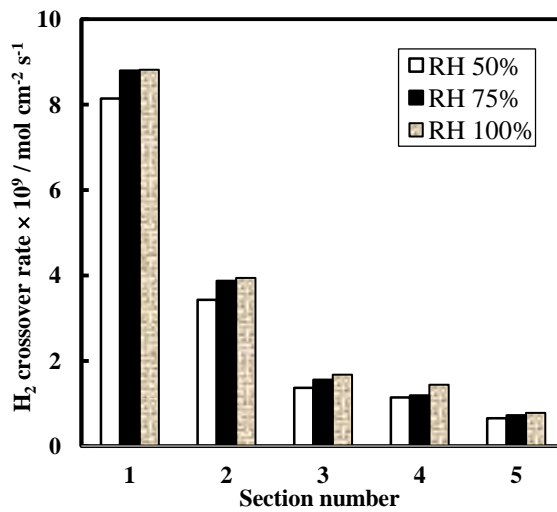


(a)



(b)

**Fig. 3.13** Local distribution of hydrogen crossover rate in fuel cell at a nitrogen flow rate of 0.5 LPM under a variety of temperature and RH conditions: cell temperatures of (a) 65°C, (b) 75°C and (c) 85°C



(c)

**Fig. 3.13** Local distribution of hydrogen crossover rate in fuel cell at a nitrogen flow rate of 0.5 LPM under a variety of temperature and RH conditions: cell temperatures of (a) 65°C, (b) 75°C and (c) 85°C

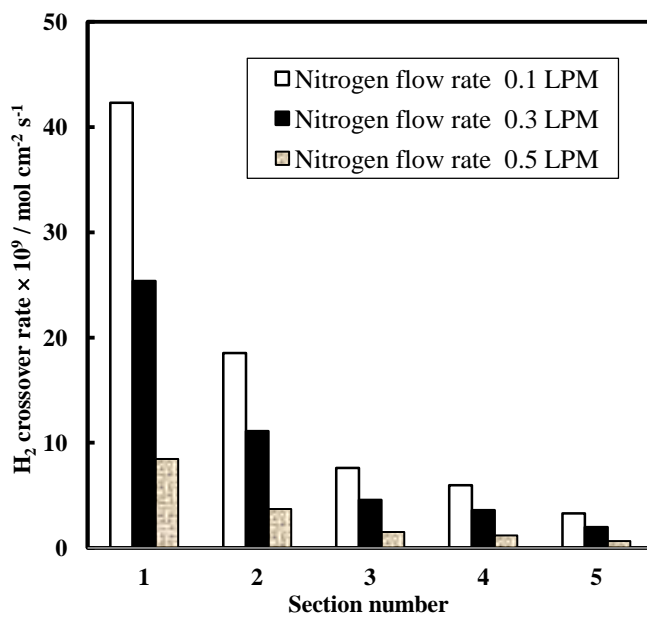


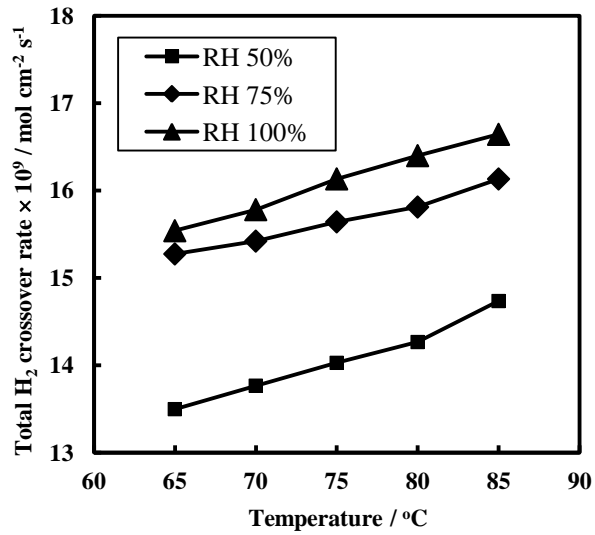
**Fig. 3.14** Local distribution of hydrogen crossover rate in fuel cell under the various nitrogen flow rate conditions at 65°C and 100% RH

on the nitrogen flow rate at cathode, we measured the local distribution of hydrogen crossover rates under a variety of nitrogen flow rates at 65°C and 100% RH, as shown in Fig. 3.11. The hydrogen crossover rates increase with decreasing the nitrogen flow rates at a given section, but the tendency of higher hydrogen crossover rates near the inlet than the outlet is observed regardless of the nitrogen flow rates examined in this study. Thus it is thought that the observed local hydrogen crossover behavior appears general under the specific conditions used in this study.

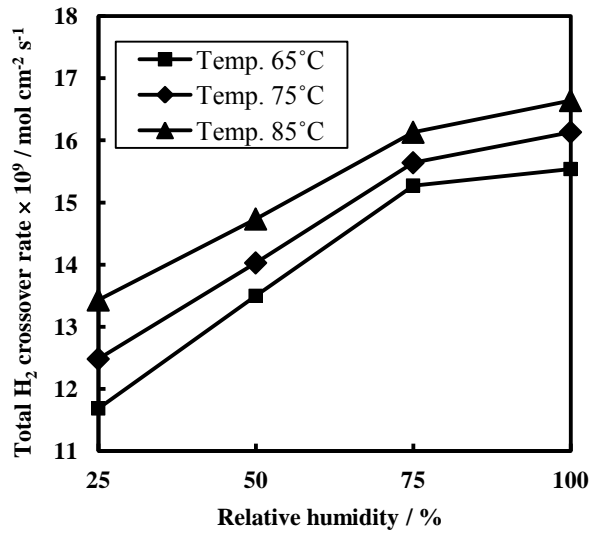
### **3.3.3 Effects of operating conditions on hydrogen crossover**

Fig. 3.12 shows the total hydrogen crossover rates of the single fuel cell under a variety of temperature and RH conditions. As shown in Fig. 3.12(a), the total hydrogen crossover rates of the single cell increase proportionally with the increase of the cell temperature under given RH conditions. Baik et al. [28] reported that the diffusion coefficient increases when temperature is elevated because molecular movement of the gas becomes more active with increase of temperature. They showed that the gas permeability coefficient is expressed as the product of the diffusion coefficient and the solubility coefficient; thus, the increase in diffusion coefficient ultimately results in the

increase in gas permeability coefficient. For this reason, the hydrogen crossover rate increases as temperature increases. As shown in the Fig. 3.12(b), the total hydrogen crossover rates of the single cell increase with increasing RH under given cell temperatures. Several studies investigated why gas crossover occurs largely in a hydrated membrane. Liu et al. [36] reported that when water is absorbed into the membranes, the intermolecular distance between the polymer chains increases to enlarge the free volume, which offers additional passageways where hydrogen crossover can occur. Sakai et al. [4] also investigated that the diffusion coefficient value in hydrated Nafion<sup>®</sup> was 20 times greater than that in dry Nafion<sup>®</sup>, thus increasing hydrogen crossover. Fig. 3.12(b) also shows that the increase of the hydrogen crossover rate from 50% to 75% RH is large, but the increase of the hydrogen crossover rate from 75% to 100% RH is relatively small. This can be explained by the characteristics of membrane hydration. Liu et al. [36] showed the permeability coefficients of CO<sub>2</sub> and N<sub>2</sub> as a function of water content in the membrane. They claimed that a permeability coefficient increases with an increase in water content and tends to level off when the water content is sufficiently high. Thus, a membrane is considered to be fully hydrated above a certain level of RH. The water content of the membrane does not change significantly even if the RH increases further above a critical level, but this critical level depends

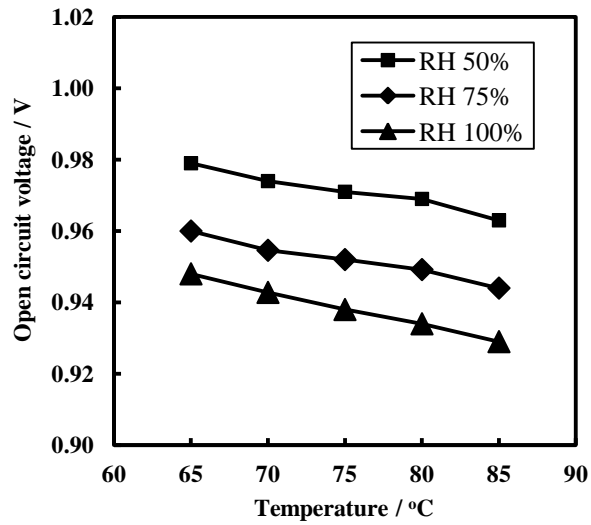


(a)

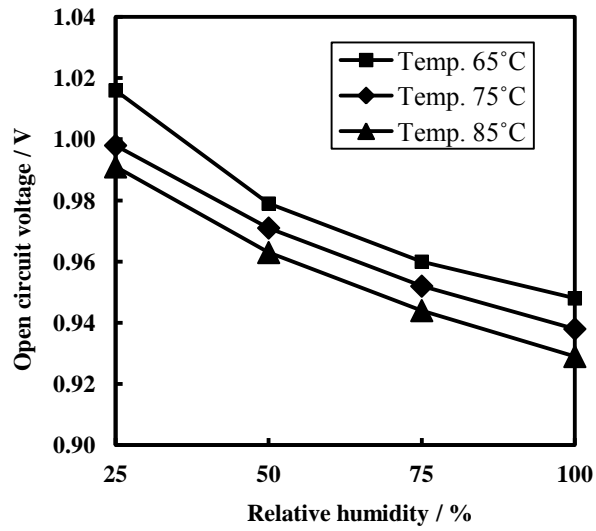


(b)

**Fig. 3.15** Total hydrogen crossover rates of the single fuel cell as a function of (a) cell temperature or (b) RH



(a)



(b)

**Fig. 3.16** Open circuit voltages of the single fuel cell as a function of (a) cell temperature or (b) RH

on the experimental materials and system configurations. In the present study, it is believed that the membrane is likely to be sufficiently hydrated at 75% RH. This is why the hydrogen crossover rates appear to increase only slightly with the increase of RH from 75% to 100%, as shown in Fig. 3.12(b).

Hydrogen crossover from the anode to cathode can decrease the open circuit voltage (OCV) of fuel cells. Several studies [7, 29, 40] have identified the relationship between hydrogen crossover and OCV. They showed that the increase in hydrogen crossover results in the decrease in OCV. Fig. 3.13 shows the OCVs of the single fuel cell under a variety of temperature and RH conditions. As shown in the Fig. 3.13(a), the OCVs of the fuel cell decrease linearly as the cell temperature increases. The results are in good agreement with the total hydrogen crossover rates in Fig. 3.12(a). Consequently, an increase in hydrogen crossover results in a decrease in OCV as cell temperature increases. Likewise, the OCVs of the fuel cell decrease as RH increases, as shown in Fig. 3.13(b), and this result is also consistent with the results of Fig. 3.12(b).

### **3.4 Summary**

In this chapter, we investigated the effect of temperature, RH, hydrogen

pressure, and membrane thickness on hydrogen crossover rate in a PEMFC. The results show that the hydrogen crossover rate increases proportional to the increase in temperature for all membrane samples. As the temperature increases, the reacting gas shows greater molecular movement, resulting in higher rate of hydrogen crossover. Higher hydrogen crossover rates are also observed at higher RH conditions for all membrane samples. Increased water content of the membrane results in greater intermolecular distance between the polymer chains to enlarge the free volume, which offers additional transport pathways. The hydrogen partial pressure increases as hydrogen pressure increases, resulting in increased hydrogen crossover rate. It is found that the change in hydrogen crossover rate is significant for the thinner membranes (NRM-1 and NRM-2), whereas the hydrogen crossover rates are relatively unchanged for the thicker membranes (NRM-3, NRM-4 and NRM-5). All parameters on hydrogen crossover rate, including temperature, relative humidity, hydrogen pressure, and the inverse of the logarithmic membrane thickness, were compared through MLR. MLR analysis of the four independent parameters showed that the hydrogen crossover rate increases with the increase in the following variables: inverse of logarithmic membrane thickness > hydrogen pressure > RH > and temperature.

Local measurements of the hydrogen crossover rate were also conducted

using a single fuel cell with the specially-designed cathode bipolar plate, which has six sampling ports. Firstly, the local distribution of the hydrogen crossover rate from the gas inlet to the outlet of cathode was examined. The hydrogen crossover rate near the inlet was large. The hydrogen gas pressure near the inlet was higher than that near the outlet. Thus, it was believed that the partial pressure gradient of hydrogen was one of the reasons for the local variation of hydrogen crossover in the fuel cell. The hydrogen crossover rates increase with decreasing the nitrogen flow rates at a given section, but the tendency of higher hydrogen crossover rates near the inlet than the outlet was observed regardless of the nitrogen flow rates examined in this study. The effects of operating conditions on the hydrogen crossover rate were also investigated. The hydrogen crossover rate increased with the increase in both temperature and RH of the fuel cell. Furthermore, the effects of temperature and RH on OCV were also examined and compared with the results of the hydrogen crossover rate. The results showed the decrease of the OCV with increase in both cell temperature and RH conditions, which is closely related with the increase in hydrogen crossover.

# **Chapter 4. Measurement of the oxygen crossover rate**

## **4.1 Introduction**

Oxygen crossover causes several problems relating to limiting the durability of PEMFCs. Oxygen crossover influenced to the electrochemical corrosion of carbon in cathode gas diffusion layer (GDL). It is well known that the air/fuel boundary is created at the anode side if oxygen gas transported from cathode side. This increases the potential of cathode higher than the open circuit voltage and quickly corrodes the carbon layer. Another problem caused by oxygen crossover is membrane degradation. Oxygen crossover does provide a means for the formation of peroxide and hydroperoxide radicals, which can slowly deteriorate the membrane. Thus, it is important to measure the oxygen crossover rate through the membrane in a PEMFC. In this study, the quantitative measurements of oxygen crossover that reacts with hydrogen have been conducted by using a mass spectrometer (MS) system. The effects of temperature and relative humidity on oxygen crossover are investigated. The amount of oxygen that reacts with the hydrogen is compared with the conventional oxygen crossover rate. These

oxygen crossover measurements were used to determine how fast membrane degradation occurs. It is also suggested a relative oxygen crossover factor that is a correlation constant between the conventional oxygen permeability coefficients and oxygen permeability coefficients obtained by our study.

## **4.2 New test procedure and method**

In the actual operation of PEMFCs, the amount of oxygen that reacts with hydrogen is very important because it affects the membrane degradation and/or water management at anode side. Oxygen permeated from the cathode side can be divided into two parts under the fuel cell operating conditions as shown in Fig. 4.1. Firstly, some oxygen reacts with hydrogen at the anode catalyst layer. However, not all of the oxygen permeated from the cathode reacts with hydrogen at anode, which means there is residual oxygen detected at the anode outlet [9]. Some reports mentioned that there is no residual oxygen at anode exit stream because all the oxygen reacted with the hydrogen at the anode catalyst layer [31]. However, we repeatedly checked that there is a small amount of residual oxygen at anode side, indicating that not all oxygen that permeated from the cathode side reacts with hydrogen at the anode side.

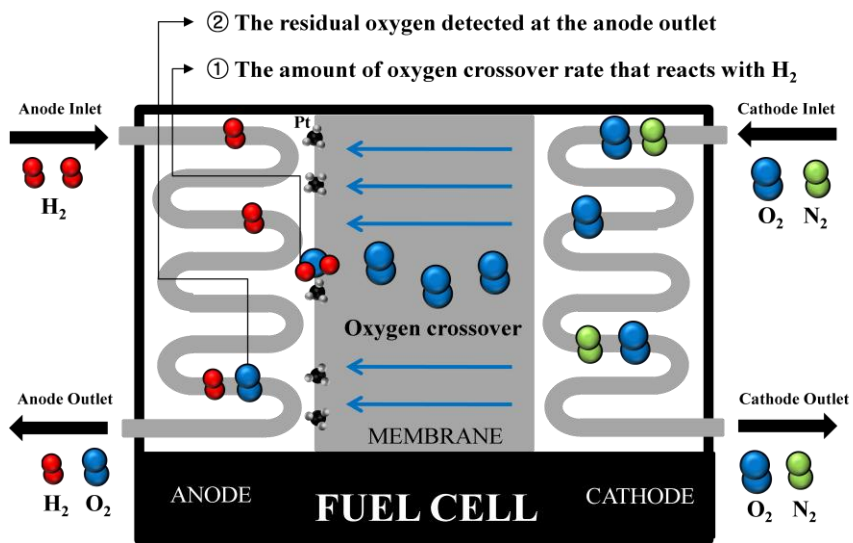


**Fig. 4.1** Schematic diagram of the oxygen crossover rate in a PEMFC

In order to distinguish the amount of oxygen that reacts with the hydrogen at the anode catalyst layer from the whole amount of oxygen crossover rate, two different experiments were conducted using different supplying gases. First, hydrogen for the anode side and oxygen for the cathode side were supplied at  $0.5 \text{ L min}^{-1}$  (LPM), respectively. Some studies [31] reported that oxygen gases were not detected at the anode exit stream under the fuel cell operation conditions because of the reacting with the hydrogen, but the fact that there was a small amount of oxygen gas at the anode exit stream even though the hydrogen was supplied into the anode side was checked by our numerous repeated experiments. The result of oxygen crossover using hydrogen/oxygen was represented in Fig. 4.2. Secondly, helium and oxygen were injected into the anode and cathode sides, respectively, at a flow rate of  $0.5 \text{ L min}^{-1}$ . When helium was supplied at the anode side, the oxygen that permeated from the cathode side does not react with any gas in the anode catalyst layer, thus all cross-overed oxygen exhausted at the helium outlet stream of anode side as shown in Fig. 4.2. Lastly, oxygen that reacts with the hydrogen can be obtained by subtracting the oxygen crossover rate using hydrogen/oxygen supplying gases from that using helium/oxygen supplying gases.

In this paper, the output value of the mass spectrometer was the oxygen

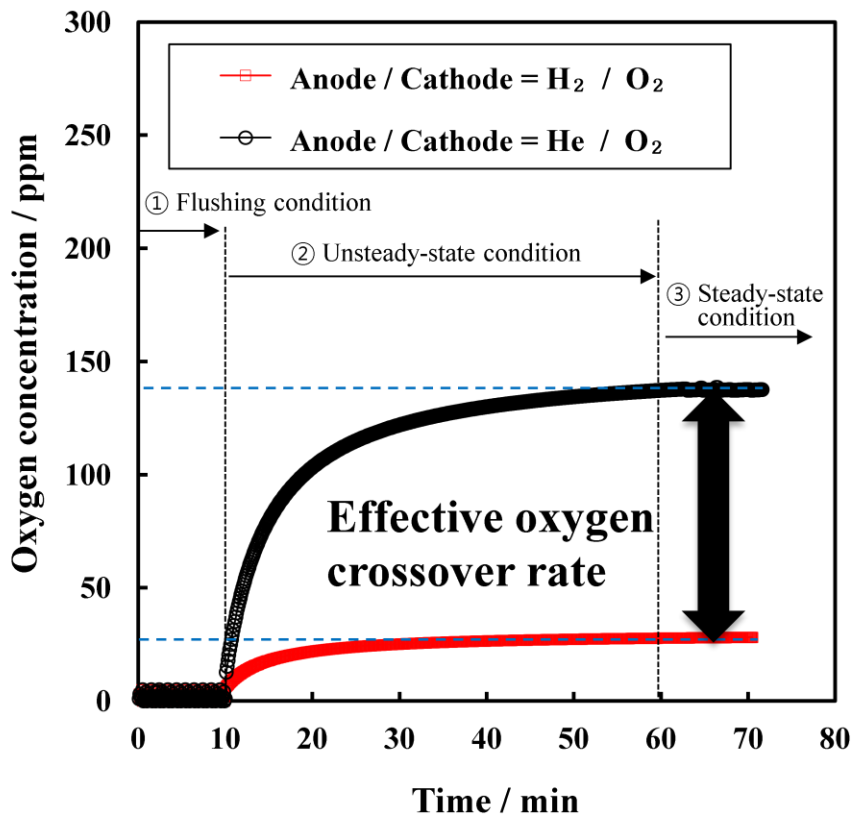


**Fig. 4.2** Experimental raw data of oxygen crossover rates using hydrogen/ oxygen and helium/oxygen supplying gases

concentration in the anode exit stream as shown in Figs. 4.2~4.4. It was assumed that there was no change in hydrogen flow rate at the anode side between the inlet and outlet because the amount of hydrogen that permeated from the anode to cathode during the measurements was expected to be too small to cause a significant drop. Under that assumption, the oxygen concentrations with units of ppm were converted into the flux of oxygen crossover rates,  $J_{O_2}$ , with units of  $\text{mol cm}^{-2} \text{s}^{-1}$  to calculate the oxygen permeability coefficient [28].

### **4.3 Gas selectivity measurement**

The effect of gases that have a different molecular weight such as hydrogen, helium and nitrogen on oxygen crossover could be different, so the gas selectivity tests were conducted to identify the effect of gas selection. For configuration of the gas selectivity, the non-reactive gases such as helium, nitrogen and argon were used as supplying gases at the anode side while oxygen was supplied at the cathode side. Hydrogen was not used in this test because hydrogen can react with oxygen at the anode catalyst layer when oxygen permeated from the cathode to anode sides, affecting the measurement of oxygen crossover rate as shown in Fig. 4.1. The test results

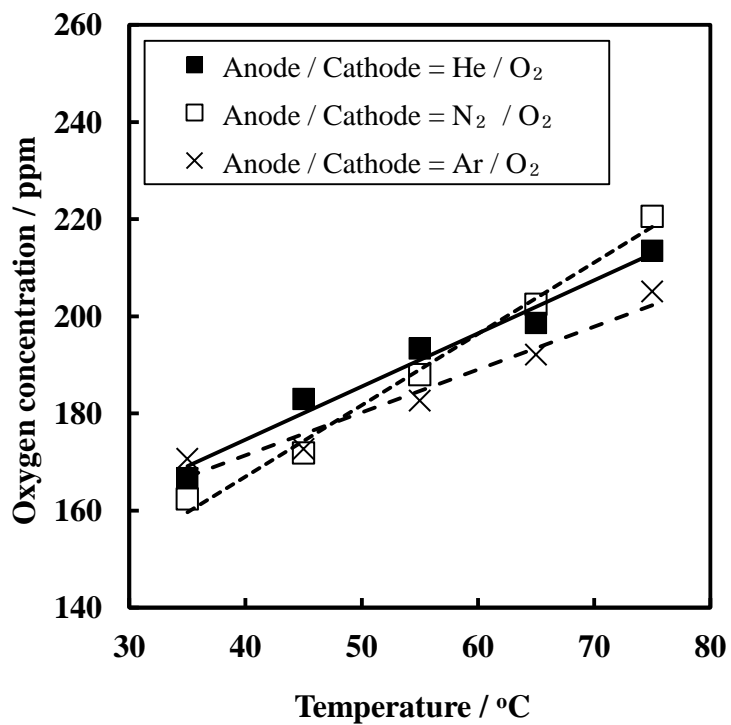


**Fig. 4.3** Oxygen concentration for different supplying gases under various temperature conditions

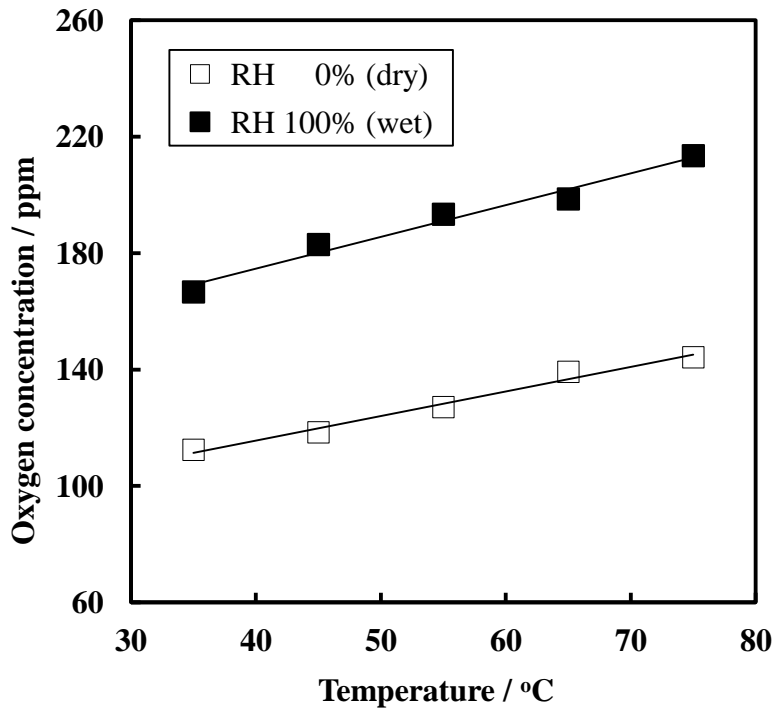
of the gas selectivity were shown in Fig. 4.3. It is observed that the oxygen concentration showed no trend with the molecular weight, implying that the effect of gases that have different molecular weights on oxygen crossover can be negligible under the test conditions used in this study. This is because the fresh membrane was used in this study even though the activation process was conducted prior to the tests. A fresh polymer membrane normally contains large pores enough to allow convective flow. If the size of the pores is larger than the mean free path of the gas molecules, all gases can diffuse through the pores without regard to the molecular weight. This permeation behavior is called “solution-diffusion transport” [53]. However, as the membrane degraded, the permeation behavior may change to Knudsen flow from the solution-diffusion transport. If the size of the pores is smaller than the mean free path of the gas molecules, these pores allow lighter molecules to preferentially diffuse through the pores. This permeation behavior is called “Knudsen flow” [39]. If the membrane exhibits Knudsen behavior, the gas permeability starts to depending on the molecular weight [23, 39, 53]. Thus, the fact that there is no trend with the molecular weight in Fig. 4.3 was acceptable because of using the fresh membrane in this study. This result gives a confidence to use the helium gas as a supplying gas at the anode side in section 4.5 to compare the results of supplying hydrogen at the

anode side.

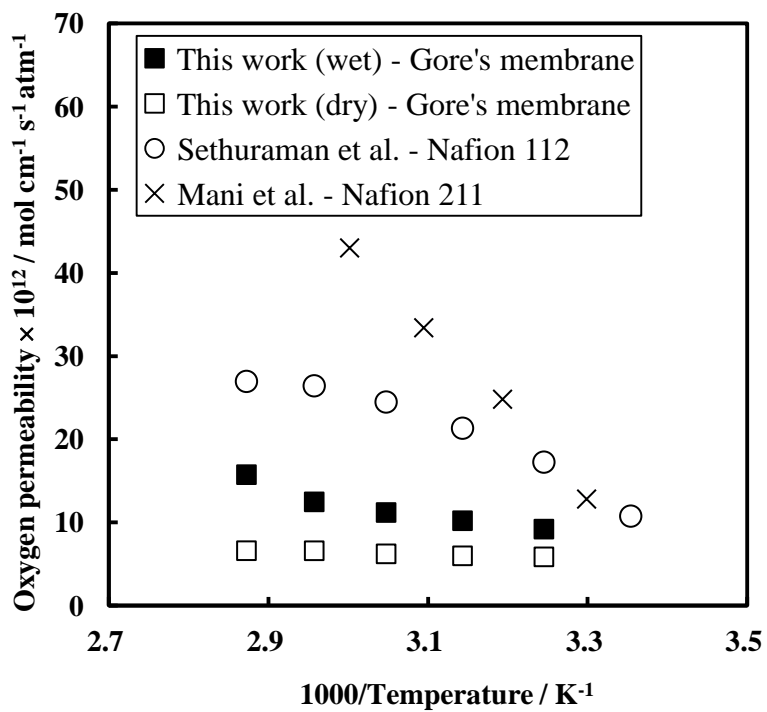
#### 4.4 Quantitative measurements of oxygen crossover

Fig. 4.4 shows the oxygen concentration over a range of fuel cell temperatures at ambient pressure. The results show that oxygen concentration increases with increases in cell temperature under all RH conditions. Higher values of oxygen concentration under the wet conditions are also observed. This is due to the increased oxygen diffusion coefficient. It is generally known that the diffusion coefficient increases when temperature is elevated because molecular movement of the gas becomes more active as temperature increases [28]. Furthermore, it was explained according to the increase in membrane flexibility when the temperature and humidity were increased. Hence, the increase in flexibility of the membrane is a reason for the increase in crossover with increasing cell temperature and humidity [6, 8]. Based on the data in Fig. 4.4, oxygen permeability coefficients are calculated using Eq. (4.1) which is derived from the Fick's law and plotted in Fig. 4.5 [28].

$$k_{O_2} = D_{O_2} \cdot S_{O_2} = J^{C \rightarrow A}_{O_2} \cdot \left( \frac{l}{P^C_{O_2}} \right) \quad (4.1)$$



**Fig. 4.4** The oxygen concentration over a range of fuel cell temperatures at ambient pressure



**Fig. 4.5** Arrhenius plot of oxygen permeability as a function of temperature

The results correspond to an Arrhenius type behavior depending on temperature which is expressed as [54]

$$k_{O_2} = k_{O_2}^0 \cdot \exp\left[-\frac{E_{O_2}}{RT}\right] \quad (4.2)$$

where  $k_{O_2}^0$  is the maximum permeability coefficient of oxygen and  $E_{O_2}$  is the activation energy of oxygen for diffusion. The activation energies for wet and dry gases are 11.32 and 3.00 kJ mol<sup>-1</sup>, respectively. In Fig. 4.5, the oxygen permeability values calculated here are compared with other reported values. Oxygen permeability coefficient values estimated in this study show similar trends to those estimated by Sethuraman using Nafion<sup>®</sup> 112; by Mani using Nafion<sup>®</sup> 211. However, lower oxygen permeability values estimated in this work are observed than those estimated by other studies. The Gore's membranes used in this study are mechanically reinforced membranes. The reinforcement membrane usually provides high mechanical properties [55]. Thus, the permeabilities of the Gore's membranes are much lower than the unreinforced Nafion<sup>®</sup> membranes due to the mechanical improvement of the reinforced membranes.

## 4.5 Measurement of effective oxygen permeability

The data of oxygen crossover using hydrogen/oxygen and helium/oxygen were used to calculate the effective oxygen permeability in this section. It was known in section 4.1 that the molecular weight of supplying gas at the anode side does not affect oxygen crossover because the permeation behavior is the solution-diffusion transport under the fresh membrane conditions. Thus, the data of oxygen crossover using hydrogen/oxygen could be compared to those using helium/oxygen. Fig. 4.6 shows the oxygen concentration at the anode side when hydrogen and oxygen supplied at the anode and cathode sides, respectively. It is shown that the amount of oxygen crossover was low compared with the result in Fig. 4.4 (using helium/oxygen). Due to the reaction with hydrogen as described in Fig. 4.1, the low values of oxygen concentration were detected in the anode exit stream. As shown in Fig. 4.6, the high standard deviation of oxygen concentration is observed because the reaction between the hydrogen and permeated oxygen at the anode catalyst layer is passive. This means it is hard to control the reaction rate to be uniform, leading to the high deviation of oxygen concentration. Thus, duplicate tests must be conducted to obtain reliable results so each type of experiments was repeated five times and the error bars that representing the standard deviation of the results were added

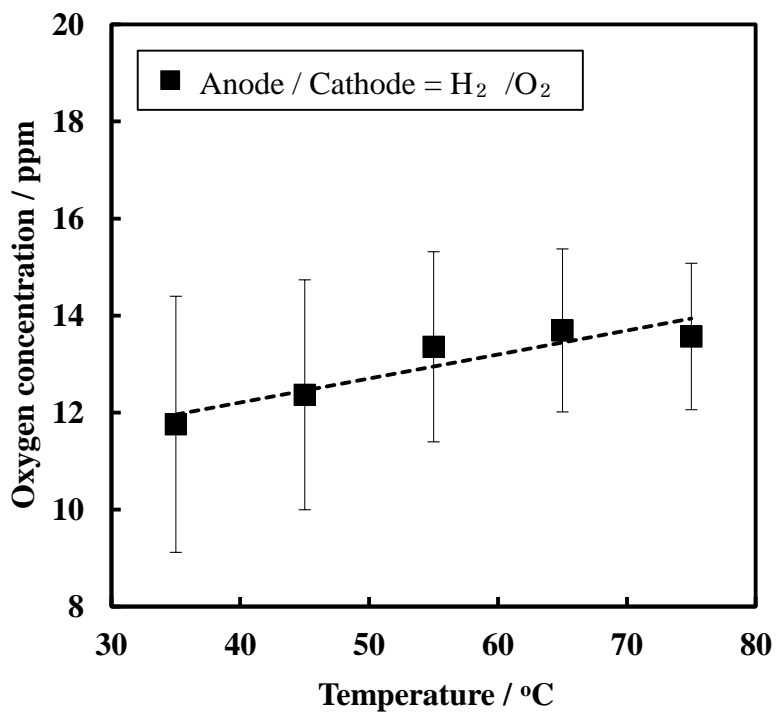


**Fig. 4.6** Oxygen concentration in the anode exit stream using hydrogen and oxygen supplying gases

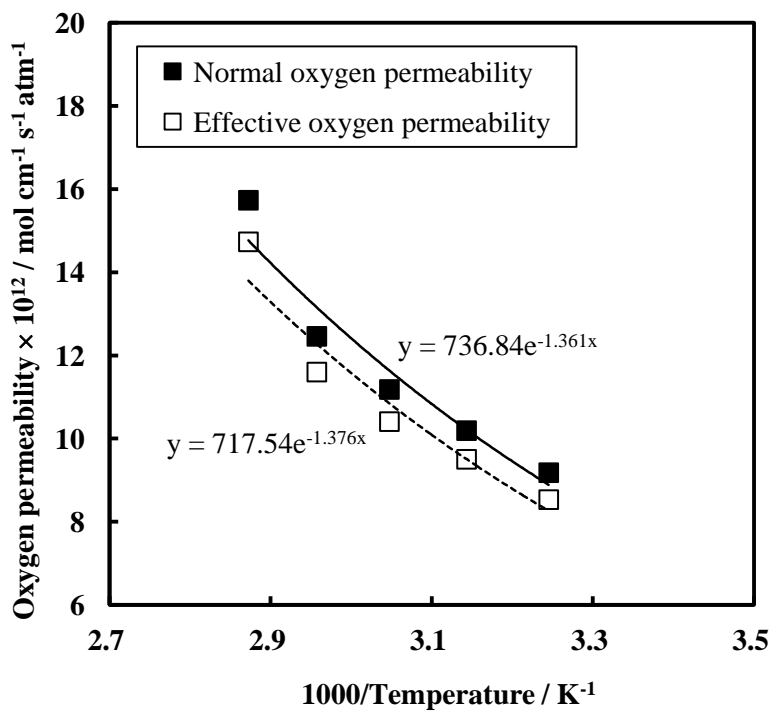
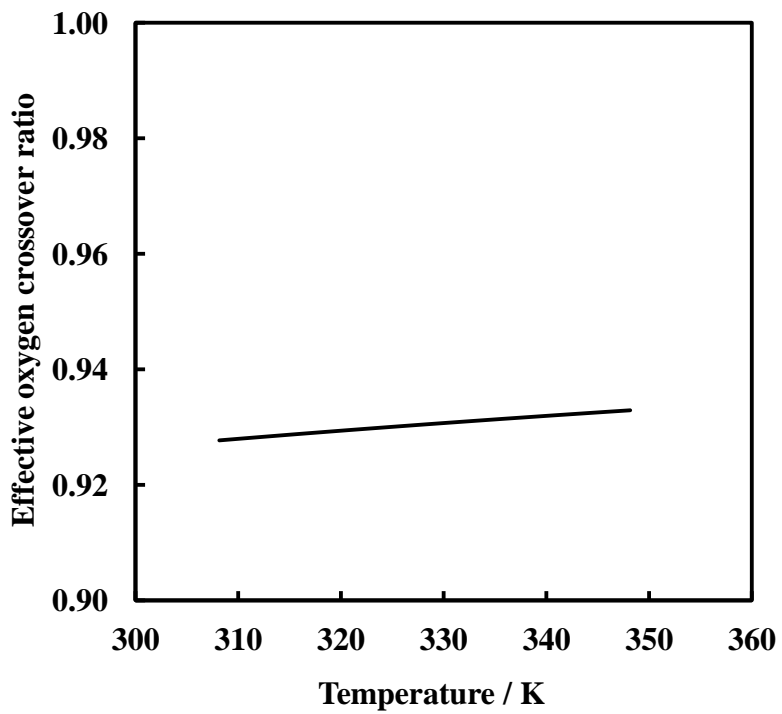


Fig. 4.7 Arrhenius plots of normal and effective oxygen permeabilities



**Fig. 4.8** The effective oxygen crossover ratio under the various temperature conditions

in Fig. 4.6. If we follow the trend of the average value of the test data, the gradual increase in the oxygen concentration is observed as the temperature increases.

From these results, the effective oxygen permeability was calculated by subtracting the value of oxygen concentration using hydrogen/oxygen from that using helium/oxygen as described in Fig. 4.2. The effective oxygen permeability was shown in Fig. 4.7 and compared to the normal oxygen permeability. The effective oxygen permeability also follows to an Arrhenius type behavior. The fitting equations of normal and effective oxygen permeabilities were also represented in Fig. 4.7. The normal oxygen permeability represents the whole amount of oxygen crossover from the cathode to anode sides, but it could not explain the exact amount of oxygen crossover that affect the membrane degradation and/or water generation under the fuel cell operating conditions. Thus, the effective oxygen permeability should be considered as an index of the membrane degradation and/or water generation due to oxygen crossover. To simply suggest the effective oxygen permeability, the effective oxygen crossover ratio,  $\alpha(T)$ , which is the ratio between the normal and effective oxygen permeability was calculated using Eq. (4.3). As shown in Fig. 4.8, the effective oxygen crossover ratio decreases as temperature increases and those are in a range

between 0.927 ~ 0.933 under the fuel cell operating temperature conditions.

$$\alpha(T) = \frac{\text{Effective oxygen permeability}}{\text{Normal oxygen permeability}} = 0.974 \cdot \exp\left(-\frac{15}{T}\right) \quad (4.3)$$

## 4.6 Summary

The quantitative measurements of oxygen crossover that reacts with hydrogen have been conducted by using a MS system. To identify the effect of gases that have a different molecular weight on oxygen crossover, the gas selectivity tests were conducted. Result showed that the oxygen concentration showed no trend with the molecular weight, implying that the effect of gases that have different molecular weights on oxygen crossover can be negligible. Thus, the data of oxygen crossover using hydrogen/oxygen and helium/oxygen were used together to calculate the effective oxygen permeability. The effective oxygen permeability could explain the exact amount of oxygen crossover that affect the membrane degradation and/or water generation under the fuel cell operating conditions. Thus, the effective oxygen permeability should be considered as an index of the membrane degradation and/or water generation due to oxygen crossover. The ratio between the normal and effective oxygen permeability is in a range between 0.927 ~ 0.933 under the fuel cell temperature conditions.

# **Chapter 5. Measurement of the nitrogen crossover rate**

## **5.1 Introduction**

When fuel cell operated, nitrogen is permeated from the cathode to anode sides due to the gas crossover. Cross-overed nitrogen accumulates in the fuel cell's hydrogen recirculation system. The excessive buildup of nitrogen lowers the hydrogen concentration, affecting fuel cell performance so it is needed to measure the nitrogen crossover rate in a PEMFC. In this chapter, experimental measurements of nitrogen crossover were obtained using a mass spectrometer and nitrogen permeability coefficients were estimated. The effects of fuel cell temperature and relative humidity on nitrogen crossover were also investigated.

## **5.2 Characterization of nitrogen crossover under open circuit voltage conditions**

For measurement of nitrogen crossover under open circuit voltage (OCV) conditions, hydrogen and nitrogen were supplied at  $0.9 \text{ L min}^{-1}$  and

2.0 L min<sup>-1</sup>, respectively, for more than 30 min. Nitrogen concentration in the anode exit stream was measured using the quadrupole mass spectrometer under various fuel cell temperature and relative humidity (RH) conditions in order to obtain data for nitrogen crossover and nitrogen permeability coefficient (NPC) calculation.

### **5.2.1 Effect of operating condition on nitrogen crossover**

Fig. 5.1 shows the nitrogen concentration in the anode exit stream over a range of fuel cell temperatures at ambient pressure and with the fuel cell in a steady state. The results show that nitrogen concentration increases with increases in cell temperature under all RH conditions tested, and that higher nitrogen concentrations are observed under higher RH conditions. This is because the nitrogen diffusion coefficient increases while the solubility of nitrogen decreases. It is generally known that the diffusion coefficient increases when temperature is elevated because molecular movement of the gas becomes more active as temperature increases. However, solubility decreases with increased temperature. Such behavior is a result of exothermic enthalpy of the solution. When a gas continues to dissolve in a membrane, the solution continues to release energy. Consequently, because

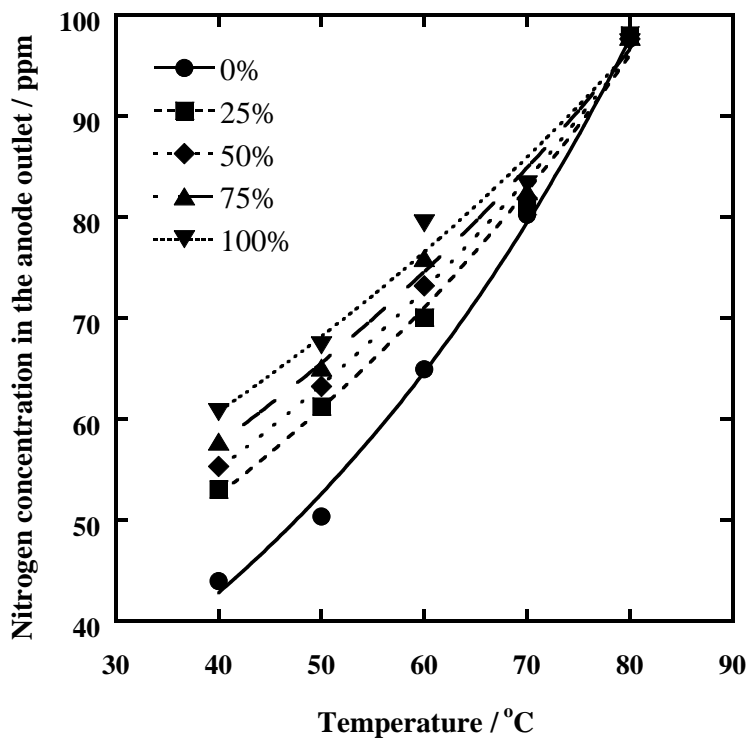


**Fig. 5.1** Nitrogen concentration in the anode exit stream under various cell temperature at ambient pressure

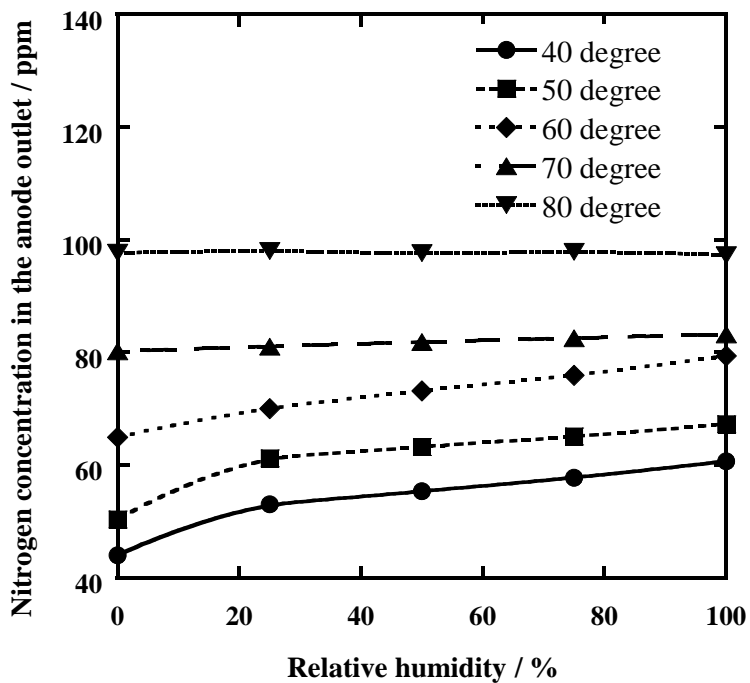


**Fig. 5.2** Raw data of nitrogen concentration at anode exit stream under various relative humidity at ambient pressure

dissolution of gases is an exothermic process, heating decreases the solubility of a gas. Cheng et al. [6] measured the hydrogen crossover rate in high-temperature PEMFC and their results show the same trend as our results, *i.e.* the hydrogen crossover rate increases with increasing temperature.

The effects of RH in the supply gas were investigated and the results are presented in Fig. 5.2. Under lower cell temperature conditions (40~60°C), nitrogen concentration slightly increased as RH increased. However, nitrogen concentration did not change with changes in RH under the higher cell temperature conditions (70~80°C). This inconsistency is because a change in RH changes the water content in the membrane, which in turn affects the membrane's permeability coefficient; however, the nitrogen concentration at the cathode side is reduced due to an increase in the saturation vapor pressure. As shown in Eq. (5.1), the  $P_{N_2}^C$  reduces due to an increase in the magnitude of  $P_{H_2O}^C$  with an increase in RH.

$$P_{total}^C = P_{N_2}^C + P_{H_2O}^C \quad (5.1)$$

## 5.2.2 Nitrogen permeability coefficient

Based on the results of section 5.2.1, nitrogen permeability coefficient

(NPC) is calculated. The NPC estimates for various cell temperatures and RH conditions are shown in Fig. 5.3. The results show that NPC follows an Arrhenius type of temperature behavior which can be written as [54]

$$k_{N_2} = k_{N_2}^0 \cdot \exp\left[-\frac{E_{N_2}}{RT}\right] \quad (5.2)$$

where  $k_{N_2}^0$  is the maximum permeability coefficient of nitrogen and  $E_{N_2}$  is the activation energy of nitrogen for diffusion. These values were calculated for each RH and the results are shown in Table 5.1. When the membrane is fully hydrated (*i.e.*, RH=100%), the maximum permeability coefficient and activation energy of nitrogen are  $5.14 \times 10^{-13} \text{ mol m}^{-1} \text{ s}^{-1} \text{ Pa}^{-1}$  and  $19.83 \text{ kJ mol}^{-1}$ , respectively. This  $E_{N_2}$  value is close to the previous reported value of  $24.0 \text{ kJ mol}^{-1}$  reported for a Nafion® 117 membrane [22]. This suggests that membrane thickness does not largely affect the gas permeability coefficient. Cheng et al. [6] and Mittelsteadt et al. [56-57] similarly suggested that membrane equivalent weight and membrane thickness have little effect on gas permeability, but membrane water uptake did influence gas permeability.

Fig. 5.4 shows NPC as a function of RH at ambient pressure. As shown in the figure, higher NPC values are observed when the membrane is more hydrated at higher cell temperatures. The increase in the water content of the membrane at higher cell temperatures can affect both solubility and

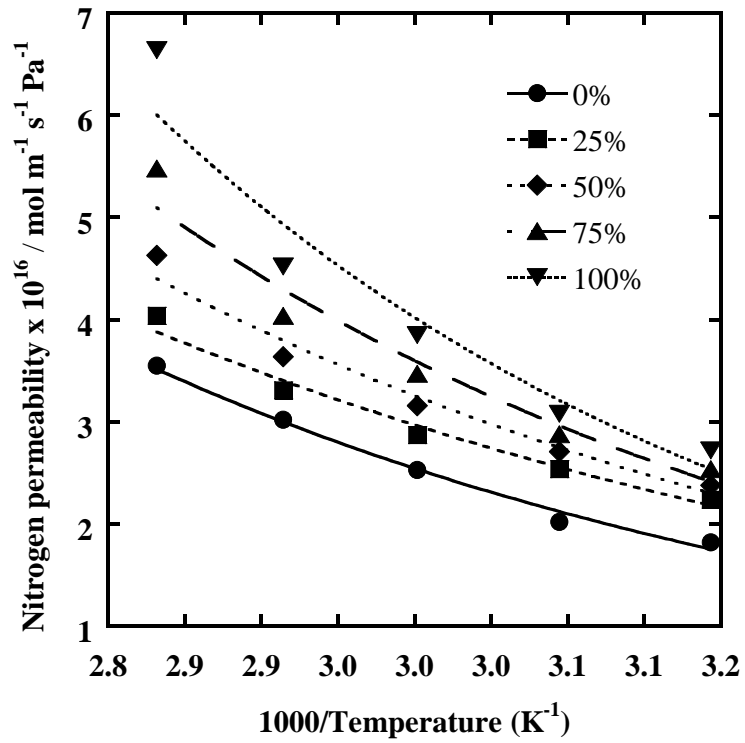


**Fig. 5.3** Arrhenius plot of nitrogen permeability coefficient as a function of fuel cell temperature

**Table 5.1** Calculated maximum permeability coefficient and the activation energy from the Arrhenius plot as a function of RH

| <b>RH (%)</b> | <b>Maximum permeability coefficient, <math>k_{N_2}^0</math><br/>(<math>\text{mol m}^{-1} \text{s}^{-1} \text{Pa}^{-1}</math>)</b> | <b>Activation energy, <math>E_{N_2}</math><br/>(<math>\text{kJ mol}^{-1}</math>)</b> |
|---------------|---|--|
| 0             | $7.92 \times 10^{-14}$  | 15.91  |
| 25            | $3.47 \times 10^{-14}$  | 13.19  |
| 50            | $7.01 \times 10^{-14}$  | 14.89  |
| 75            | $1.77 \times 10^{-13}$  | 17.17  |
| 100           | $5.14 \times 10^{-13}$  | 19.83  |

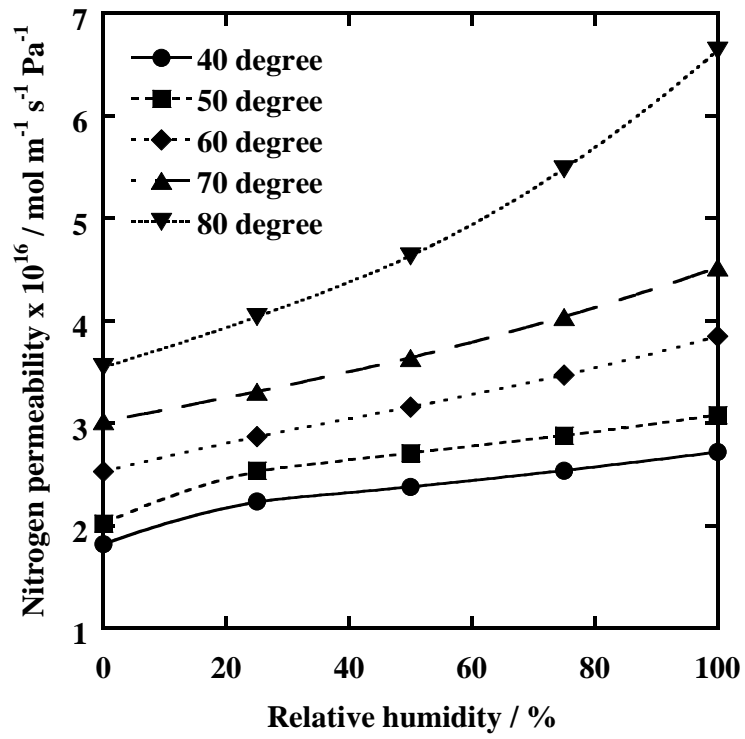


**Fig. 5.4** Nitrogen permeability coefficient as a function of RH at ambient pressure

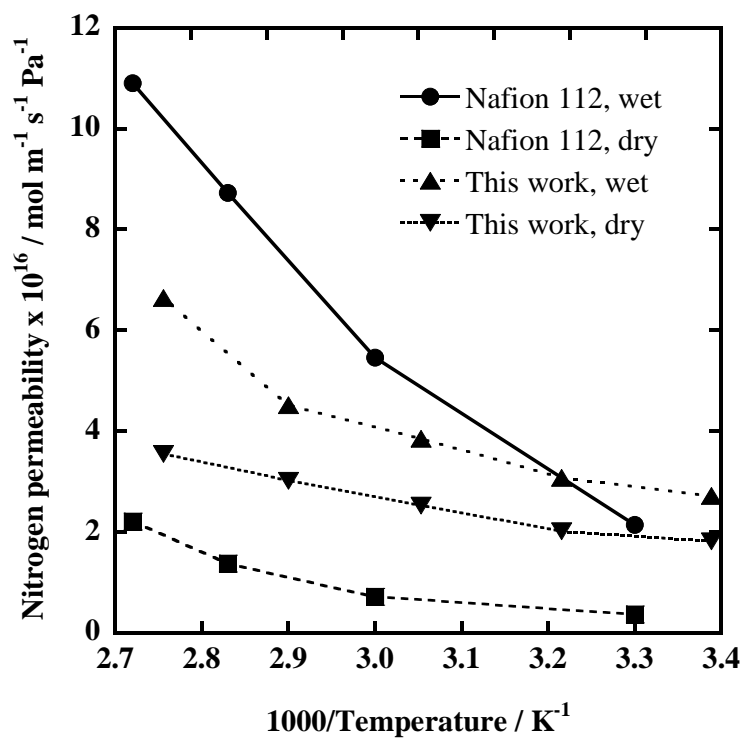


**Fig. 5.5** Comparison of nitrogen gas permeability coefficient with reported data

diffusivity, resulting in an increase in the membrane's permeability coefficient. Sakai et al. [3-4] reported that the diffusion coefficient value in hydrated Nafion<sup>®</sup> was 20 times greater than that in dry Nafion<sup>®</sup>. However, the solubility coefficient in hydrated Nafion<sup>®</sup> was half that in dry Nafion<sup>®</sup>. Thus, solubility decreases slightly and diffusivity increases remarkably (both influenced strongly by the contained water) when Nafion<sup>®</sup> is hydrated. This indicates that NPC increases at higher cell temperatures are due to an increase in diffusion coefficients as RH increases.

The NPC values calculated here may be compared with other reported values by viewing the results in Fig. 5.5. Mittelsteadt et al. [56] estimated NPC over a wide temperature range (30~95°C) and RH (0~100%) with wet and dry Nafion<sup>®</sup> 112. As shown in the figure, higher NPC values are obtained when the membrane is exposed to wet conditions than when the membrane is dry.

### **5.3 Characterization of nitrogen crossover under power generation conditions**

To identify nitrogen crossover during power generation, hydrogen and air were supplied to the anode and cathode sides, respectively. The nitrogen

concentration in the anode exit stream was then measured when the PEMFC was operated under various power generation conditions.

### 5.3.1 Effect of current density on nitrogen crossover

To investigate the effect of current density, hydrogen and air were supplied at a constant flow rate of  $0.9 \text{ L min}^{-1}$  and  $2.0 \text{ L min}^{-1}$ , respectively. Fig. 5.6 shows the effect of current density on nitrogen concentration in the anode exit stream. A linear increase of nitrogen concentration was observed at the  $0.9 \text{ L min}^{-1}$  hydrogen inlet flow rate. For analysis of nitrogen crossover using nitrogen concentration data, the residual hydrogen flow rate at the exit is needed. However, measuring that residual flow rate experimentally is not easy due to the large amount of water vapor in the anode exit stream. Here, the following basic fuel cell formula was used.

$$N_e^A = N_i^A - \frac{I}{2F} \cdot M_{H_2} \cdot \frac{60}{\rho} \quad (5.3)$$

where  $N_e^A$  is the residual anode exit hydrogen flow rate,  $N_i^A$  is the supply anode inlet hydrogen flow rate (*i.e.*,  $N_i^A = 0.9 \text{ L min}^{-1}$ ) and  $\frac{I}{2F} \cdot M_{H_2} \cdot \frac{60}{\rho}$  is the hydrogen consumption rate. Using Eq. (5.3), the residual exit hydrogen flow is calculated separately from the hydrogen consumed during the generation of electrical power as shown in Fig. 5.7. From the

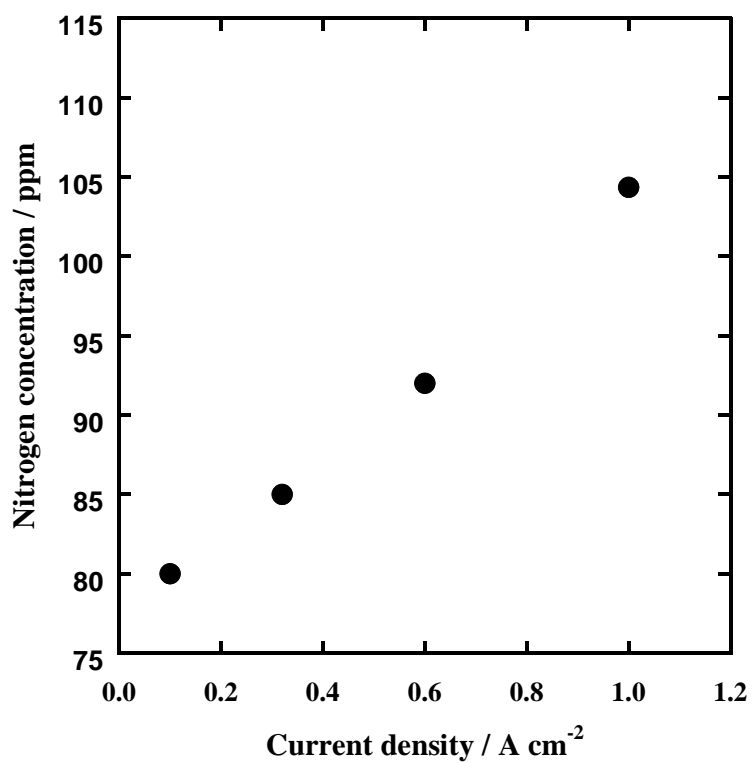


**Fig. 5.6** Nitrogen concentration in the anode exit stream under various current densities when hydrogen flow rate is 0.9 L min<sup>-1</sup> and air flow rate is 2.0 L min<sup>-1</sup>

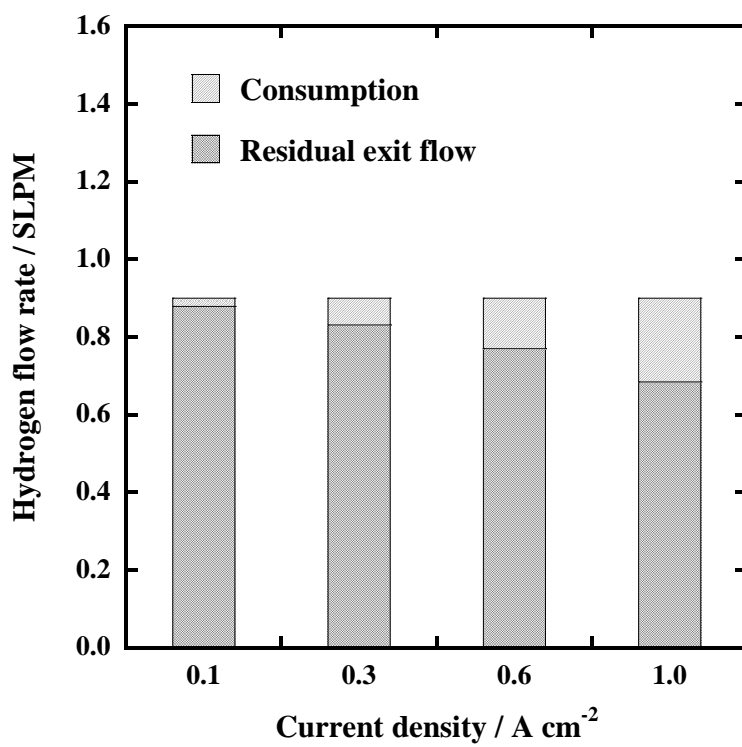


**Fig. 5.7** Calculated hydrogen consumption and the residual hydrogen flow rate at the exit under various current densities

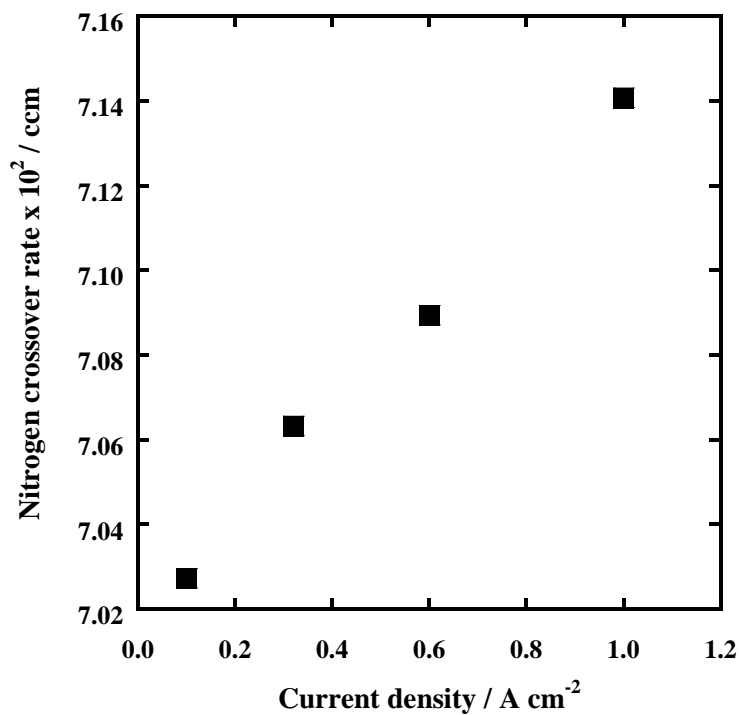


**Fig. 5.8** Nitrogen crossover rate under various current densities when hydrogen flow rate is 0.9 L min<sup>-1</sup> and air flow rate is 2.0 L min<sup>-1</sup>

results shown in Figs. 5.6 and 5.7, the nitrogen crossover rate can be estimated for various current density conditions as shown in Fig. 5.8. Those results show that nitrogen crossover increases with increasing current density. An increase in current density indicates that the fuel cell is generating an increase in power and producing heat. Thus, both fuel cell temperature and membrane water content increase due to the generation of heat and water in the fuel cell. Moreover, nitrogen crossover increases because of increases in membrane temperature and water content.

### **5.3.2 Effect of anode stoichiometric ratio on nitrogen crossover**

Typically, during fuel cell operation, a constant anode stoichiometric ratio ( $SR_A$ ) instead of a constant flow rate is used to expand fuel efficiently over a range of current densities. The  $SR_A$  determines the flow rate of the supplied hydrogen and can markedly affect the nitrogen concentration in the anode stream. Fig. 5.9 shows the nitrogen concentration in the anode exit stream under various  $SR_A$  conditions while the cathode stoichiometric ratio was set at 3.0. The results show that the nitrogen concentration increases under all current densities as the  $SR_A$  decreases. In particular, the results show a particularly marked increase in nitrogen concentration at low current

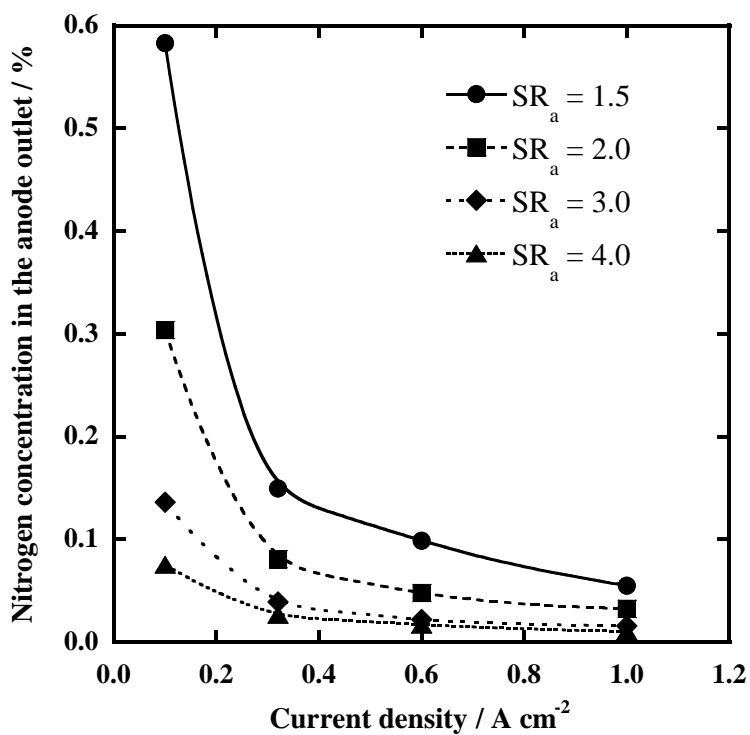


**Fig. 5.9** Nitrogen concentration in the anode exit stream under various anode stoichiometric ratios at ambient pressure with cathode stoichiometric ratio of 3.0

densities. The hydrogen supply flow rate at a low current density is relatively smaller compared to that at a high current density; thus, the residual hydrogen flow rate at the exit under a low current density is also small. Nitrogen concentration in the anode exit stream is largely determined by the residual hydrogen flow rate; therefore, a small residual hydrogen flow rate will result in a high nitrogen concentration. The hydrogen is usually supplied at greater than the  $SR_A$  which means that the rate of hydrogen supply is determined by  $SR_A$ . For example, the hydrogen flow rate increases with an increase in the  $SR_A$  and decreases with a decrease in the  $SR_A$ . A low hydrogen flow at a low current density will significantly increase the nitrogen concentration, due to the small amount of hydrogen flow. This relationship between  $SR_A$  and hydrogen flow rate can produce marked increases in nitrogen concentration at low current densities. This suggests that a higher  $SR_A$  should be used at low current densities, while a lower  $SR_A$  should be used at high current densities.

## **5.4 Summary**

In this chapter, nitrogen crossover was measured using a mass spectrometer under various operating conditions and under OCV and power

generation conditions in single PEMFCs. Under OCV conditions, nitrogen crossover increased with increasing cell temperature under all RH conditions. NPC was calculated based on the obtained nitrogen concentration data and the NPC results fitted the form of Arrhenius expression. When the PEMFC membrane was fully hydrated, the maximum permeability coefficient and activation energy of nitrogen were  $5.14 \times 10^{-13} \text{ mol m}^{-1} \text{ s}^{-1} \text{ Pa}^{-1}$  and  $19.83 \text{ kJ mol}^{-1}$ , respectively. NPC as a function of RH was also investigated. At higher cell temperatures and when the membrane was hydrated, a higher NPC was observed. In addition, the solubility decreased slightly and diffusivity increased remarkably, when the membrane was hydrated, indicating that the permeability coefficient increased. Under power generation conditions, nitrogen crossover increased with increasing current density. Moreover, when current density increased, nitrogen crossover increases were found to be related to elevated membrane temperature and high water content. When the  $SR_A$  was low, nitrogen concentration increased under all current densities tested. At low current densities, a change in the hydrogen flow rate, due to a change in the  $SR_A$  being used, significantly affects the nitrogen concentration. This work may be useful in the development of a nitrogen crossover model that can be used to facilitate establishment of an efficient method for hydrogen recirculation systems.

## **Chapter 6. Gas crossover due to GDL penetration**

### **6.1 Introduction**

During the assembling process of fuel cell stack, the compression or clamping pressure of PEMFCs for vehicle applications is typically high enough to minimize contact resistance among the cell components such as MEA, GDL and bipolar plate. However, a few experimental studies have been done to understand the membrane degradation when compression pressure increased. Mittelsteadt et al. [57] investigated membrane puncturing due to the diffusion media (carbon fiber paper materials) penetration into the membrane under various membrane thickness and relative humidity (RH) cycling conditions. They focused on the relationship between membrane properties and membrane puncturing and also measured the specific resistances to identify membrane puncturing. According to this study, carbon fiber penetration makes several micro-holes in the MEA surface when clamping pressure is too high. Those micro-holes are the cause of the membrane degradation because hydrogen and oxygen can easily penetrate into the membrane through the micro-holes. Thus membrane degradation process is accelerated in these spots. Lai et al. [58] conducted an accelerated

stress test to compare the shorting performance of various material sets using a current distribution measurement technique to monitor the local shorting behavior. Likewise, several experimental researches about the membrane puncturing under various clamping pressures have been conducted. To the best of our knowledge, however, hydrogen crossover due to the membrane puncturing as a function of the clamping pressure has not been reported in literatures. In this study, membrane puncturing due to the carbon fiber penetration into the membrane has been investigated, and hydrogen crossover and open circuit voltage (OCV) for three types of GDLs were measured. The performances of cells with different types of GDLs were also measured under various clamping torque conditions. Lastly, morphological images of the GDLs and the catalyst layer in MEA have been analyzed by scanning electron microscopy (SEM) in connection with hydrogen crossover to elucidate the membrane puncturing process.

## **6.2 Materials and experimental setup**

Three types of commercial GDL were used in this study. The GDLs used in this study are listed in Table 6.1. The GDL-1 has a macro-porous substrate of carbon fiber felt with MPL-1 coating type of a rough surface, the

GDL-2 has a carbon fiber felt substrate with MPL-2 coating type of a smooth surface, and the GDL-3 has a carbon fiber paper substrate with MPL-2. The results of GDL-1 and GDL-2 are compared to investigate the effect of MPL type on the membrane puncturing, and the results of GDL-2 and GDL-3 are compared to explain the effect of carbon fiber structure in macro-porous substrate on the membrane puncturing. The thickness of all the GDLs was measured with at least 20 measurements per each GDL using a Mitutoyo thickness gauge (Mitutoyo Co., Tokyo, Japan) and the values of average and standard deviation were listed in Table 6.1.

In this study, a single cell with an active area of 25 cm<sup>2</sup> was used. The single fuel cell is composed of end plates, graphite bipolar plates with a 5-serpentine channel for both anode and cathode flow fields, GDLs, gaskets and an MEA. A commercial MEA was used for all the experiments. Teflon gaskets were also used to prevent the gas leakage. A torque wrench (CDI Torque Product, USA) was used for a fuel cell assembly. The torque wrench was firstly set at a designated value and the single cell assembly was compressed uniformly with a torque wrench. A leak testing was performed after the fuel cell assembly process. All measured data were transmitted to a computer by a general-purpose interface bus connection. Hydrogen and nitrogen gases were supplied to anode side, and air and nitrogen gases were

**Table 6.1** Characteristics of GDLs used in this study

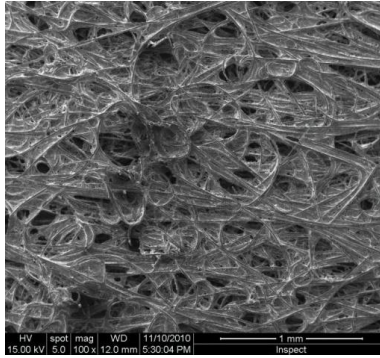
| <b>Code name</b> | <b>Macro-porous substrate type</b> | <b>Micro-porous layer coating type</b> | <b>Thickness (<math>\mu\text{m}</math>)</b> |
|------------------|------------------------------------|--|---|
| GDL-1            | Carbon fiber felt                  | MPL-1 (rough surface)                  | $426 \pm 10$                                |
| GDL-2            | Carbon fiber felt                  | MPL-2 (smooth surface)                 | $423 \pm 5$                                 |
| GDL-3            | Carbon fiber paper                 | MPL-2 (smooth surface)                 | $365 \pm 6$                                 |

supplied to cathode side for the experiments. All gas flow rates were controlled by mass flow controllers which were calibrated before the tests. In order to measure the operating temperature of the fuel cell, T-type thermal couples (TCs) were inserted into the long hole of 40 mm in both the anode and cathode bipolar plates, and heaters were also inserted into both the anode and cathode end plates. Both TCs and heaters were connected to the UT 550 temperature controller (Yokogawa, Tokyo, Japan) to control the fuel cell temperature. For a gas humidification, bubble type humidifiers were used. A mass spectrometer was installed to the cathode exit stream to measure the hydrogen concentration in the nitrogen flow. For electrochemical measurements, a PLZ 1004WA electric load (Kikusui Electronics, Yokohama, Japan) was used for measuring a voltage and current of the fuel cell. Hydrogen crossover through the membrane in a PEMFC was measured using an on-line HPR-20 quadrupole mass spectrometer (Hidden Analytical, Warrington, UK). A flushing sequence is needed to measure the small amount of hydrogen, thus a flush line was installed and combined with conventional fuel cell test system. For quantitative measurements with the mass spectrometer, a calibration process proposed by Bley et al. [34] was conducted using a nitrogen-based standard gas mixture which contained 200 ppm of hydrogen.

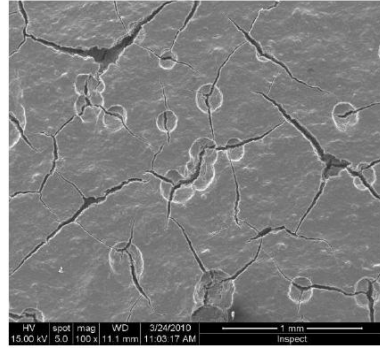
The test procedure is well designed for measuring the OCV and hydrogen crossover. For a preparation of the fuel cell experiment, the fuel cell was assembled and the clamping torque was set at the lowest value. Activation process was conducted for fresh fuel cell under the following conditions: hydrogen and air flow, temperature of 65°C, RH of 100%, and stoichiometric ratios at anode and cathode sides of 1.5 and 2.0, respectively. After the activation process, the fuel cell characterization was performed to measure a current-voltage (*I-V*) polarization curve. Firstly, measurement of *I-V* curve was carried out when RH is 50% with the same operating conditions in the activation process. Following the performance test, hydrogen crossover rate was measured while the hydrogen for anode and nitrogen for cathode were supplied at 0.9 and 0.5 L min<sup>-1</sup>, respectively. Gas crossover through the membrane occurs when the concentration of gas is different between the anode and cathode sides. According to the gas crossover theory, hydrogen can permeate from the anode to cathode sides, and thus cathode exit stream includes a small amount of hydrogen. The cathode exit stream containing a small amount of hydrogen was injected to the mass spectrometer via a 3-way valve to measure the hydrogen crossover. After the hydrogen crossover measurements at 50% RH, measurements of *I-V* curve and hydrogen crossover at 100% RH were also performed. After

finishing the measurement of hydrogen crossover, the fuel cell was cooled down to the ambient temperature for increasing clamping torque and the same experiments were conducted under other clamping torque conditions for the fuel cell with GDL-1. The tests for the fuel cells with GDL-2 and GDL-3 were accomplished in the same manner described above.

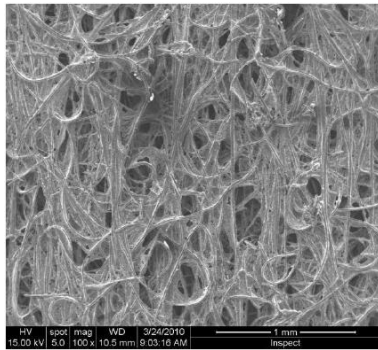
The surface morphology of MPLs and macro-porous substrates of all the pristine GDL samples was observed by SEM (InspectTM, FEI Co.) with an accelerating voltage of 15 kV and a magnification of 100×. The cross-sectional morphology of the GDL-1 and the surface morphology of anode catalyst layer in MEA before and after compression tests were characterized by the field-emission SEM (SUPRA 55VP, Carl Zeiss, Weimar, Germany). Fig. 6.1 shows the surface images of macro-porous substrates and MPLs of GDLs used in this study which were observed by 100× magnification as representative photos. As shown in Fig. 6.1(a) and (c), the GDL-1 and GDL-2 have the same macro-porous substrate structures of carbon fiber felt, while the MPL surfaces of GDL-1 and GDL-2 are rough and relatively smooth as shown in Fig. 6.1(b) and (d), respectively. As shown in Fig. 6.1(c) and (e), the macro-porous substrate structures of GDL-2 and GDL-3 are carbon fiber felt and paper, respectively, while both the GDLs have the same MPL type with relatively smooth surface (see Fig. 6.1(d) and (f)). It is observed that the



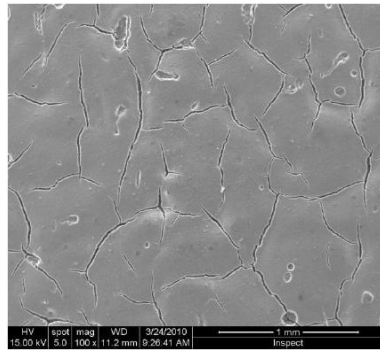
(a)



(b)

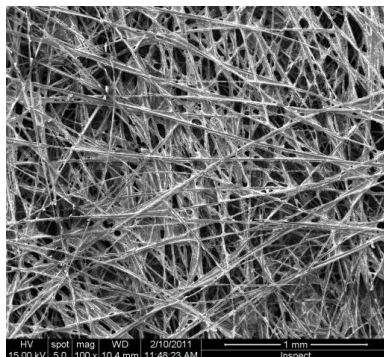


(c)

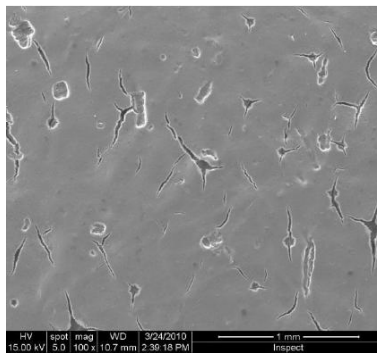


(d)

**Fig. 6.1** Surface morphologies of macro-porous substrate and micro-porous layer observed by SEM with a 100× magnification: (a) macro-porous substrate and (b) micro-porous layer of GDL-1, (c) macro-porous substrate and (d) micro-porous layer of GDL-2, (e) macro-porous substrate and (f) micro-porous layer of GDL-3



(e)



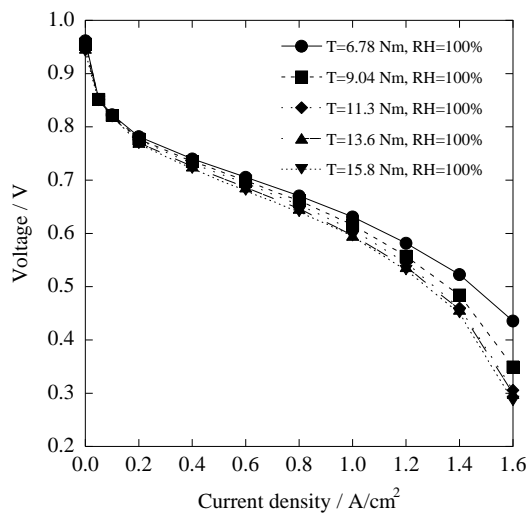
(f)

**Fig. 6.1** Surface morphologies of macro-porous substrate and micro-porous layer observed by SEM with a 100× magnification: (a) macro-porous substrate and (b) micro-porous layer of GDL-1, (c) macro-porous substrate and (d) micro-porous layer of GDL-2, (e) macro-porous substrate and (f) micro-porous layer of GDL-3

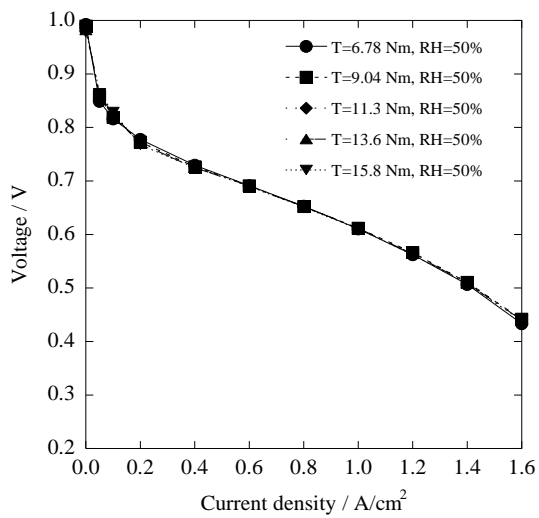
carbon fiber felt is likely to have more entangled structure, while the carbon fiber paper appears to be more straight [59-60].

### **6.3 Electrochemical *I-V* performance of fuel cell**

Fig. 6.2(a) and (b) show the polarization curves of cells with GDL-1 under various clamping torque conditions at 100% and 50% RHs, respectively. In Fig. 6.2(a), the overall performance decreases as clamping torque increases when RH is 100%. In particular, the voltage at a current density of  $1.6 \text{ A cm}^{-2}$  dropped from 0.436 to 0.286 V at clamping torques from 6.78 to 15.8 N m, respectively. It is due to the reduced porosity of GDL when clamping torque increases. Chang et al. [61] reported that high clamping torque narrowed down the diffusion path for mass transport from gas channels to the catalyst layers. Additionally, the amount of generated water as a result of fuel cell reaction is larger at higher current densities, indicating a larger mass transport limitation in GDL regions. Thus the mass transport or concentration loss occurred caused a decrease in the fuel cell performance. However, the voltage drop is not observed when the RH is 50% as shown in Fig. 6.2(b). It is attributed to the fact that the amount of water inside the GDL at 50% RH is relatively lower than that at 100% RH,



(a)



(b)

**Fig. 6.2** The polarization curves under various clamping torque conditions for the GDL-1 sample: (a) RH is 100% and (b) 50%

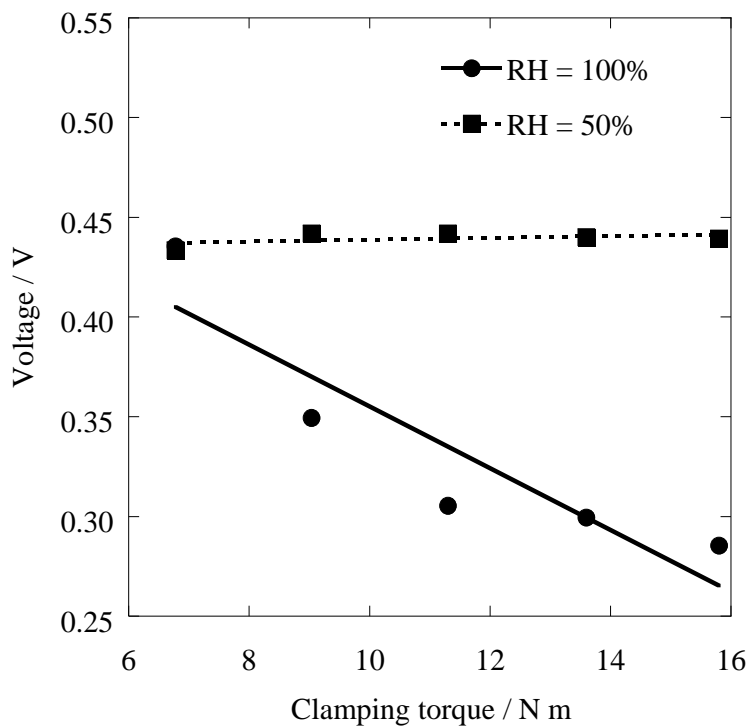


**Fig. 6.3** The cell voltage variation at a current density of  $1.6 \text{ A cm}^{-2}$  as a function of clamping torque

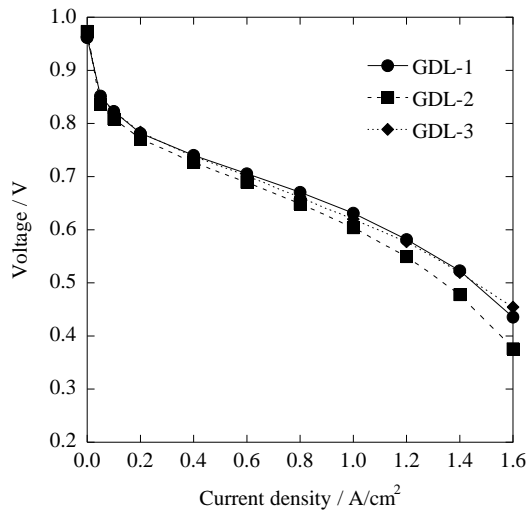
thus reactant gases flow well through the GDL although the high clamping torque narrowed down the diffusion path. The voltage variation at a current density of  $1.6 \text{ A cm}^{-2}$  under different clamping torques is shown in Fig. 6.3. The voltage at 100% RH decreases dramatically as clamping torque increases, while the voltage at 50% RH remains substantially constant regardless of applied clamping torque. As the clamping torque of the cell is increased, the GDL in the cell should be increasingly compressed, typically resulting in a more dense structure with reduced gas permeability. Thus, the cell with the compressed GDL may be more vulnerable to water flooding and this phenomenon can be more manifest especially under operating conditions of higher RH and/or higher current density. From these results, it is thought that the voltage drop due to the water flooding effect is relatively large when supplying gases are fully hydrated, but it can be reduced under less hydrated condition.

By contrast, previous studies suggested that high clamping torque reduced the contact resistance between the bipolar plate and the GDL which had a positive effect on the fuel cell performance. Yim et al. [62] represented that the PEMFC stack with high GDL compression (30%) showed a higher performance than that with low GDL compression (15%) at all current density ranges, indicating that the decrease of contact resistance is more

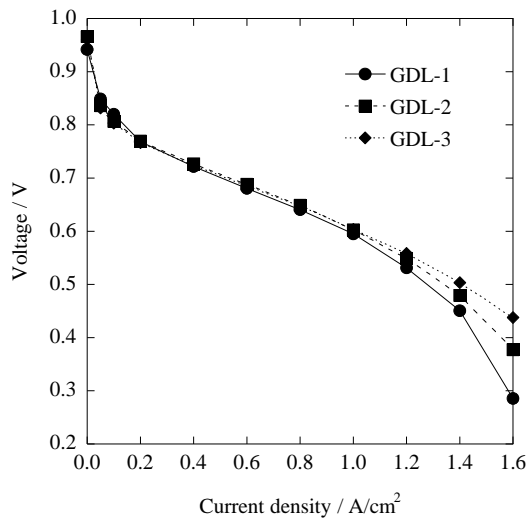
dominant factor on the stack performance than the increase of mass transport resistance during GDL compression in their stack configurations. Under the specific cell configuration and clamping torques (6.78 ~ 15.8 N m) used in the present study, however, the effect of the increased mass transport resistance by increased clamping torque is likely to be more dominant than that of the decreased contact resistance. That is why the fuel cell performance at high RH of 100% decreases as clamping torque increases.

The *I-V* tests of cells using GDL-2 and GDL-3 were also conducted. As representative examples, the polarization curves for all GDLs at the lowest and highest clamping torques are plotted in Fig. 6.4. As shown in Fig. 6.4(a), the cell performances using GDL-1 and GDL-3 are higher than that of GDL-2. Firstly, comparison of the results of GDL-1 and GDL-2 indicated that the MPL with rough surface (GDL-1) is better for increasing the cell performance than that with smooth surface (GDL-2) at the lowest clamping torque. The benefits of the MPL are most noticeable at higher current densities, indicating that the rough surface of MPL with more large cracks may induce more favorable liquid water distribution which results in better mass transport for both product water removal and reactant gases supply. According to SEM images shown in Fig. 6.1, the GDL-1 has an MPL with rough surface that has a lot of large cracks when compared with the MPL

with relatively smooth surface (GDL-2). It is generally thought that these cracks allow the generated water to flow more easily through the MPL at higher current density conditions. Thus the fuel cell performance using GDL-1 is higher than that using GDL-2 due to the better water distribution in the cell. As for the results of GDL-2 and GDL-3, the GDL-3 shows a higher cell performance than GDL-2. It is believed that the contact resistance between bipolar plate and macro-porous substrate using carbon fiber felt might be higher than that using carbon fiber paper, because carbon fiber felt has more entangled structure in comparison with the carbon fiber paper as mentioned in section 6.2. Furthermore, the improved cell performance is also explained that oxygen counter flow through the carbon fiber paper is better than other types of GDLs [63]. Fig. 6.4(b) represents the cell performances with various GDLs at the highest clamping torque of 15.8 N m. It is observed that the cell performances of all the GDL samples decrease at high current densities. The higher clamping torque usually breaks the GDL substrate, resulting in the reduced pores available for reactant gases transport within the GDL during fuel cell operation [63]. Additionally, water is generated more at high current densities and fills up the reduced pores within the GDLs, which causes the mass transport resistance. It is noteworthy that the GDL-1 sample shows the largest decrease in performance, implying that



(a)



(b)

**Fig. 6.4** The polarization curves for all types of GDLs under a cell temperature of 65 °C and fully humidified conditions: (a) clamping torque is 6.78 N m and (b) clamping torque is 15.8 N m

the damage of GDL-1 sample is the biggest among all GDL samples at the highest clamping torque.

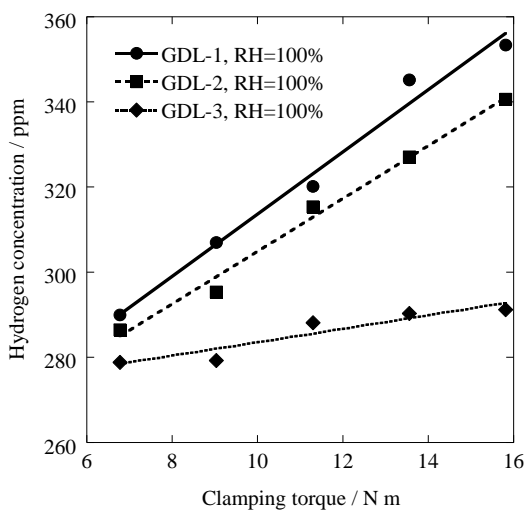
## 6.4 Effect of hydrogen crossover on the OCV

The hydrogen is permeated from the anode to cathode sides and accumulated in cathode stream, thus hydrogen crossover can be detected by measuring the gas composition at the cathode exit stream. Fig. 6.5(a) shows hydrogen concentration at cathode exit stream under various clamping torques when anode hydrogen and cathode nitrogen flow rates are 0.9 and 0.5 L min<sup>-1</sup>, respectively. Molar flow rate of hydrogen crossover can be calculated as follows

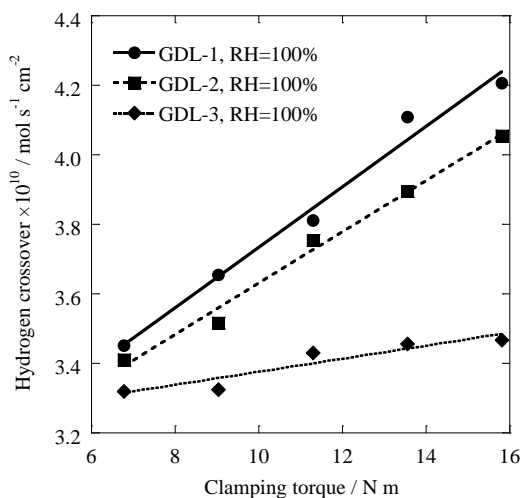
$$m = \frac{C_{H_2} \times FL_{H_2} \times \rho_{H_2}}{6 \times 10^7 \times M_{H_2} \times A} \quad (6.1)$$

where  $m$  is the molar flow rate of hydrogen crossover with the unit of mol s<sup>-1</sup> cm<sup>-2</sup>,  $C_{H_2}$  is the hydrogen concentration and  $FL_{H_2}$  is the nitrogen flow rate at the cathode side,  $\rho_{H_2}$  is the density of hydrogen gas (0.0714 g L<sup>-1</sup> at 65°C),  $M_{H_2}$  is the molar weight of hydrogen gas (2 g mol<sup>-1</sup>) and  $A$  is the active area of the cell (25 cm<sup>2</sup>). With this simple equation, we can calculate a hydrogen crossover value of  $3.57 \times 10^{-9}$  mol s<sup>-1</sup> cm<sup>-2</sup> when the hydrogen concentration is 300 ppm, which is similar to that ( $3.78 \times 10^{-9}$  mol s<sup>-1</sup> cm<sup>-2</sup>)

reported by Cheng et al. [6]. Molar flow rates of hydrogen crossover as a function of clamping torque are shown in Fig. 6.5(b). As shown in Fig. 6.5(a) and (b), hydrogen concentrations and crossover rate of cells with all GDL samples increase with the increase of clamping torque, respectively. Under high clamping torque conditions, the possibility of carbon fiber penetration increases due to the increased clamping torque. Thus micro-pin holes are made more by the penetration of carbon fibers into the membrane with increasing clamping torque. Consequently, the micro-pin holes which are the pathways of hydrogen crossover can accelerate hydrogen crossover through the membrane. A schematic process of GDL penetration into the MEA is proposed in Fig. 6.6. When the cell is compressed, the thickness of GDL substrate is reduced firstly among the assembling materials of fuel cell. If higher clamping pressure is applied to the fuel cell assembly, the MPLs are partly fractured, which makes it easy for carbon fibers in macro-porous substrate to penetrate into membrane through the MPL and catalyst layer. When the clamping torque is increased further, carbon fibers may make some cracks or holes on the membrane surface. By comparing the results of GDL-1 with those of GDL-2, it is known that the MPL coating type has an effect on the hydrogen crossover. The MPL of GDL-1 has a rough surface with large cracks that allow the carbon fibers to penetrate into the membrane



(a)



(b)

**Fig. 6.5** (a) Hydrogen concentration and (b) crossover rate at cathode exit stream as a function of clamping torque. Anode  $\text{H}_2$  flow and cathode  $\text{N}_2$  flow rates are  $0.9$  and  $0.5 \text{ L min}^{-1}$ , respectively

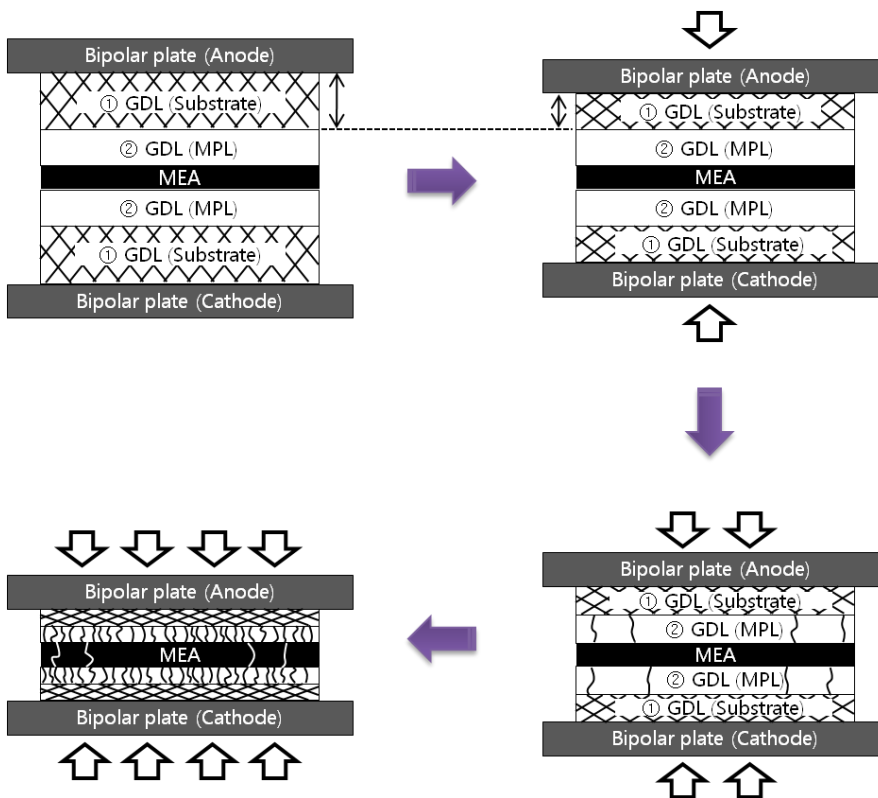


**Fig. 6.6** A proposed process of GDL substrate penetration into the MEA as clamping torque increases

more easily. On the other hand, the MPL of GDL-2 has a relatively smooth surface with small cracks, indicating that the MPL of GDL-2 is likely to be relatively dense and uniform, thus it can reduce the penetration of carbon fibers in substrate into the membrane. Thus the increase in hydrogen crossover of cell with the GDL-1 sample is much higher than that with the GDL-2 sample. Similarly, the results of GDL-2 and GDL-3 exhibit the effect of the substrate structure on the hydrogen crossover of fuel cells. As listed in Table 1, the GDL-2 has a carbon fiber felt substrate, while the GDL-3 has a carbon fiber paper substrate. As shown in Fig. 6.5(a), it is seen that the increase in hydrogen crossover for GDL-2 case with increasing the clamping torque is higher than that for GDL-3 case. From these results, it is concluded that the membrane damage due to the penetration of the carbon fiber felts is much more severe than that of the carbon fiber papers.

Hydrogen crossover from the anode to cathode can affect the decrease in OCV of the fuel cells. Vilekar et al. [7] theoretically analyzed the role of hydrogen crossover in PEMFCs. They explained that the hydrogen that permeates from the anode to cathode can undergo oxidation on the Pt catalyst with oxygen electrochemically. The hydrogen oxidation reaction at the cathode provides electrons, or a crossover current at cathode, for the oxygen reduction reaction at the cathode even under open-circuit conditions.

Thus the entire potential loss under open-circuit conditions occurs due to hydrogen crossover. Zhang et al. [40] also suggested that the difference in OCV between the theoretical and the measured values is caused mainly by two factors: one is the mixed potential of the Pt/PtO catalyst surface and the other is hydrogen crossover. From this information, it is known that the increase in hydrogen crossover results in the decrease in OCV. Fig. 6.7 shows the OCVs under various clamping torques when RH is 100% and cell temperature is 65°C at ambient gas pressure. As shown in the Fig. 6.7, the OCVs of cells for all GDL cases decrease as clamping torque increases. This is in good agreement with the result of hydrogen crossover which increases with the clamping torques. The OCV reduction of cell with GDL-1 is much greater than that with GDL-2 and GDL-3, especially at higher clamping torques. It is also explained that the hydrogen crossover of GDL-1 case is larger than that of other cases. Accordingly, hydrogen crossover resulting from the membrane puncturing due to the GDL penetration results in the reduction of OCV that affects the membrane degradation behavior. Thus it is concluded that the GDL-3 is better than the other two GDLs in terms of fuel cell durability, because the GDL-3 shows the minimum OCV reduction as clamping torque increases.

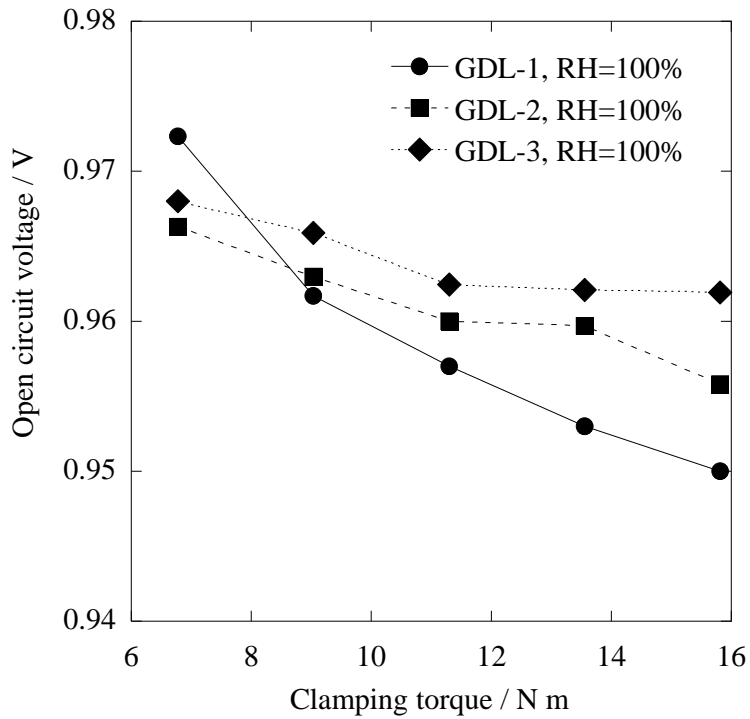


**Fig. 6.7** OCV as a function of clamping torque when RH is 100% and cell temperature is 65°C at ambient gas pressure

## 6.5 Visual observation of the GDLs and MEA

In order to investigate the membrane puncturing due to the carbon fibers penetration, the cross-sectional morphology of the GDL-1 and the in-plane surface morphology of anode catalyst layer in MEA before and after cell compression were observed by SEM images as shown in Fig 6.8. Fig. 6.8(a) and (b) show the cross-sectional morphology of GDL-1 before and after cell compression tests, respectively. The upper part of the carbon fiber felt substrate is covered with the MPL. As shown in Fig. 6.8(a) and (b), the thickness of GDL-1, especially the macro-porous substrate region, is reduced by the cell compression. This may result from the fact that the carbon fiber felt is a non-woven material so that the thickness cannot be easily recovered after the compression. Thus, it is believed that the GDL can be easily compressed by external compression force, resulting in a more dense structure with reduced permeability. This may explain why the fuel cell is more vulnerable to water flooding with increasing compression force under higher RH condition, as shown in Fig. 6.3. Fig. 6.8(c) and (d) show the in-plane surface morphology of anode catalyst layer in MEA before and after cell compression tests, respectively. The SEM images of the catalyst layer were observed at 1000× magnification. Contrary to our expectation, the carbon fiber penetration into the membrane through the catalyst layer due to

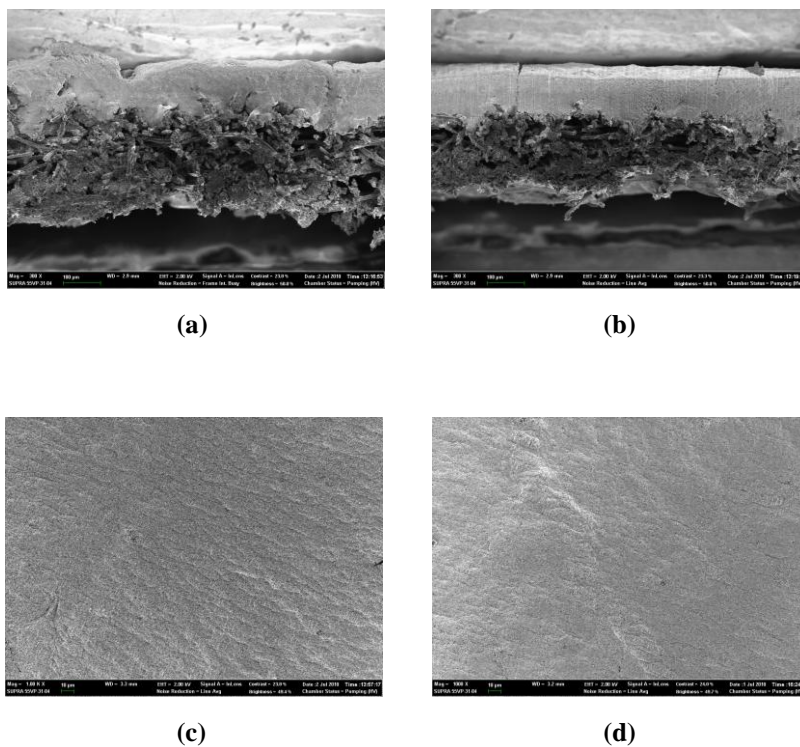


**Fig. 6.8** Cross-sectional SEM images of GDL-1 (a) before and (b) after the cell compression tests and in-plane surface SEM images of anode catalyst layer in MEA (c) before and (d) after the cell compression tests

the high clamping torque is not clearly observed in the SEM images because the surface morphology of the catalyst layer does not change after the cell compression (see Fig. 6.8(c) and (d)). The reason for this observation is not clear yet, but one possible reason is that the measurement of SEM images is an ex situ characterization technique which is carried out after the fuel cell tests [64]. The carbon fiber penetration phenomenon may appear more manifest under higher temperature, fully hydrated and higher clamping torque conditions. Under lower temperature, less hydrated and lower clamping torque conditions, however, the membrane tends to recover to its original shape external mechanical stress was released thus the micro pin-holes caused by GDL penetration into the membrane surface through catalyst layer may be very hard to recognize. Therefore, a further work using an in-situ observation technique under compressed situation should be necessary to clearly observe the carbon fiber penetration into the membrane in the future.

## **6.6 Summary**

In order to investigate the effect of GDL structure on the membrane puncturing, the cell performance, hydrogen crossover and OCV of fuel cells

were measured under various clamping torque conditions. The fuel cell performance decreases as clamping torque increases when RH is 100% due to the reduced porosity of GDL. The performances of fuel cells with GDL-1 (a carbon fiber felt substrate with MPL having rough surface) and GDL-3 (a carbon fiber paper substrate with MPL having smooth surface) are higher than that with GDL-2 (a carbon fiber felt substrate with MPL having smooth surface) under low clamping torque conditions, whereas when clamping torque is high (*i.e.*, approximately 15.8 N m), the GDL-1 sample shows the largest decrease in cell performance, implying that the damage of GDL-1 is the biggest among all the GDL samples. Hydrogen crossover of cells for all GDL samples increases with the increase of clamping torque, especially the degree of increase of GDL-1 is much greater than that of the other two GDL samples. The OCV of cells for all GDL samples decreases as clamping pressure increases, and especially the OCV reduction of GDL-1 is much greater than that of GDL-2 and GDL-3. It implies that the penetration of carbon fibers of GDL-1 into membrane should be higher than that of the other two GDL samples. On the other hand, the cell with the GDL-3 is expected to have better durability than the other two GDLs, because the GDL-3 shows the minimum OCV reduction as clamping torque increases.

Contrary to our expectation, however, the carbon fiber penetration into

the membrane through the MPL and catalyst layer due to the high clamping torque is not clearly observed in the SEM images. The reason for this observation is not clear yet, but a further work using an in-situ observation technique should be necessary to clearly observe the carbon fiber penetration into the membrane in the future.

## Chapter 7. Concluding remarks

In this study, the gas crossover rates of hydrogen, oxygen and nitrogen in PEFMCs were measured using an in-situ direct gas detection method at various operating conditions. The effect of operating parameters such as temperature, RH, hydrogen pressure, and membrane thickness on hydrogen crossover rate in PEMFCs was firstly investigated. The results show that the hydrogen crossover rate increases proportional to the increase in temperature for all membrane samples. As the temperature increases, the reacting gas shows greater molecular movement, resulting in higher rate of hydrogen crossover. Higher hydrogen crossover rates are also observed at higher RH conditions for all membrane samples. Increased water content of the membrane results in greater intermolecular distance between the polymer chains to enlarge the free volume, which offers additional transport pathways. The hydrogen partial pressure increases as hydrogen pressure increases, resulting in increased hydrogen crossover rate. It is found that the change in hydrogen crossover rate is significant for the thinner membranes (NRM-1 and NRM-2), whereas the hydrogen crossover rates are relatively unchanged for the thicker membranes (NRM-3, NRM-4 and NRM-5). All parameters on hydrogen crossover rate, including temperature, relative humidity, hydrogen pressure, and the inverse of the logarithmic membrane thickness, were

compared through MLR. MLR analysis of the four independent parameters showed that the hydrogen crossover rate increases with the increase in the following variables: inverse of logarithmic membrane thickness > hydrogen pressure > RH > and temperature.

Local measurements of the hydrogen crossover rate were also conducted using a single fuel cell with the specially-designed cathode bipolar plate, which has six sampling ports. Firstly, the local distribution of the hydrogen crossover rate from the gas inlet to the outlet of cathode was examined. The hydrogen crossover rate near the inlet was large. The hydrogen gas pressure near the inlet was higher than that near the outlet. Thus, it was believed that the partial pressure gradient of hydrogen was one of the reasons for the local variation of hydrogen crossover in the fuel cell. The hydrogen crossover rates increase with decreasing the nitrogen flow rates at a given section, but the tendency of higher hydrogen crossover rates near the inlet than the outlet was observed regardless of the nitrogen flow rates examined in this study. The effects of operating conditions on the hydrogen crossover rate were also investigated. The hydrogen crossover rate increased with the increase in both temperature and RH of the fuel cell. Furthermore, the effects of temperature and RH on OCV were also examined and compared with the results of the hydrogen crossover rate. The results

showed the decrease of the OCV with increase in both cell temperature and RH conditions, which is closely related with the increase in hydrogen crossover.

The quantitative measurements of oxygen crossover that reacts with hydrogen have been conducted by using a MS system. Oxygen permeability values estimated in this study show similar trends to those estimated by other studies. To identify the effect of gases that have a different molecular weight on oxygen crossover, the gas selectivity tests were conducted. Result showed that the oxygen concentration showed no trend with the molecular weight, implying that the effect of gases that have different molecular weights on oxygen crossover can be negligible. Thus, the data of oxygen crossover using hydrogen/oxygen and helium/oxygen were used together to calculate the effective oxygen permeability. The effective oxygen permeability could explain the exact amount of oxygen crossover that affect the membrane degradation and/or water generation under the fuel cell operating conditions. Thus, the effective oxygen permeability should be considered as an index of the membrane degradation and/or water generation due to oxygen crossover. The ratio between the normal and effective oxygen permeability is in a range between 0.927 ~ 0.933 under the fuel cell temperature conditions.

Nitrogen crossover was measured using a mass spectrometer under

various operating conditions and under OCV and power generation conditions in single PEMFCs. Under OCV conditions, nitrogen crossover increased with increasing cell temperature under all RH conditions. NPC was calculated based on the obtained nitrogen concentration data and the NPC results fitted the form of Arrhenius expression. When the PEMFC membrane was fully hydrated, the maximum permeability coefficient and activation energy of nitrogen were  $5.14 \times 10^{-13} \text{ mol m}^{-1} \text{ s}^{-1} \text{ Pa}^{-1}$  and  $19.83 \text{ kJ mol}^{-1}$ , respectively. NPC as a function of RH was also investigated. At higher cell temperatures and when the membrane was hydrated, a higher NPC was observed. In addition, the solubility decreased slightly and diffusivity increased remarkably, when the membrane was hydrated, indicating that the permeability coefficient increased. Under power generation conditions, nitrogen crossover increased with increasing current density. Moreover, when current density increased, nitrogen crossover increases were found to be related to elevated membrane temperature and high water content. When the  $SR_A$  was low, nitrogen concentration increased under all current densities tested. At low current densities, a change in the hydrogen flow rate, due to a change in the  $SR_A$  being used, significantly affects the nitrogen concentration.

In order to investigate the effect of GDL structure on the membrane

puncturing, the cell performance, hydrogen crossover and OCV of fuel cells were measured under various clamping torque conditions. The fuel cell performance decreases as clamping torque increases when RH is 100% due to the reduced porosity of GDL. The performances of fuel cells with GDL-1 (a carbon fiber felt substrate with MPL having rough surface) and GDL-3 (a carbon fiber paper substrate with MPL having smooth surface) are higher than that with GDL-2 (a carbon fiber felt substrate with MPL having smooth surface) under low clamping torque conditions, whereas when clamping torque is high (*i.e.*, approximately 15.8 N m), the GDL-1 sample shows the largest decrease in cell performance, implying that the damage of GDL-1 is the biggest among all the GDL samples. Hydrogen crossover of cells for all GDL samples increases with the increase of clamping torque, especially the degree of increase of GDL-1 is much greater than that of the other two GDL samples. The OCV of cells for all GDL samples decreases as clamping pressure increases, and especially the OCV reduction of GDL-1 is much greater than that of GDL-2 and GDL-3. It implies that the penetration of carbon fibers of GDL-1 into membrane should be higher than that of the other two GDL samples. On the other hand, the cell with the GDL-3 is expected to have better durability than the other two GDLs, because the GDL-3 shows the minimum OCV reduction as clamping torque increases.

Contrary to our expectation, however, the carbon fiber penetration into the membrane through the MPL and catalyst layer due to the high clamping torque is not clearly observed in the SEM images. The reason for this observation is not clear yet, but a further work using an in-situ observation technique should be necessary to clearly observe the carbon fiber penetration into the membrane in the future.

The measurement of gas permeability could provide useful data and an insight into the selection of polymeric materials not only for membrane manufacturers, but also for fuel cell researchers understanding failure modes of membranes in operating fuel cells. Transient permeability measurement could also contribute to the fundamental understanding of diffusion properties of membranes and MEAs. Furthermore, nitrogen crossover data may be useful in the development of a nitrogen crossover model that can be used to facilitate establishment of an efficient method for hydrogen recirculation systems.

## References

- [1] Mehrer H. Diffusion in solids: fundamentals, methods, materials, diffusion-controlled processes: Springer; 2007.
- [2] Yeager HL, Steck A. Cation and water diffusion in nafion ion exchange membranes: influence of polymer structure. Journal of the Electrochemical Society 1981;128:1880-1884.
- [3] Sakai T, Takenaka H, Wakabayashi N, Kawami Y, Torikai E. Gas permeation properties of solid polymer electrolyte (SPE) membranes. Journal of the Electrochemical Society 1985;132:1328-1332.
- [4] Sakai T, Takenaka H, Torikai E. Gas diffusion in the dried and hydrated Nafions. Journal of the Electrochemical Society 1986;133:88-92.
- [5] Kocha S, Yang J, Yi J. Characterization of gas crossover and its implications in PEM fuel cells. AIChE Journal 2006;52:1916-1925.
- [6] Cheng X, Zhang J, Tang Y, Song C, Shen J, Song D, et al. Hydrogen crossover in high-temperature PEM fuel cells. Journal of Power Sources 2007;167:25-31.
- [7] Vilekar SA, Datta R. The effect of hydrogen crossover on open-circuit voltage in polymer electrolyte membrane fuel cells. Journal of Power Sources 2010;195:2241-2247.

- [8] Inaba M, Kinumoto T, Kiriake M, Umebayashi R, Tasaka A, Ogumi Z. Gas crossover and membrane degradation in polymer electrolyte fuel cells. *Electrochimica Acta* 2006;51:5746-5753.
- [9] Bessarabov D, Kozak P. Measurement of gas permeability in SPE membranes for use in fuel cells. *Membrane Technology* 2007;2007:6-9.
- [10] Nam J, Chippar P, Kim W, Ju H. Numerical analysis of gas crossover effects in polymer electrolyte fuel cells (PEFCs). *Applied Energy* 2010;87:3699-3709.
- [11] Yuan XZ, Zhang S, Wang H, Wu J, Sun JC, Hiesgen R, et al. Degradation of a polymer exchange membrane fuel cell stack with Nafion<sup>®</sup> membranes of different thicknesses: Part I. In situ diagnosis. *Journal of Power Sources* 2010;195:7594-7599.
- [12] Francia C, Ijeri VS, Specchia S, Spinelli P. Estimation of hydrogen crossover through Nafion<sup>®</sup> membranes in PEMFCs. *Journal of Power Sources* 2011;196:1833-1839.
- [13] Willsau J, Heitbaum J. The influence of Pt-activation on the corrosion of carbon in gas diffusion electrodes—A dems study. *Journal of Electroanalytical Chemistry and Interfacial Electrochemistry* 1984;161:93-101.

- [14] Maass S, Finsterwalder F, Frank G, Hartmann R, Merten C. Carbon support oxidation in PEM fuel cell cathodes. *Journal of Power Sources* 2008;176:444-451.
- [15] Lim KH, Oh HS, Jang SE, Ko YJ, Kim HJ, Kim H. Effect of operating conditions on carbon corrosion in polymer electrolyte membrane fuel cells. *Journal of Power Sources* 2009;193:575-579.
- [16] Hodgdon R, Boyack J, LaConti A. The Degradation of Polystyrene Sulfonic Acid. TIS Report 65DE 1966;5.
- [17] LaConti A, Hamdan M, McDonald R. Mechanisms of membrane degradation. *Handbook of Fuel Cells—Fundamentals, Technology, and Applications* 2003;3:647-662.
- [18] Ramaswamy N, Hakim N, Mukerjee S. Degradation mechanism study of perfluorinated proton exchange membrane under fuel cell operating conditions. *Electrochimica Acta* 2008;53:3279-3295.
- [19] Broka K, Ekdunge P. Oxygen and hydrogen permeation properties and water uptake of Nafion 117® membrane and recast film for PEM fuel cell. *Journal of Applied Electrochemistry* 1997;27:117-123.
- [20] Haug AT, White RE. Oxygen diffusion coefficient and solubility in a new proton exchange membrane. *Journal of the Electrochemical Society* 2000;147:980-983.

- [21] Peron J, Mani A, Zhao X, Edwards D, Adachi M, Soboleva T, et al. Properties of Nafion<sup>®</sup> NR-211 membranes for PEMFCs. *Journal of Membrane Science* 2010;356:44-51.
- [22] Ahluwalia RK, Wang X. Buildup of nitrogen in direct hydrogen polymer-electrolyte fuel cell stacks. *Journal of Power Sources* 2007;171:63-71.
- [23] Chiou J, Paul D. Gas permeation in a dry Nafion membrane. *Industrial & Engineering Chemistry Research* 1988;27:2161-2164.
- [24] Rutherford SW, Do DD. Review of time lag permeation technique as a method for characterisation of porous media and membranes. *Adsorption* 1997;3:283-312.
- [25] Ogumi Z, Takehara Z, Yoshizawa S. Gas permeation in SPE method. *Journal of the Electrochemical Society* 1984;131:769-773.
- [26] Ogumi Z, Kuroe T, Takehara Z-i. Gas permeation in SPE method. *Journal of the Electrochemical Society* 1985;132:2601-2605.
- [27] Mohamed HFM, Ito K, Kobayashi Y, Takimoto N, Takeoka Y, Ohira A. Free volume and permeabilities of O<sub>2</sub> and H<sub>2</sub> in Nafion membranes for polymer electrolyte fuel cells. *Polymer* 2008;49:3091-3097.

- [28] Baik KD, Kim MS. Characterization of nitrogen gas crossover through the membrane in proton-exchange membrane fuel cells. *International Journal of Hydrogen Energy* 2011;36:732-739.
- [29] Baik KD, Kim SI, Hong BK, Han K, Kim MS. Effects of gas diffusion layer structure on the open circuit voltage and hydrogen crossover of polymer electrolyte membrane fuel cells. *International Journal of Hydrogen Energy* 2011;36:9916-9925.
- [30] Baik KD, Kong IM, Hong BK, Kim SH, Kim MS. Local measurements of hydrogen crossover rate in polymer electrolyte membrane fuel cells. *Applied Energy*.
- [31] Shim JY, Tsushima S, Hirai S. Experimental and Modeling Studies on the Effect of Oxygen Partial Pressure on Membrane Degradation in PEMFCs. *Journal of the Electrochemical Society* 2009;156:B690-694.
- [32] Kaneko K, Tsushima S, Hirai S. Effect of SO<sub>2</sub> concentration and relative humidity on contamination of cathode and anode in PEMFC. *ECS Transactions* 2009;25:1279-1287.
- [33] Pietro T, Franco M, Irma L, Roberta S. Quantitative Applications of Mass Spectrometry 2006.

- [34] Bley WG. Quantitative measurements with quadrupole mass spectrometers: important specifications for reliable measurements. Vacuum 1988;38:103-109.
- [35] Comyu J. Polymer permeability 1985.
- [36] Liu L, Chakma A, Feng X. Gas permeation through water-swollen hydrogel membranes. Journal of Membrane Science 2008;310:66-75.
- [37] Adachi M, Navessin T, Xie Z, Li FH, Tanaka S, Holdcroft S. Thickness dependence of water permeation through proton exchange membranes. Journal of Membrane Science 2010;364:183-193.
- [38] Zhu Z, Sun W, Yan L, Liu W, Liu W. Synthesis and hydrogen permeation of Ni-Ba(Zr<sub>0.1</sub>Ce<sub>0.7</sub>Y<sub>0.2</sub>)O<sub>3-δ</sub> metal-ceramic asymmetric membranes. International Journal of Hydrogen Energy 2011;36:6337-6342.
- [39] Kundu S, Fowler MW, Simon LC. Gas selectivity measurements as a diagnostic tool for fuel cells. Journal of Power Sources 2008;180:760-766.
- [40] Zhang J, Tang Y, Song C, Zhang J, Wang H. PEM fuel cell open circuit voltage (OCV) in the temperature range of 23 °C to 120 °C. Journal of Power Sources 2006;163:532-537.

- [41] Zaza F, Paoletti C, LoPresti R, Simonetti E, Pasquali M. Multiple regression analysis of hydrogen sulphide poisoning in molten carbonate fuel cells used for waste-to-energy conversions. *International Journal of Hydrogen Energy* 2011;36:8119-8125.
- [42] Placca L, Kouta R, Candusso D, Blachot J-F, Charon W. Analysis of PEM fuel cell experimental data using principal component analysis and multi linear regression. *International Journal of Hydrogen Energy* 2010;35:4582-4591.
- [43] Gelman A, Hill J. *Data analysis using regression and multilevel/hierarchical models*: Cambridge University Press New York; 2007.
- [44] Hamby DM. A review of techniques for parameter sensitivity analysis of environmental models. *Environmental Monitoring and Assessment* 1994;32:135-154.
- [45] Jung CY, Shim HS, Koo SM, Lee SH, Yi SC. Investigations of the temperature distribution in proton exchange membrane fuel cells. *Applied Energy* 2012;93:733-741.
- [46] Higier A, Liu H. Optimization of PEM fuel cell flow field via local current density measurement. *International Journal of Hydrogen Energy* 2010;35:2144-2150.

- [47] Hwnag JJ, Chang WR, Peng RG, Chen PY, Su A. Experimental and numerical studies of local current mapping on a PEM fuel cell. *International Journal of Hydrogen Energy* 2008;33:5718-5727.
- [48] Sun H, Zhang G, Guo L, Liu H. A Study of dynamic characteristics of PEM fuel cells by measuring local currents. *International Journal of Hydrogen Energy* 2009;34:5529-5536.
- [49] Zhang G, Guo L, Ma L, Liu H. Simultaneous measurement of current and temperature distributions in a proton exchange membrane fuel cell. *Journal of Power Sources* 2010;195:3597-3604.
- [50] Alaefour I, Karimi G, Jiao K, Li X. Measurement of current distribution in a proton exchange membrane fuel cell with various flow arrangements – A parametric study. *Applied Energy* 2012;93:80-89.
- [51] Zhou B, Huang W, Zong Y, Sobiesiak A. Water and pressure effects on a single PEM fuel cell. *Journal of Power Sources* 2006;155:190-202.
- [52] Matsuura T, Siegel JB, Chen J, Stefanopoulou AG. Multiple degradation phenomena in polymer electrolyte fuel cell operation with dead-ended anode. *Proceedings of the ASME 9th International Fuel Cell Science, Engineering and Technology Conference*. Washington 2011 Aug 7-10.

- [53] Takahashi S, Yoshida M, Asano M, Tanaka T, Nakagawa T. Effect of heavy-ion irradiation on the gas permeability of poly(ethylene terephthalate) (PET) membranes. *Journal of Applied Polymer Science* 2001;82:206-216.
- [54] Lufrano F, Gatto I, Staiti P, Antonucci V, Passalacqua E. Sulfonated polysulfone ionomer membranes for fuel cells. *Solid State Ionics* 2001;145:47-51.
- [55] Kolde JA, Bahar B, Wilson MS, Zawodzinski TA, Gottesfeld S. Advanced composite polymer electrolyte fuel cell membranes. *Proc Electrochem Soc* 1995;23:193-201.
- [56] Mittelsteadt C, Umbrell M. Gas permeability in perfluorinated sulfonic acid polymer electrolyte membranes. *ECS Meeting Abstracts: ECS*; 2006. p. 770-770.
- [57] Mittelsteadt CK, Liu H. Conductivity, permeability, and ohmic shorting of ionomeric membranes. In: Vielstich W, Gasteiger HA, Yokokawa H, editors. *Handbook of fuel cells-advances in electrocatalysis, materials, diagnostics and durability*, vol 5. England: John Wiley & Sons Ltd.; 2010. p. 345-358.

- [58] Lai YH. An investigation of shorting failure in PEM fuel cells. Proceedings of the ASME 8th International Fuel Cell Science, Engineering and Technology Conference. New York 2010.
- [59] Han K, Hong BK, Kim SH, Ahn BK, Lim TW. Influence of anisotropic bending stiffness of gas diffusion layers on the electrochemical performances of polymer electrolyte membrane fuel cells. International Journal of Hydrogen Energy 2010;35:12317-12328.
- [60] Han K, Hong BK, Kim SH, Ahn BK, Lim TW. Influence of anisotropic bending stiffness of gas diffusion layers on the degradation behavior of polymer electrolyte membrane fuel cells under freezing conditions. International Journal of Hydrogen Energy 2011;36:12452-12464.
- [61] Chang WR, Hwang JJ, Weng FB, Chan SH. Effect of clamping pressure on the performance of a PEM fuel cell. Journal of Power Sources 2007;166:149-154.
- [62] Yim SD, Kim BJ, Sohn YJ, Yoon YG, Park GG, Lee WY, et al. The influence of stack clamping pressure on the performance of PEM fuel cell stack. Current Applied Physics 2010;10:S59-S61.
- [63] Park S, Popov BN. Effect of a GDL based on carbon paper or carbon cloth on PEM fuel cell performance. Fuel 2011;90:436-440.

[64] O'Hayre R, Cha SW, Colella W, Prinz FB. Fuel cell fundamentals. New York: John Wiley & Sons; 2009.

## 구 문 초 록

고분자 전해질 막 연료전지에는 주로 고분자 멤브레인이 이온 교환막으로 널리 사용되고 있다. 멤브레인의 가장 중요한 기능은 수소 이온을 음극에서 양극으로 전달시켜 주는 역할이지만, 연료전지에 공급되는 수소와 공기의 혼합을 방지하는 막의 역할도 동시에 수행하고 있다. 하지만, 고분자 물질로 구성되어 있는 멤브레인의 특성 때문에 수소 및 공기가 멤브레인을 통과하여 투과되는 현상이 발생하게 되는데, 이를 “기체 크로스오버” 현상이라 한다. 본 연구에서는 연료전지에서 발생하는 수소, 산소 및 질소 기체의 크로스오버 양을 질량분석기를 사용하여 정량적으로 측정하고 분석하였다. 우선적으로 기체 크로스오버에 영향을 미치는 주변 인자들의 영향을 분석하기 위하여, 연료전지의 온도, 가습량, 압력 및 멤브레인 두께를 변화시켜가며 수소 크로스오버를 측정하였다. 실험 결과 수소 크로스오버는 연료전지의 주변 온도 및 공급되는 기체의 가습량 증가에 따라 선형적으로 증가하였다. 또한, 연료전지 공급 기체의 압력 증가에 대해서도 선형적인 증가를 보였다. 실험 결과를 다중 회귀 분석 통계 방법을 사용하여 각각의 주변 인자가 수소 크로스오버에 미치는 영향도를 분석한 결과, 수소 크로스오버에 큰 영향을 미치는 인자는 멤브레인 두께, 압력, 가습량, 온도 순서로 분석이 되었다. 다음으로 연료전지 내부에서의 극소적인 수소 크로스오버를 측정하기 위하여 특수 제작한 양극측 분리판을 자체적으로 개발하였다. 새롭게 제작한 분리판을 연료전지에 적용하여 연료전지 채널 입구에서 출구까지 수소 크로스오버가 극소적으로 어떻게 발생하는지를 분석하였다. 실험 결과 수소 크로스오버는 연료전지 입구 영역에서 다량 발생함을 알 수 있었고, 채널 출구 쪽으로 갈수록 수소 크로스오버가 발생하는 양은 점차적으로 감소하는 것을 확인하였다. 이러한 극소적인 수소

크로스오버 차이를 발생시키는 원인 중 하나로 연료전지에 공급되는 수소 기체 압력의 영향으로 분석할 수 있다. 연료전지 내구성 저하의 원인으로 지적 받고 있는 산소 크로스오버 또한 기존 방법과는 다른 본 연구에서 개발한 새로운 방법을 통하여 측정하였다. 이번 연구에서 효과적인 산소 투과 계수 값을 새롭게 제시함으로써 음극의 물관리 및 내구성 저하에 영향을 미치는 산소크로스오버의 정확한 양을 제시하였다. 질소 크로스오버 측정 또한 다양한 온도 및 가습 조건에서 수행을 하였다. 먼저 개회로 전압 조건에서 질소 크로스오버는 온도와 가습량에 비례하여 증가하는 경향을 보였다. 또한 질소 투과 계수를 계산함으로써 수소 재순환 시스템에서의 질소 누적 모델 개발을 위한 기초 자료를 제공하였다. 마지막으로 기체 확산층 구조에 따른 멤브레인 단락 현상을 관찰하기 위하여 체결압력에 따른 연료전지 성능, 수소 크로스오버 및 개회로 전압을 측정하였다. 기체 확산층 1 번 구조(탄소 펠트)를 사용 하였을 때 다른 기체 확산층 보다 높은 성능을 나타내는 것을 확인하였다. 기체 확산층 기재의 침투로 인한 수소 크로스오버 증가 또한 기체 확산층 1 번 구조를 사용 하였을 때 수소 크로스오버 증가율이 가장 높은 것을 알 수 있었다. 이러한 기체 크로스오버 실험 결과들은 연료전지 작동 중 고장 원인을 분석하는데 핵심 자료로 활용될 수 있을 것으로 기대한다.

**주요어:** 고분자 전해질막 연료전지, 기체 크로스오버, 기체 투과 계수,

극소위치 측정, 기체 확산층 침투

**학 번:** 2007-20801

## 감사의 글

어느덧 관악에서의 짧지 않은 10년간의 배움의 길을 마무리하고 또 다른 미래를 위한 길로 떠나기 위해 이 글을 작성하게 되었습니다. 이 논문이 시작된 이후 지금까지 도와주신 모든 분들에게 감사의 말씀을 전하고 싶습니다.

먼저 무엇보다 저에겐 늘 최고의 스승님이셨으며 전공 지식뿐 아니라 올바른 삶을 살아가는 자세를 가르쳐 주신 지도교수 김민수 교수님께 깊은 감사를 드립니다. 또한, 저의 논문을 함께 심사해 주신 강신형 교수님, 차석원 교수님, 송한호 교수님, 그리고 고려대학교의 김용찬 교수님께 깊은 감사를 드립니다.

대학원 과정 동안 많은 것을 공유하며 함께 지낸 실험실 선후배님들께도 감사의 뜻을 전하고 싶습니다. 차세대에서 살면서 늘 마음속의 지주가 되어주고 어려움을 함께 나누었던 정훈형, 성일, 임모, 범준형, 성훈, 영상, 김동규, 애리, 신동규께 감사의 뜻을 전합니다. 또한 박사과정을 하는 동안 함께 생활해온 모세, 철우, 동호, 학수, 한샘, 영욱, 민기, 진우에게 감사를 드리며, 앞으로 박사과정을 통하여 선배를 넘어서는 결실을 맺기를 바랍니다.

늘 책임감 있고 성실하게 살 수 있도록 끝없는 성원과 질책을 아끼지 않으셨던 사랑하는 아버지, 어머니, 언제나 든든한 가족이라는 울타리를 만들어준 여동생 다현에게 감사를 드립니다.

끝으로, 항상 저를 믿고 아낌없는 지도와 격려를 해주신 현대자동차의 홍보기 박사님께 깊은 감사의 말씀을 전합니다.

2013년 2월 관악에서